A 13,000-year record of climate- and human-impact-induced flooding in the Lower Meuse

Peng, F.

2020

document version
Publisher's PDF, also known as Version of record

VRIJE UNIVERSITEIT

A 13,000-year record of climate- and human-impact-induced flooding in the Lower Meuse

ACADEMISCH PROEFSCHRIFT

ter verkrijging van de graad Doctor of Philosophy aan
de Vrije Universiteit Amsterdam,
op gezag van de rector magnificus
prof.dr. V. Subramaniam,
in het openbaar te verdedigen
ten overstaan van de promotiecommissie
van de Faculteit der Bètawetenschappen
op dinsdag 20 oktober 2020 om 9.45 uur
in de aula van de universiteit,
De Boelelaan 1105

door

Fei Peng

geboren te Henan, China

promotor:	prof.dr. R.T. van Balen
copromotoren:	dr. M.A. Prins
	dr. C. Kasse

Reading committee:

prof.dr. Mark Macklin

prof.dr. Hans Middelkoop

prof.dr. Philip Ward

prof.dr. Klaudia Kuiper

dr. Joep Storms

Contents

Summary

Increased fluvial flooding, mainly by Rhine and Meuse, as a result of current and future climate change is a serious threat in the low-lying Netherlands. For the Meuse river, the earliest instrumental discharge record dates back to 1911, and older historical written flood records start from the 13th century. This time record is too short to understand the relationship between flooding and climate change. However, we can use geological archives of paleoflooding to extend our record of past floodings, in order to study its relations to past climate change.

This dissertation consists of four scientific chapters. Chapter 2, 3 and 4 are based on field sampling and laboratory analysis, and chapter 5 presents a synthesis of the flood records from chapters 2, 3 and 4. To be specific, chapters 2 and 3 studied the Holocene flooding-phase records that were reconstructed from the sedimentary infill of an abandoned channel on a floodplain (Well-Aijen core) and from levee sediments (Ooijen site), respectively. Chapter 4 extends the Lower Meuse flood record to the Lateglacial period, by means of studying the Allerød abandoned channel infill from the De Ham core. In these three studies, the length and covered time span of the retrieved sediment cores and the sampled levee section are 626 cm (Well-Aijen core with deposition during the Holocene), 256 cm (section A in the Ooijen levee also contains sediments formed during the Holocene, that is, since the early Mesolithic period) and 420 cm (De Ham core comprises sediments deposited from the early Allerød up to the middle Holocene). The sampling resolution is 2-cm in the three studies, and each analyzed sample represents ~30-year average sedimentation at the Well-Aijen and De Ham cores and ~80-year average sedimentation at the Ooijen levee section. Using these high-resolution sedimentary records spanning the Lateglacial to Holocene time period, we infer the flooding phase conditions on a centennial to millennial time scale. In chapter 5, we first synthesized the reconstructed Lower Meuse flooding phases. Next, we compare them to the climatic proxy records (grand solar minima, North Atlantic ice-rafted debris record, Greenland isotope and glaciochemical records, and the North Atlantic Oscillation index) and paleohydrological records (storminess records, lake-level variation records, and fluvial flood records) from the European continent. These paleoclimatic data served a comprehensive comparison and discussion in understanding the causality of the Lower Meuse floods and climate-human impacts.

The traditional methods, for example based on the (coarse) sand component content, median grain size or P90 values (the grain size corresponding with the 90th percentile of the cumulative grain-size distribution), were found not to be applicable in the paleoflood study on the Well-Aijen core sediments. This is because, first, the average sand (>63 μm) content of the flooding sediments (above the channel bed sediments at 626-610 cm that mainly contain the gravels and coarse sands) is 3.8 vol. %, and this value is even lower (<1 vol. %) in the upper half of the core. Clay (<4 μm) and silt (4-63 μm) are the main components. This sediment composition characteristic means that the coarse portion (>63 μm or >125 μm) of the grain-size data is unrepresentative to represent the flooding signal, and cannot be

directly used. In addition, both the clay and silt components cannot be used in flood identification either, because they can occur in small floods and large floods. Second, the presence of post-depositional Fe-Mn concretions and resistant organic particulate materials contaminated the coarse end of grain-size data, and this means that the P90 values are not reliable. Based on these considerations, we rejected to directly use the raw grain size data from the Well-Aijen core sediments in the flooding study. We proposed a new method, the Flood Energy Index (FEI), to identify the high flooding phases and to resolve the above issues. The main principle of this method is to calculate the ratio of the coarse grain size end members (the flooding signal) over the other grain size end-member components, to split/separate the grain size dataset into suspended load and bed load. High FEI values indicate phases of increased flooding magnitude. This approach also forms the foundation of the methods used in the paleoflood studies in the Ooijen and the De Ham sites.

The Well-Aijen paleochannel contains a fairly continuous depositional record of Meuse flood deposits from ~8600 cal BP to modern times. Thus, the depositional process of the core sediments can be regarded as a typical case of Holocene channel infilling and floodplain evolution in the Lower Meuse catchment. Based on the lithology and analyzed sedimentary parameters, six lithostratigraphic units were distinguished. The basal unit 1 consists of coarse sands and gravels which formed as channel-bed deposits. The lower organo-clastic part of the sequence (units 2–3) represents a fluvio-lacustrine swamp environment, which formed after channel abandonment in the early Holocene. During this time-interval natural depositional processes dominated over limited human impact. The upper clastic part of the sequence (units 4–6) was formed since the Bronze Age, and was affected by enhanced human influence, which accelerated sediment accumulation rates. Multi-centennial periods with increased floods were identified at c. 8500, c. 8000, c. 7600, c. 7000, c. 5900 cal BP. This was followed by a low sedimentation rate and low flooding activity until c. 2800 cal BP which can be linked to the 2.8 ka climate anomaly. The last three inferred flooding phases occurred at c. 2000, c. 700 and c. 300 cal BP and coincide with the Roman Period, Medieval Warm Period and Little Ice Age, respectively. Rapid sediment accumulation rates and more severe floods reveal increased fluvial instability in the late Holocene, also indicating that humans had begun to have a profound influence on fluvial dynamics.

At the Ooijen site, the Holocene flooding regime was investigated by analyzing the sediments from a different geomorphological setting: a levee. The levee acts as the connector between the channel and floodplain, but it has obtained relatively less attention in paleoflooding studies due to the limited sediment preservation potential on it. Three sections were sampled from a trench for archeological research which was oriented perpendicular to the river channel. The sampled site on the NW part of the levee preserves a continuous Holocene sedimentation profile, and this finding is in contrast to the former investigation on the SE part of the levee which claimed little sedimentation had taken place in the last seven thousand years. Starting from the middle Mesolithic, the results reveal a gradually decreasing flooding regime, during which the young levee was low. In this period, humans began to occupy the

levee, but the anthropogenic influence on the landscape in the Lower Meuse valley was still low. Subsequently, the Neolithic and Bronze Age periods experienced a low, but gradually increasing flooding regime. The Iron Age witnessed the start of a period of enhanced flooding with the deposition of coarser sediments. Intense flooding conditions lasted through the Roman Period until the Dark Ages, during which the Lower Meuse experienced a phase of weakened flooding intensity. From the middle to the late Middle Ages, the flooding conditions intensified again. We propose that the coarsening-upward trend and high accumulation rates since the Iron Age resulted from increased flooding and high sediment supply caused by human impacts on the Meuse catchment. The flooding phases derived from levee sediments agree well with those derived from floodplain sediments at Well-Aijen. This implies that well-preserved levee sediments, along stable channel courses, can be a suitable candidate for paleohydrological studies.

The De Ham core contains sediments deposited in an abandoned Meuse channel during the late Allerød and Holocene time interval. The study of the core sediments focused on the late Allerød-Younger Dryas interval, as we expected that this dramatic climatic oscillation could have been recorded by the fluvio-lacustrine sediments. In addition, this study supplements previous geomorphological studies which indicated increased flooding and incision during the Younger Dryas. Based on end member modelling of the grain-size distribution results, flood-energy indexes were constructed for both the suspended load and bed-load sediment fractions. Both the indexes show a quick increase of the flooding energy at the start of the Younger Dryas. In addition, the short intra-Allerød cold period was also reflected by the sedimentary record (organic matter content, calcium carbonate content, AP/NAP in pollen diagram, and biogenic isotope $\delta^{13}C$ and $\delta^{18}O$). The match of the Lower Meuse flooding signal records with various regional climate change proxy records indicates a rather sensitive response of the hydrological processes to the climate forcing.

In chapter 5, the two Holocene flood records (Well-Aijen core, Ooijen site) and the Lateglacial flood record (De Ham core) make up a 13,000-yr Lower Meuse flood record. This enables a comprehensive discussion to understand the climate forcing and anthropogenic impact on the Lower Meuse paleohydrology. The main reason to account for the rapid intensification of flooding at the late Allerød to the Younger Dryas transition is the increased snow-melt water, combined with reduced soil-water infiltration and storage capacity, to trigger higher peak discharges during spring. Overall, the two Holocene flood records agree well and show increased flooding phases at 8700-8400 cal BP and 8100-7500 cal BP, 6100-5000 cal BP, 3000-2600 cal BP, 2200-1900 cal BP (Roman Period), 1500-1200 cal BP (Dark Ages), 900-600 cal BP (Middle Ages) and 500-200 cal BP (Little Ice Age). The late Holocene flooding record is characterized by rapid changes in the flooding regime, with more episodic variability and the occurrence of high-magnitude floods, compared to the long-term phasing and relatively lower magnitude floods that occurred during the early and middle Holocene. We suggest that solar forcing played a dominant role through the coupling of the atmospheric circulation and the cooling of the North

Atlantic Ocean surface. The coupling of atmospheric circulation with long-term North Atlantic surface temperature dominates the European climate, and this can be expressed by the NAO which controls the westerlies track changes. However, the associated high and low latitudes atmospheric and ocean circulation systems (i.e., Hadley cell, subpolar and subtropical gyres) could also exert a profound impact both on the Northern and Southern Europe hydroclimate variabilities. The high magnitude and more frequent floods in the Lower Meuse during the late Holocene are attributed to the anthropogenic-induced land-use changes which led to a more climate-susceptible fluvial system. That is, the intense human activity in the late Holocene increased the vulnerability of the fluvial system. The consequence is that (compared to the times before) an increase in precipitation could induce a flood with larger magnitude. Therefore, we conclude that the late Holocene flooding phases were climatic-induced but significantly intensified by anthropogenic impacts. The quick response of the Lower Meuse hydrological variability to the climate variations is meaningful for future flood risk assessments.

1. Introduction

1.1. Background

Flood control is a national policy of the Netherlands, since about two thirds of the country (mainly the western area) is vulnerable to flooding due to the low altitude and flat terrain. This topography means that floods, caused by coastal storm surges and inland rivers, usually pose a threat to Dutch people and community. Examples are the 1953 North Sea flood catastrophe, and the 1993 and 1995 Meuse and Rhine flood hazards. In this context, global warming, accompanied by the rising sea level (caused by ice melting and thermal expansion) and increased precipitation events, is a major threat. In addition to the implementation of flood prevention works (i.e., the Delta Works; enlarging of river dykes) that can directly protect the land from flooding threats, accurate flood hazard and risk assessment are also important for the habitable environment and economic development. However, robust assessments of present and future flood hazard are often limited by the scarcity and short time span of the instrumental time series. For the rivers, the understanding of the past hydrological variability and its causality with dramatic climate changes and human disturbances (especially in the last two millennia) aids in predictions and anticipations of flood hazards (Baker, 2008).

From 1980 onwards, studies in fluvial paleohydrology were conducted to estimate recurrence intervals for large floods which exceed the length of instrumental and historical records (Kochel and Baker, 1982; Baker et al., 1983a; Baker et al., 1983b). These early pioneering case studies utilized the slackwater deposits as a paleoflood stage indicator and as input for discharge calculations, combined with the slope-area method (Kochel and Baker, 1982; Ely, 1997). The easy discrimination of slackwater deposits from non-flood sediments makes it a widely-used paleoflooding indicator (Ely, 1997; Yang et al., 2000; Huang et al., 2012). However, the use of slackwater deposits in low-relief landscape, i.e. at floodplains, is not always practical, because gradually attenuated overbank flow carries sediments away from the river channel more regularly, and the accumulated deposits have adopted a relatively homogeneous structure. This setting makes recognition of clear sequences of flood deposits, dating and assigning a flood stage to reconstruct paleodischarge and assessment of recurrence frequency, a challenging enterprise. This issue can be resolved by using recent methodological advancements which involve the processing of grain-size datasets by performing end member modelling (Prins and Weltje, 1999; Weltje and Prins, 2003) or principal components analysis (i.e., Munoz et al., 2015; Toonen et al., 2015a; Munoz et al., 2018). In these cited three studies, the coarse grain-size components (coarse end members and/or normalized EM scores) are related to the discharge of historical flood events. Compared with the direct use of other grain-size parameters (i.e., P90, median grain size or the mean of the sand fraction), using coarse end members or normalized EM scores produce robust outcomes in paleodischarge calculations (Toonen et al., 2015a; Munoz et al., 2018).

By any means, the main principle of reconstructing paleofloods by using grain size lies in correlating the coarse components to floods. Alternatively, layered organic depositions (i.e., peat bed) have also been regarded as an indicator of a reduction in flood magnitude and frequency (i.e., Nesje et al., 2001; Ishii et al., 2017). However, the flood indicators mentioned above, are not always present in the flood deposits, or they do not record flooding properly. For instance, compared with the proximal channel and point bar-swale environments, the distal part of the floodplain setting receives less sand input. In this location, the generally fine-grained sediments have a relatively homogeneous structure, which makes it difficult to establish a link between the coarse components with floods. On the other hand, the gradually accumulated sedimentation on the levee and the floodplain, also can bias the paleoflood reconstruction. To be specific, channel downcutting or widening can happen during channel evolution both in long- and short time spans, for example during extreme floods. The impact of changes in river type (meandering vs braided), channel width/depth ratio, and vertical accretion of floodplain or levee sediments can disturb the correlation between discharge/magnitude and grain-size parameters. For example, channel downcutting and/or widening can result in a higher bankfull discharge and flooding threshold. Thus, two flood events, before and after a change of the flooding threshold, have different magnitudes, although they resulted in comparable flooding deposits (similar grain-size compositions). Further, paleodischarge estimations based on single grain-size parameters could suggest that there is no apparent difference between the two events. Therefore, we argue for using the complete grain-size distribution in paleoflood reconstruction and for taking into account channel morphological changes. This is mainly achieved with the combination of end-member modelling analysis. The addition of complete end members to reconstructing the FEI index, which is the main methodology in this thesis, is able to consider a complete flooding water transporting mechanism. For the Lower Meuse, fluvial studies conducted in the past decades have concentrated amongst others on channel migration, river terrace formation, and vegetation development during the Weichselian, especially during the Last Glacial-Interglacial transition (Bohncke et al., 1993; Kasse et al., 1995; Huisink, 1997; Tebbens et al., 1999; Hoek et al., 2017; Woolderink et al., 2018). However, little attention has been paid to the long-term paleoflooding variations of the Lower Meuse, and this impedes a correlation between fluvial flooding activity and climate-human impacts. This thesis provides a first long-term flood record for the Lower Meuse for the Late Glacial and Holocene, based on a promising and meaningful method for flood identification. In the scope of this thesis, the results and conclusions emphasize the great potential of the Lower Meuse fluvial sediments in registering the external forcings signals.

1.2. The research area

The Meuse originates in northeastern France, flows through the uplifting Ardennes and subsiding Roer Valley rift system, and finally debouches into the North Sea. It has a length of 900 km and a catchment area of 33,000 km2. As a rain-fed river, the annual average discharge of the Lower Meuse is about 230 m3/s. The study area is situated in the Lower Meuse Valley, between Aijen and Ooijen in the north

of Limburg Province (Fig. 1.1A). Tectonically, this area lies on the Venlo Block of the Roer Valley Rift System (Fig. 1.1A). The relatively subsiding Venlo Block is separated from its adjacent uplifting Peel Block by the Tegelen Fault Zone (Van Balen et al., 2005). Geological evidence show that the Venlo Block is relatively stable. The average subsidence rates in the Roer Valley Graben and the Peel Block are ~88 mm/ka and ~46 mm/ka respectively during the Quaternary (Houtgast and Van Balen, 2000). The subsidence rate for the Venlo Block is possibly even lower. The river channel along the study sites has no or limited lateral migration (Woolderink et al., 2018).

In this area, the morphology is characterized by a series of river terraces which formed due to incision during the Lateglacial period (Kasse et al., 1995; Woolderink et al., 2018). At the start of the Late Glacial, during the Bølling interstadial period (14.7-14.1 ka cal BP), temperature and precipitation increased and the braided river system gradually changed into a low-sinuosity meandering system which coincided with a phase of incision. This transitional system eventually evolved into a high-sinuosity meandering system in the following Allerød interstadial period (14.0-12.9 ka cal BP). During the Allerød, lateral channel migration sediments accreted on the channel point-bar forming up to 7.5-m-thick fining-upward sequences (Van Huissteden and Kasse, 2001). The warm Allerød interstadial is followed by the relatively cold Younger Dryas stadial period, during which the Meuse changed to a multi-channel or braided system. As a consequence, many of the pre-developed sinuous channels were eroded and only remnant scars are visible at present. Incision of the Lower Meuse during the late Younger Dryas resulted in aeolian deflation of sediment from terrace remnants and (seasonally) exposed river bars, forming parabolic aeolian dunes on the eastern bank of the river (Fig. 1.1B) (Bohncke et al., 1993; Kasse et al., 1995). At the transition to the warm Holocene, the braided river system could not continue to exist due to the combined effect of the rapid temperature increase, the decrease in peak discharge and the vegetation recovery. At the start of the Holocene, local permafrost disappeared and the increase of the infiltration capacity of the soil led to lower peak discharges and a higher base flow compared to the Younger Dryas (Van Huissteden and Kasse, 2001). Because of the rapid reforestation during the early Holocene, the sediment supply decreased again and the Meuse river incised.

1.3. Outline

In chapters 2 and 3, we study the Holocene flooding-phase records that were derived from the sedimentary infill of an abandoned channel on a floodplain (Well-Aijen core, Fig. 1.1B) and from levee sediments (Ooijen site, Fig. 1.1B), respectively. In Chapter 4, we extend the Lower Meuse flood record to the Lateglacial period, by studying fluvial sediments from an Allerød abandoned channel infill (De Ham core, Fig. 1.1B). In chapter 5, we synthesize the Holocene and Lateglacial flooding phases. This is followed by a comparison of the flood records with the climatic proxy records (grand solar minima, North Atlantic ice-rafted debris record, Greenland isotope and glaciochemical records, and the North

Atlantic Oscillation index) and paleohydrological records (storminess records, lake-level variation records, and fluvial flood records) from the European continent. These paleoclimatic data serve a comprehensive comparison and discussion in understanding the causality of the Lower Meuse floods and climate-human impacts.

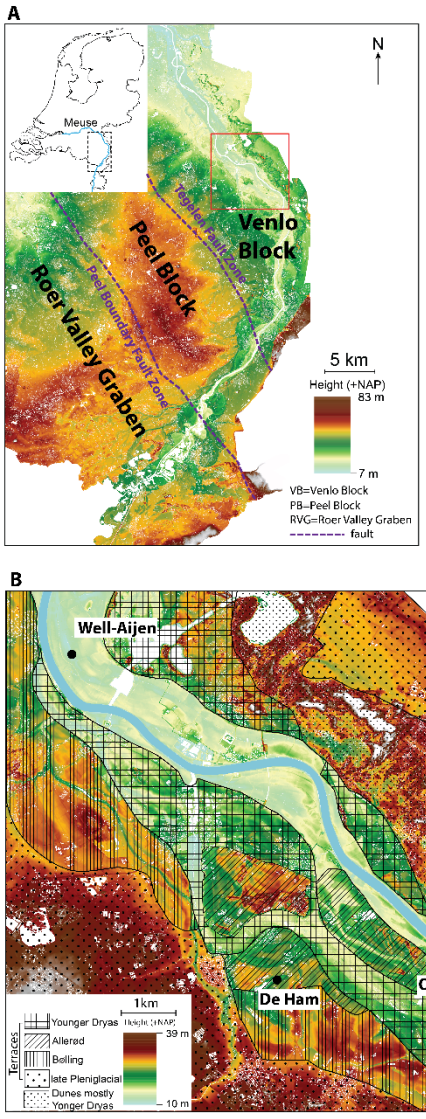

Figure 1.1. Digital elevation map of the study area. (A) The Lower Meuse valley (dashed box in the insert) and the tectonic blocks. The study area lies on the Venlo Block which is separated from its adjacent uplifting Peel Block. (B) The three investigated sites: Well-Aijen core locates on the floodplain, and the Ooijen section sites on the levee. De Ham core was retrieve from an abandoned channel which is located on the Allerød river terrace. East of the Meuse presents the Younger Dryas cover sands.

2. An improved method for paleoflood reconstruction and flooding phase identification, applied to the Meuse River in the Netherlands

Published as: Fei Peng, Maarten A. Prins, Cornelis Kasse, Kim M. Cohen, Nathalie Van der Putten, Jeroen van der Lubbe, Willem H.J. Toonen, Ronald T. van Balen (2019). Global and Planetary Change 177, 213-224

Abstract

This study investigates Holocene floodplain evolution and flooding phases as experienced in the Lower Meuse catchment, primarily based on grain-size distributions of channel-fill and floodplain deposits in sediment cores. The presence of post-depositional Fe-Mn concretions and resistant organic particulate materials impedes the direct use of grain-size data. By combining end-member modelling results with laboratory observations, we have constructed a Flood Energy Index (FEI), which allows identification of phases of past increased flooding from the grain-size signal. Since concretions and organic-rich sediments regularly occur in floodplain sediments, we emphasize that the quality of a grain-size dataset should be assessed prior to its use for reconstruction of flood events. We suggest that the new approach has potential to become standardized within paleoflood research. The temporal variation of FEI in Meuse sediment cores highlights multi-centennial flooding phases occurring at c. 8500, c. 8000, c. 7600, c. 7000 and c. 5900 cal BP within the fluvio-lacustrine environment (early–middle Holocene). The record of low flood activity in the Subboreal is attributed to a cooler and dryer climate anomaly after the Holocene Climatic Optimum. In the late Holocene, the first flooding phase occurring at c. 2800 cal BP can be linked to the 2.8 ka climate anomaly. During the last two thousand years, the variation of FEI index reveals oscillating flood regimes in the Lower Meuse floodplain. The last three recorded flooding phases most likely coincide with the Roman Period (c. 12 BCE–250 CE), the Medieval Warm Period (c. 950–1400 CE) and the Little Ice Age (c. 1400–850 CE). Despite uncertainty in the age-model, the rapid accumulation rate and amplified flood magnitudes imply increased fluvial instability during the late Holocene, indicating that humans exerted a profound influence on fluvial dynamics in the Meuse.

Keywords: Grain-size distribution, End-member modelling, Floodplain evolution, Flood energy index, Holocene paleofloods

2.1. Introduction

Fluvial systems are susceptible to climate change and human activity within a multi-millennial time scale in the Holocene (e.g., Macklin et al., 2012; 2015). A change in the frequency and magnitude of floods is the main direct driver that determines the response of river systems to climatic change (Ward et al., 2008; Macklin et al., 2012; Starkel et al., 2015). Therefore, fluvial systems can act as recorders

of climate and human-induced changes and the deposits can thus be used to infer past climatic conditions and human impacts on the fluvial system (e.g., Ely, 1997; De Moor et al., 2008).

Since Baker et al. (1983a) introduced the analyses of slackwater deposits from confined bedrock gorge settings in paleohydrological research, these deposits have been widely used to reconstruct past floods and flooding regimes, because they can be easily distinguished from other sediment units by applying a series of criteria, such as lithology, grain-size, sediment color, sedimentary texture and structure, and interbedded palaeosols (Ely, 1997; Yang et al., 2000; Huang et al., 2012). However, the use of slackwater deposits in a low-relief landscape that characterizes the lower Meuse floodplain is impractical, because the gradually attenuated overbank flow carries sediments away from the river channel more regularly, and the accumulated deposits feature a relatively homogeneous structure. This setting makes recognition of clear sequences of flood deposits, dating and assigning a flood stage to reconstruct paleodischarge and assessment of recurrence frequency challenging. Alternative sedimentary archives (e.g., gyttja, peat and varved lacustrine sequences) have been used for reconstructing past hydrological events. For instance, well-preserved peat sequences in floodplains and lakes can be used to study flooding magnitude and frequency (i.e., Ishii et al., 2017). Furthermore, grain-size variation from appropriate sedimentary settings is suited to interpret episodic, high-magnitude floods because the amount of coarse grains entrained with suspended materials increases with flood magnitudes, and these coarse sediments can settle out from suspension relatively quickly (Lim et al., 2013; Toonen et al., 2015b). However, in a distal floodplain setting the sand input is limited. Therefore, linking the coarse-grained components solely to large floods can lead to misunderstanding because distal floodplain sites do not contain a substantial amount of sand. In addition, the conventional use of grain-size information in paleoflood event reconstructions generally incorporates the entire grain-size distributions (GSDs) without considering the reliability of the dataset (i.e., Toonen et al., 2015b). Moreover, iron and manganese (Fe-Mn) concretions in fluvial sediments, which are broadly associated with soil formation and gley phenomena, can be hard to remove/dissolve during sample pretreatment (Schwertmann and Fanning, 1976). To our knowledge, there is nothing reported concerning this issue in published flood reconstructions. The aforementioned issues can however greatly affect the reliability of paleoflood reconstructions in floodplain environments. Hence, caution should be taken when interpreting the grain-size data and linking such information to palaeoflood magnitudes.

In the Netherlands, the instrumental flood record is relatively short. The earliest instrumental discharge record for the Meuse River dates back to 1911, and older historical written flood records start from the 13th century (Buisman, 1995; Glaser and Stangl, 2003). There is no one long-term (millennial scale) flood reconstruction for this fluvial system. As a rain-fed river, the discharge of the Meuse reacts quickly to precipitation changes (Kasse et al., 1995; Ward et al., 2008). Therefore, the information derived from a paleoflood study holds a great potential in reflecting the long-term changes of past precipitation.

In this study, we address the above-mentioned challenges to a paleoflood record for the Lower Meuse. By analyzing the sedimentological properties of a floodplain channel-fill core at 2-cm resolution, we minimize unwanted signals related to the presence of Fe-Mn concretions and organic remains that survived sample preparation. The applicability of the proposed method is evaluated prior to identifying the flooding phases for the Lower Meuse. Given the fact that grain-size data can be biased by post-depositional concretion formation and/or high amounts of organic matter in other sedimentary contexts, we emphasize the quality of a grain-size dataset should be assessed prior to using it for flooding reconstructions. We suggest the new method and approach have potential to be standardized in paleoflood research elsewhere. As a building block for future work and a paper that emphasizes on methodology in paleoflood study and its application in the Lower Meuse, we do not detail the human and climatic influences on the Meuse catchment during the Holocene. This synthesized work will be present in the next step, combined with a new sedimentary record from the same river.

2.2. Setting

The Meuse originates from northeastern France and flows northward through Belgium, passing the uplifted Ardennes. After initially continuing northward in the Netherlands, the flow direction changes to the west before entering the low-relief Rhine-Meuse delta plain and debouching into the North Sea. The study site, Well-Aijen (referred to as WA hereafter), is located in the Limburg Province of the southern Netherlands, and about 45 km upstream of the Rhine-Meuse delta apex. Tectonically, this site lies on the Venlo Block of the Roer Valley Rift System (Fig. 2.1a). The relatively subsiding Venlo Block is separated from its adjacent uplifting Peel Block by the Tegelen Fault Zone (Van Balen et al., 2005). Geological studies indicate average subsidence rates in the Roer Valley Graben and the Peel Block are ~88 mm/ka and ~46 mm/ka respectively during the Quaternary (Houtgast and Van Balen, 2000). The subsidence rate for the Venlo Block is possibly even lower, and there is no evidence indicating tectonic movement during the Holocene.

In the Roer Valley Graben the Meuse has a broad Holocene floodplain (~3.5 kilometers wide) due to the highly sinuous channel. On the Peel Block the Holocene floodplain is very narrow (~500 meters wide) along the relatively straight, incised channel. On the Venlo Block, where WA is situated, the floodplain is gradually widening towards the Rhine-Meuse delta. The Holocene floodplain at WA is confined by Late Glacial terraces and superimposed inland dunes (Fig. 2.1b). Directly to the east, aeolian inland dunes derived from braided river deposits were formed during the Younger Dryas (Kasse et al., 1995). During the transition from the Late Glacial to the Holocene, the Meuse changed from a braided to a meandering system in response to climate change (Kasse et al., 1995; Huisink, 1999; Tebbens et al., 1999), and as a consequence, many braided channels were abandoned (Fig. 2.1b). The study area has been extensively investigated by means of paleogeographic mapping, establishing regional pollen and constructing frameworks for prehistorical human activity (e.g., Zuidhoff and Van der Velde, 2008; Bos et al., 2014; Bos and Zuidhoff, 2015; Hoek et al., 2017; Isarin et al., 2017; Rensink,

2017; Woolderink et al., 2018). In 2011, an abandoned paleochannel in WA was studied using hand-drillings and a trench. Archeological finds indicated that this trench comprises a sediment record that covers the last ~8000 years (Bos and Zuidhoff, 2015). Thus, the WA could be an ideal site for tracing past fluvial activity. According to the Late Glacial-to-Holocene terrace stratigraphy (e.g., Hoek et al., 2017; Woolderink et al., 2018), it follows that the WA channel was active during the Preboreal and Boreal (early Holocene). Radiocarbon dating together with a palynological study confirm its abandonment in the late Boreal (Bos and Zuidhoff, 2015). Since then, the abandoned channel received sediments when bankfull discharge was exceeded during flooding. After the abandonment, the main channel of the Meuse was positioned roughly at the present location (Kasse et al., 1995), and no apparent migration has been recognized. Our observations support this. First, Mesolithic and Neolithic archeological sites were preserved in the area between the WA paleochannel and the present river (Bos et al., 2014; Bos and Zuidhoff, 2015), implying there was no eastward migration in the past. Second, the existence of paleochannel relicts between the studied paleochannel and the Late Glacial terraces precludes the westward erosion after the channel abandonment (Fig. 2.1b).

2.3. Material and methods

2.3.1. Coring and scanning

In 2011, core WA11 was drilled using a Begemann coring device at the deepest part of the WA paleochannel to produce a record for a paleoecological study (Bos and Zuidhoff, 2015). In 2016, a second core (WA16) was retrieved from the same paleochannel, 14 m NW of core WA11 site. The two cores are aligned parallel to the present river flow direction (Fig. 2.1b). Both sediment cores reached the coarse-grained channel bed and have respective lengths of 6.29 m (WA11) and 6.26 m (WA16). The top 30 cm of core WA16 was discarded because this interval represents soil that is heavily disturbed by modern farming activities.

Core WA16 was recovered using PVC tubes with an inside diameter of 66 mm. It was transported to TNO Geological Survey of the Netherlands, where it was split, described, photographed (registered as core B52E3302) and sampled. One core-half was used for sampling, the other half was scanned with a GEOTEK Multi-Sensor Core Logger at VU Amsterdam at 0.5 cm resolution to obtain a record of magnetic susceptibility and gamma-ray bulk density. Before scanning, the surface of the core halves was cleaned using a plastic blade. The magnetic susceptibility was measured using a Bartington MS2E point sensor and the bulk density record was corrected for variations in sediment thickness according to the Geotek calibration protocols (http://www.geotek.co.uk/support/downloads/).

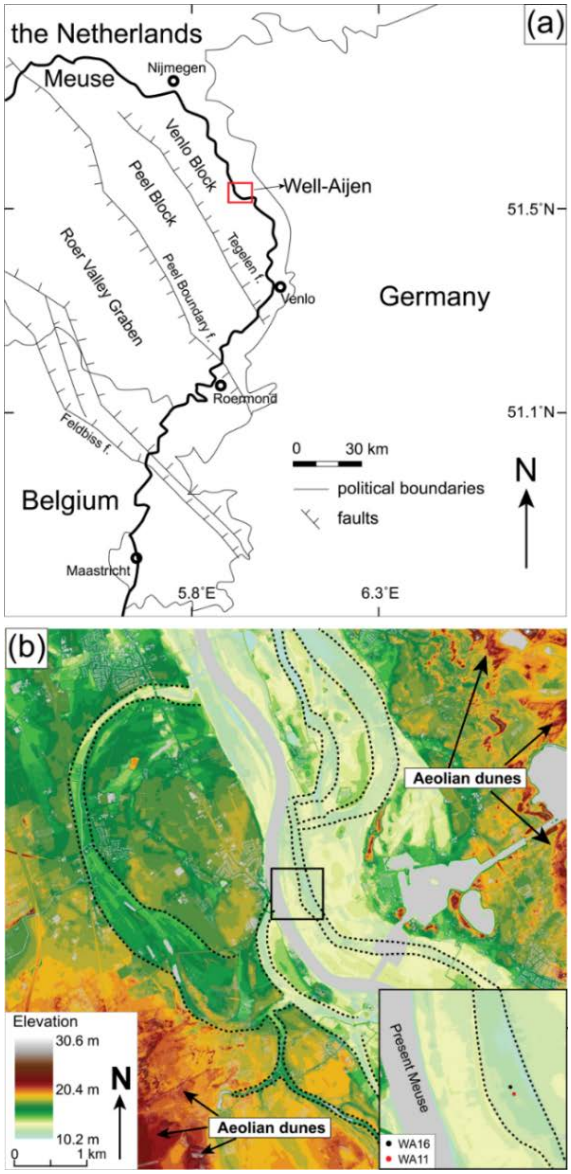

Figure 2.1. (a) Location map of the study area and major fault zones in the southern Netherlands. The research site (red box) is located on the subsiding Venlo Block which is separated from the southwestern Peel Block by the Tegelen Fault Zone (Van Balen et al., 2005). (b) Digital elevation map (https://ahn.arcgisonline.nl/ahnviewer/) shows the Well-Aijen Holocene floodplain elevation. The light-yellow area depicts the distribution of the Holocene floodplain. The dashed lines outline the abandoned channels. East and west of the Meuse Late Glacial terraces, aeolian dunes and cover sands are present (Kasse et al., 1995; Woolderink et al., 2018). The insert shows core WA11 and core WA16 at the WA paleochannel, note that the two cores are aligned parallel to the river flow.

2.3.2. Grain-size analysis and end-member modelling

We obtained 292 samples for grain-size analyses, continuously sampled with boundaries placed at 2 cm intervals. The method described in Konert and Vandenberghe (1997) was used to pretreat the samples for grain-size analysis. Samples from the upper 340 cm clastic sequence were successively pretreated with 10 ml 30% H_2O_2 and 5ml 10% HCl to remove organic matter and calcium carbonates respectively. Additional H_2O_2 was added to the organic-rich samples from the lower organo-clastic part of the core (below 340 cm) to remove excess organic matter. Grain-size distributions (GSDs) ranging from 0.1 to 2000 μm were measured with a Sympatec HELOS KR laser-diffraction instrument at the VU Amsterdam.

After pretreatment, we observed that 43 samples in the interval between 40-210 cm still contained sand-sized undissolved concretions, and several samples from the lower 300 cm still contained resistant particulate organic remains. In order to understand their physicochemical properties, concretions from six samples were analyzed with a scanning electron microscope (JCM-6000Plus) at the VU Amsterdam.

The results show that concretions from the same and from different depths can have different chemical compositions (supplementary material, Fig. S2.8.3). It was suspected that these post-depositional concretions and organic remains would affect the 'true' GSDs. Hence, another six samples were taken from both the clastic and organo-clastic part of core WA16 and pretreated with different methods to evaluate the reproducibility of the GSDs. These testing methods involve the use of ultrasonic homogenizer and additional reagents (supplementary material, Table S2.8.1). The tests show that none of the methods could completely dissolve the concretions.

We deployed end-member (EM) modelling to decompose the GSDs into a set of end members (Prins and Weltje, 1999; Weltje and Prins, 2003). This approach has been designed to offer the simplest explanation for the observed variations in GSDs in terms of grain-size EM. This EM modelling approach has been successfully applied for extracting representative paleoclimate indicators and detecting mixing patterns of sediments supplied from multiple sources (e.g., Prins et al., 2007; Shang et al., 2016). Also, the EM modelling has been applied to study transport processes and fluvial dynamics (Toonen et al., 2015b), thus demonstrating that the use of EMs is geo-genetically meaningful and not merely a descriptive methodology. Here, we used the AnalySize package (Paterson and Heslop, 2015; Van Hateren et al., 2018) to obtain EMs and to determine their proportional contributions in each grain-size sample. The coefficients of determination (r^2) were calculated to assess the minimum number of EMs (cf. Prins and Weltje, 1999). The coefficients of determination represent the proportions of the variance of each grain-size class that can be reproduced by the approximated data. This proportion is equal to the squared correlation coefficient (r^2) of the input variables and their approximated values (Prins and Weltje, 1999; Prins et al., 2000).

2.3.3. Thermo gravimetric analysis

A Leco TGA701 analyzer at VU Amsterdam was used to determine the organic matter and calcium carbonate content (Heiri et al., 2001). To achieve greater contact area and better equilibrium conditions, the samples were ground into powder after being dried in a stove at 50°C overnight. Each analysis started with the removal of residual moisture by purging the closed environment during heating to 105°C. The second heating step was performed in a pure oxygen atmosphere, the temperature was ramped up to 330°C, combusting the labile organic matter. At the third step, under air atmosphere, the reaction temperature rose to 550°C to combust the resistant organic matter. The last heating step was performed in a CO_2 atmosphere, by heating up the sample to 1000°C, and different types of carbonate were dissociated. In this manner, the total organic matter (TOM, sum of labile and resistant organic matter) and the carbonate contents were obtained.

2.3.4. Geochronology

2.3.4.1. AMS ^{14}C dating

Four AMS ^{14}C dates were obtained from the lower organo-clastic part of core WA11 by Bos and Zuidhoff (2015) (Table 2.1). We visually compared the two cores as the first step to understand the sedimentary lithofacies. The correlation of the cores shows that the sedimentary lithofacies and their marker horizons in the two cores are essentially the same (supplementary material, Fig. S2.8.1). To further constrain the chronology for core WA16, four terrestrial plant macrofossil samples were picked from core WA16 and ^{14}C dated at University of Groningen (Table 2.1). An age-depth model was constructed for the organo-clastic part (units 2 and 3) and the basal clastic part of unit 4 by using Bayesian statistics (Blaauw and Christen, 2011) with the IntCal13 calibration curve (Reimer et al., 2013).

2.3.4.2. Pollen zones subdivision and additional age control methods

No identifiable organic matter for ^{14}C dating was present in the upper 340-cm clastic part of core WA16. Therefore, the established Holocene regional biostratigraphy, pollen assemblages of core WA11 (Bos and Zuidhoff, 2015), and a tuned age model based on sedimentary proxies for accumulation rates were used for chronology (cf. Minderhoud et al., 2016). The pollen assemblage zones and archeological finds have subdivided the sedimentary stratum according to main cultural and climatic zones (supplementary material, Fig. S2.8.5). Specifically, paleobotanical interpretations reveal that the condensed interval of 334-314 cm and 314-274 cm correspond with the Bronze Age (*c*. 4000-2750 cal a BP) and Iron Age (*c*. 2750-2000 cal a BP), respectively. The shallowest sample allowing for pollen investigation originates from 274 cm and is indicative for the inception of the Roman Period (*c*. 2000 a BP). Gleyic oxidation, variable textural and grain-size variation of the upper clastic sequence indicate a dynamic sedimentary environment. Therefore, we link the granulometry-based parameters (FEI index, see 4.4) with accumulation rate to establish a tuned age model for interval of 314-70 cm (section 2.8.4 in the supplementary material). This method is modified after Minderhoud et al. (2016), in which the loss-on-ignition is linked with the accumulation rate. The modelling method described there can also be performed on other 'continuously sampled' sedimentary proxies for vertical aggradation, for example grain-size or geochemistry data (Minderhoud et al., 2016).

X-ray fluorescence analysis (XRF) was performed on a black layer at ~70 cm depth by using the Pananalytical MagiX Pro XRF at the VU Amsterdam. The XRF results (supplementary material, Fig. S2.8.2) confirm deposition of this black layer during the period of coal mining further upstream along the Meuse in the middle 19th century (Stam, 2002).

Table 2.1. Radiocarbon dated samples from core WA11 (Bos and Zuidhoff, 2015) and WA16 (this study). Depths of dates from core WA11 were transferred to correlated depths in WA16 (Section 2.8.1 in supplementary material).

Lab code	Depth in WA11 (cm)	Depth in WA16 (cm)	^{14}C age (yr BP)	Calibrated ages (median)	Calibrated ages 2σ age ranges	Material dated
SUERC-44817	344.5	347.7	4363±35	4926	5039-4851	wood
GrM-13857		448	6090±20	6954	7006-6891	wood pieces
SUERC-44816	450.0	451	6111±35	6987	7157-6893	wood
GrM-13859		458	6140±20	7048	7157-6954	wood pieces
SUERC-44818	523.5	523	7069±35	7896	7966-7836	leaves
GrM-13860		552	7205±20	8004	8044-7964	leaves/bud scales
SUERC-44822	586.5	584.7	7848±35	8625	8755-8548	leaves
GrM-13858*		623	9095±25	10239	10267-10208	seeds/wood*
SUERC-823*	629	626	8845±35	9947	10156-9744	seeds*

* marked deepest samples might be from reworked materials

2.4. Results

2.4.1. Description of the sedimentary units

Six lithostratigraphic units were distinguished in core WA16, based on the sediment characteristics such as color, sedimentary structure, grain-size composition, organic and carbonate content, core density and magnetic susceptibility. Generally, the base of core WA16 consists of coarse sands and gravels (unit 1). They are overlain by organic-rich deposits (units 2 and 3) and clastic deposits (units 4-6) (Fig. 2.2a, b). GSDs obtained from unit 1 are strongly bimodal with modes centered around 10 and 400 μm (Fig. 2.3). In unit 2-6, the GSDs have a dominant mode at 8-20 μm and occasionally a secondary mode above ~100 μm (Fig. 2.3). Table 2.2 summarizes the granulometric information of each unit.

Unit 1 (626-610 cm) starts from the base of the core (Fig. 2.2b). This unit has a dark grey color and a rapid fining-upward trend structure (Fig. 2.4a). At the very base it consists of well-rounded gravels and coarse sands. The core density is the highest but decreases gradually upwards (Table 2.2; Fig. 2.2f).

Unit 2 (610-450 cm) exhibits dark brown and black colors. Light grey clastic laminations with millimeter-scale thickness were observed (Fig. 2.4c, d). The median grain-size curve shows minor variations around 8.1 μm (Table 2.2). This unit contains a large portion of organic matter (Table 2.2; Fig. 2.4b-d), as reflected by the increased total organic matter (TOM) values and low carbonate content (Fig. 2.2d, e). The core density is rather low, as it varies between 0.24 and 1.38 g cm^{-3}. The magnetic susceptibility is very low throughout this unit (Fig. 2.2g).

Unit 3 (450-330 cm) consists of clastic sediments mixed with organic matter and shows a similar color and structure as unit 2. Macroscopic charcoal particles are present in this unit (Fig. 2.4e, f). The occurrence and size of these charcoal particles show a decreasing trend towards the top of this unit. There is no clear change in median grain-size, but the organic matter content is significantly lower than in unit 2 (Fig. 2.2d). The calcium carbonate content co-varies with the TOM values. The core density gradually increases throughout this unit and the magnetic susceptibility is slightly higher compared to unit 2 (Fig. 2.2f, g).

Unit 4 (330-165 cm) has a gradual contact with unit 3 and is characterized by homogenous yellowish clay (Fig. 2.2a). In this unit, oxidized rusty spots occur sporadically (Fig. 2.4g, h). Notably, at 220-200 cm, the sediment color changes from yellow to brown, whereas most of the sediment properties only show gentle variations. The median grain-size shows a series of peaks at ~250 cm (Fig. 2.2c). The TOM reaches the lowest level with an average of 5.9%. The core density and magnetic susceptibility increase while the carbonate content decreases slightly (Fig. 2.2e-g).

Unit 5 (165-70 cm) is distinguished from unit 4 by its brown silty clay with loose structure and coarser grain-size (Fig. 2.4i). The median grain size varies between 8.4 and 16.5 μm (Fig. 2.2c). TOM values (around 8%) and calcium carbonate content (1.5-1.7%) remain at a low level (Fig. 2.2d, e). At about 100 cm, the median grain-size, core density and magnetic susceptibility increase significantly while carbonate content decreases slightly (Fig. 2.2).

Table 2.2. Sediment characteristics of each unit from core WA16.

Unit	Sediments type	Median (μm)	Depth range (cm)	Sand (vol%)	TOM (wt%)	Carbonate (wt%)	Density (g cm^{-3})	P_{EM1}	P_{EM2}	P_{EM3}	P_{EM4}
6	brown silty clay	8.1-8.5 (8.2)	70-30	2.11	8.9-15.1 (10.2)	1.9-2.5 (2.0)	0.06-1.90 (1.40)	33.3	45.3	9.9	0
5	brown silty clay	8.4-16.5 (10.6)	165-70	2.25	3.8-9.8 (5.0)	1.4-2.0 (1.6)	1.07-2.24 (1.71)	15.9	69.5	14.5	0.1
4	yellowish clay	5.4-19.6 (7.6)	330-165	1.53	4.2-11.4 (5.9)	1.5-2.3 (1.9)	1.11-1.99 (1.63)	48.4	45.7	5.8	0.1
3	clastic sediments mixed with organic matter	6.3-9.7 (7.5)	450-330	3.36	9.3-25.8 (17.5)	2.1-3.1 (2.5)	0.71-1.72 (1.25)	50.6	39.4	9.8	0.3
2	organic dominant infills	6.0-19.2 (8.1)	610-450	7.31	15.2-69.4 (38.0)	1.1-3.4 (2.3)	0.24-1.38 (0.88)	48.6	25.0	24.2	2.2
1	gravels and sands	9.2-335.8 (91.6)	626-610	45.65	4.7-26.4 (12.4)	1.2-2.7 (2.1)	1.05-2.05 (1.38)	12.9	10.4	10.8	65.9

Numbers in parentheses are mean values

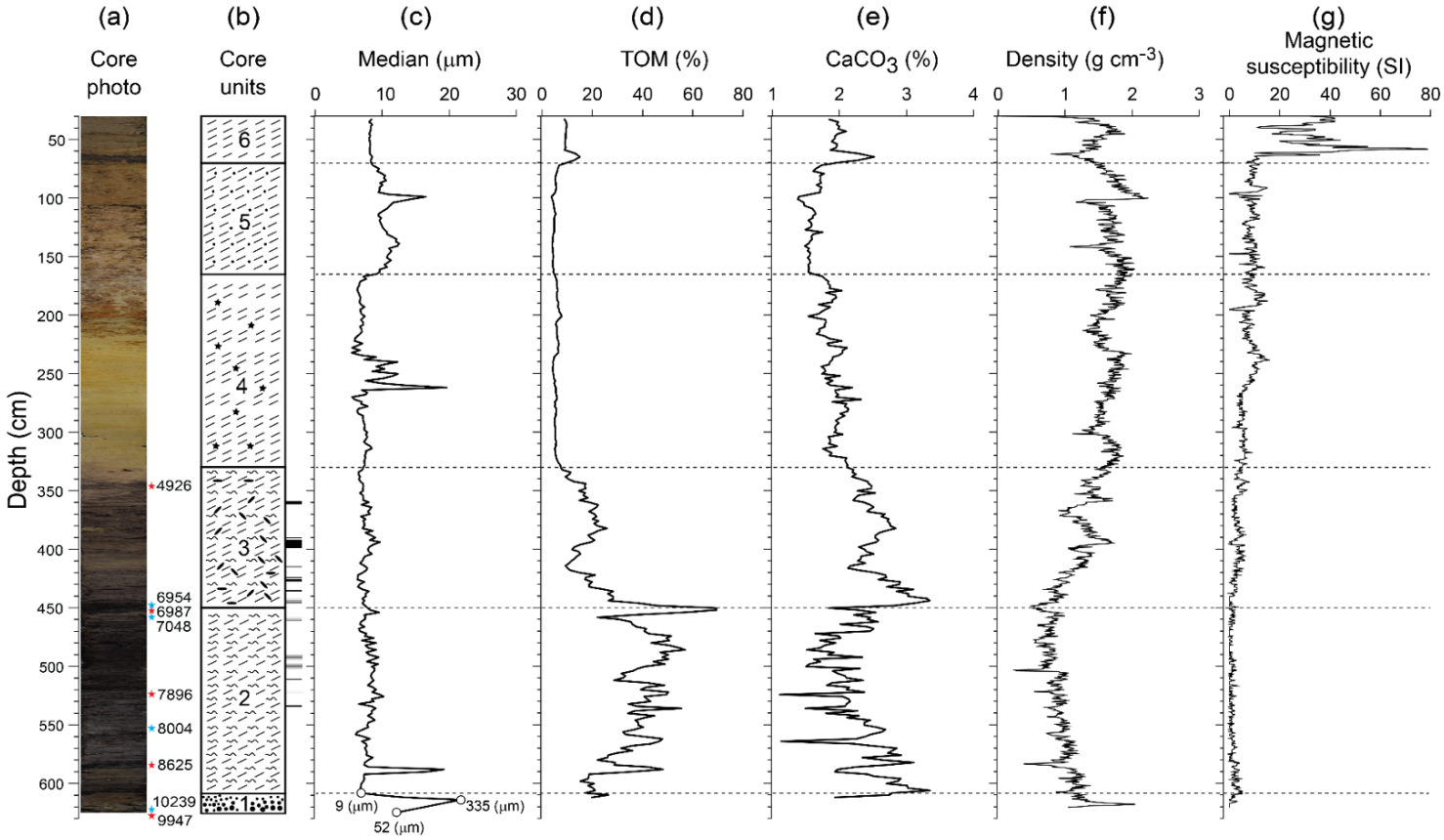

Figure 2.2. Sedimentary characteristics of core WA16. (a) photograph of the core; the asterisks show the calibrated ^{14}C dating positions from core WA11 (red, Bos and Zuidhoff, 2015) and WA16 (blue, this study); (b) shows the unit subdivision with bars along the right side marking the observed clastic flooding layers (see 4.1, thickness is not on scale); unit 1 represents channel bed sediments that are composed of gravels and sands; units 2-3 are the organo-clastic infilling of the abandoned channel; units 4-6 are flooding sediments mainly consisting of clays and silts; (c) median grain-size; (d) total organic matter (TOM) content; (e) calcium carbonate content; (f) core density; (g) magnetic susceptibility. Horizontal dashed lines mark the unit boundaries. Note that the basal part of the core (Unit 1) has not been analyzed by TGA (d, e) and core scanning.

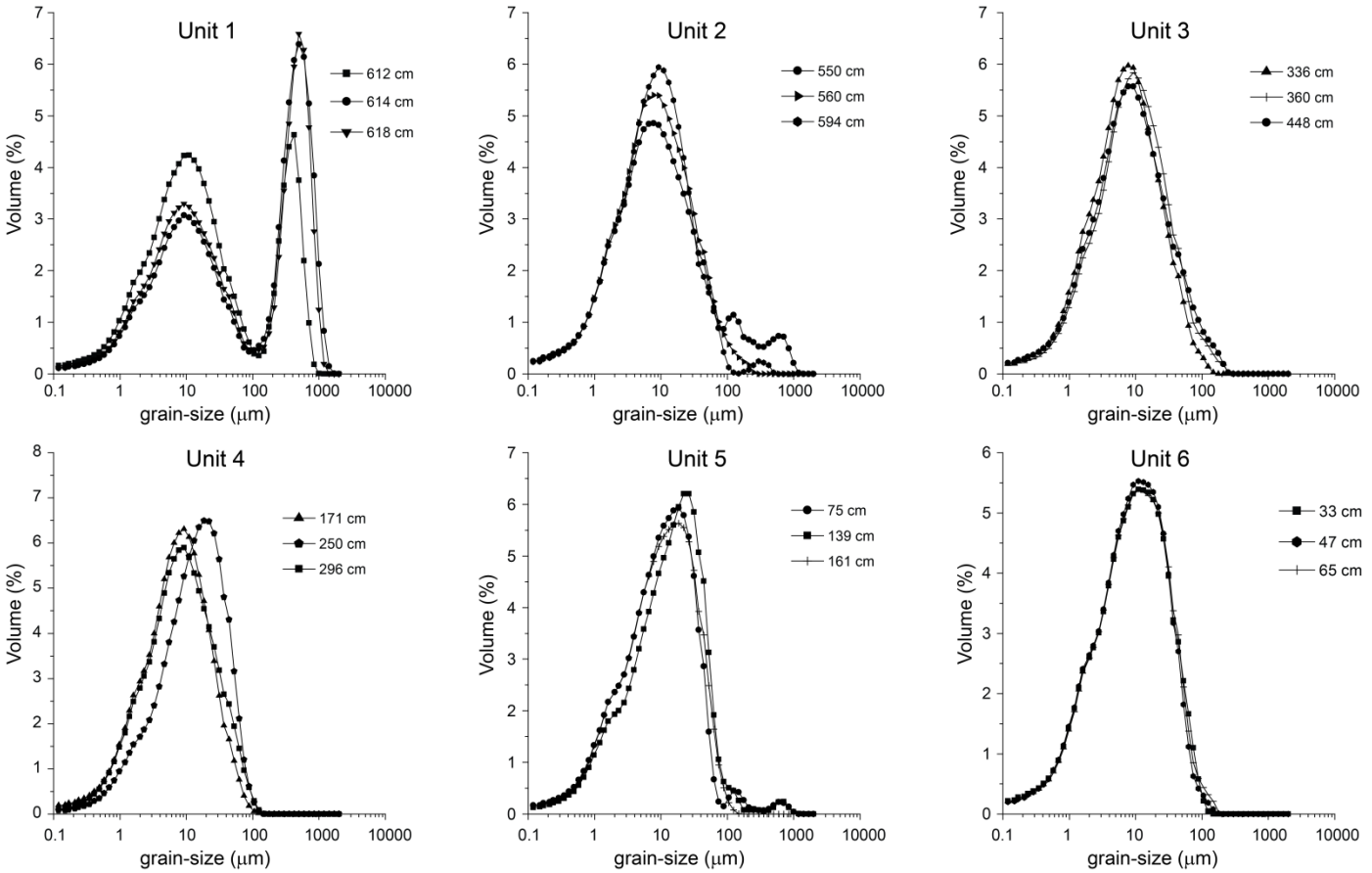

Figure 2.3. Grain-size distributions (GSDs) for each unit. Unit 1 shows bimodal grain-size distributions with modes at 10 and 400 μm. The GSDs in the upper five units show that the deposits generally consist of fine-grained particles dominated by a mode at 8-20 μm. Note that some of the GSDs in units 2 and 5 have irregular tails at grain sizes >100 μm.

Unit 6 (70-30 cm) consists of silty clay sediments and is separated from unit 5 by an 8-cm thick black layer at 70-62 cm (Fig. 2.2a). The median grain-size varies at ~9 μm. The TOM and calcium carbonate content reach up to 18% and 2.5%, respectively (Fig. 2.2d, e). Core density decreases to 0.85 g cm^{-3} (Fig. 2.2f). The black layer was also observed in core WA11. Starting from the bottom of this layer, the magnetic susceptibility increases sharply to the highest recorded value (80 SI units) at the top of this layer, and then it reduces rapidly to about 30 (SI units) (Fig. 2.2g). The geochemical analysis revealed enriched Zn and Pb concentrations in this layer (Fig. S2.8.2).

The organo-clastic interval of core WA16 (units 2-3) was examined to identify clastic flooding layers through a variety of sedimentological criteria that commonly are used in paleoflood hydrology (Benito et al., 2003; Benito and Thorndycraft, 2005): (i) color change; (ii) silt and clay deposits intercalated between organic-rich deposits; (iii) horizontal clay laminations. These flooding layers appear as single layers as well as clustered laminations in the sediments, and the thickness varies between 0.1 and 0.6 cm (Fig. 2.4c-f), The black bars in Figure 2.2b and Figure 2.4c-f show the position of the clastic flooding layers (thickness is not on scale).

2.4.2. Age-depth model

The AMS ^{14}C ages were calibrated to calendar years before present (1950 AD). The calibrated ages in units 2 and 3 do not deviate from a steady increasing age trend with depth (Table 2.1, Fig. 2.2, 2.5), suggesting that the sediment accumulation took place progressively and without reworking in the organo-clastic sequence. The tuned age-depth relation for the clastic sequence is present in Figure 2.5, and the detailed information is provided in the spreadsheet of the supplementary material. Average accumulation rates were derived for units 1-3, and for the overall clastic sequence (Fig. 2.5).

2.4.3. End-member modelling analysis

The median coefficient of determination (r^2) reveals that a four-EM model explains more than 85% of the total variance of the GSDs (Fig. 2.6a). Using a five-EM model or six-EM model does not significantly improve the performance, while a three-EM model performs very poorly ($r^2<0.7$) in the range from 53-220 μm (Fig. 2.6b). Although the median r^2 values of the four-EM model decrease from 0.8 to 0.6 in the grain-size interval 105-200 μm (Fig. 2.6b), reflecting a slightly reduced explanatory power in this range, we consider the four-EM model to be the most suitable mixing model for the WA16 grain-size dataset. Figure 2.6c shows the grain-size distributions of the four EMs, with the finest labelled EM1 and the coarsest labelled EM4. EM1 has a mode at 7 μm. The modes of EM2 and EM3 are 20 μm and 31 μm, respectively. The secondary mode of EM3 at >100 μm (Fig. 2.6c) is associated with the decreased coefficient of determination within that range (Fig. 2.6b). The coarsest EM4 has a dominant mode at 450 μm and a secondary mode at 10 μm.

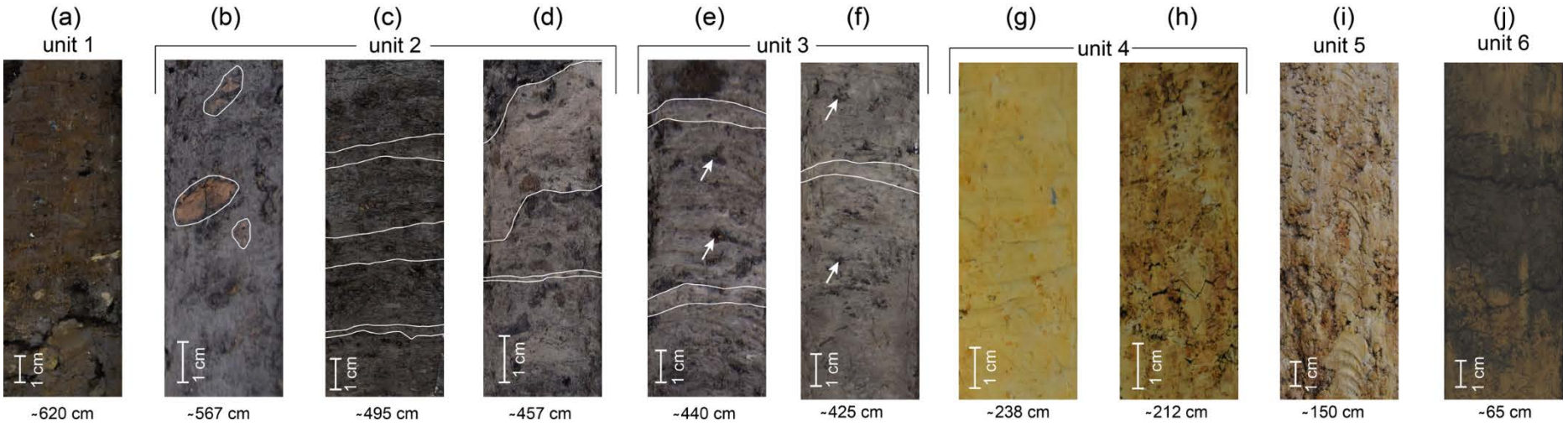

Figure 2.4. Photographs of the units. (a): unit 1 shows a fining-upward trend, the base contains gravels and coarse sands while the top consists of silts; (b)-(d): well-preserved wood pieces, closely-spaced laminae and clastic flood deposits are highlighted with white lines in unit 2; (e) and (f): charcoal spots (white arrows) and flood layers (white lines) in unit 3; (g) and (h): homogeneous yellowish sediments and rusty spots in unit 4; (i): brown clays and silts with rusty spots in unit 5; (j): unit 6 with a black layer containing high concentrations of Zn and Pb.

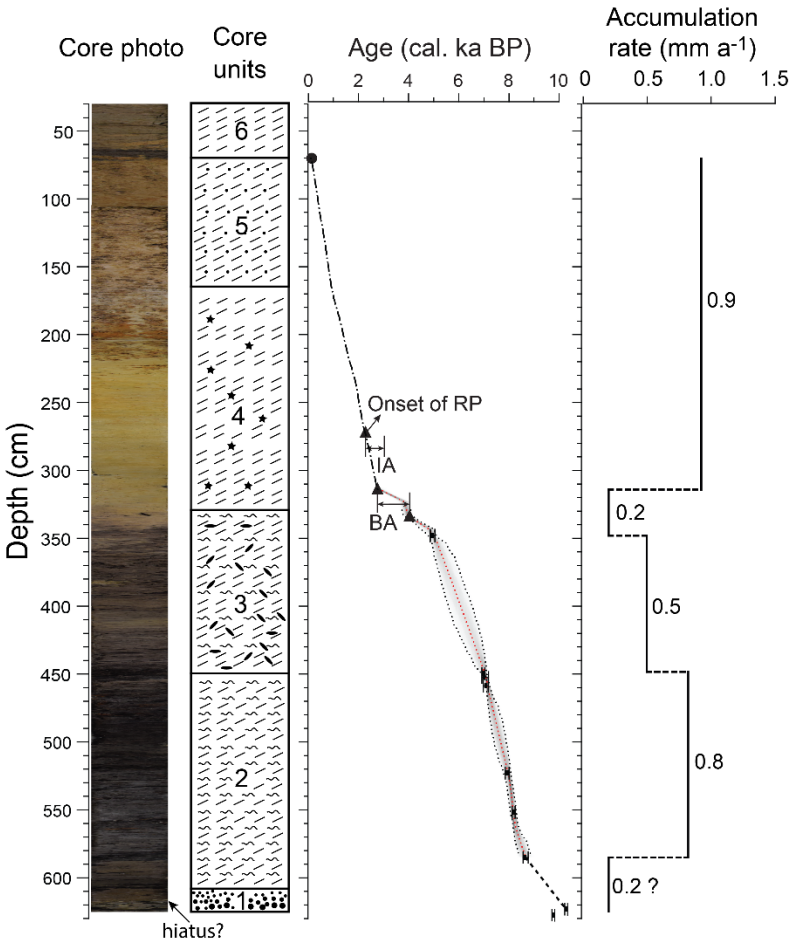

Figure 2.5. Bayesian age-model with 2σ error below 314 cm and tuned age-model (dash-dotted line) above 314 cm. Two calibrated 14C ages in unit 1were excluded due to the uncertainty of erosion (see 2.4.2 and 2.6.1). The triangles which represent time boundaries are derived from archaeological evidence (BA=Bronze Age, IA=Iron Age, RP=Roman Period). The dot at 70 cm reflects peak coal mining activity upstream along the Meuse in the middle of 19th century (Stam, 2002). Average accumulation rates were derived for units 1-3, and for the overall clastic sequence. See lithological explanations for core units 1-6 in Figure 2.2b.

Figure 2.6d denotes the relative contribution of the four EMs in relation to their stratigraphic position. EM1 and EM2 are dominant throughout the core. Their total contribution is about 85% in units 2-6 (Table 2.2). EM1 varies around 50% at 610-270 cm, from 270 to 230 cm its contribution is very low (average of 20%), at 230-165 cm it again reaches to 50%, but from 165 cm its contribution declines again (<38%). The average abundance of EM2 at 610-560 cm is 35%, but it decreases gradually until 470 cm, subsequently, EM2 increases to an average of 43% in unit 3 and unit 4. In the middle of unit 4, EM2 shows a series of spikes (Fig. 2.6d). In unit 5 and unit 6, EM2 accounts for an average of 65%. The average contributions of EM3 in unit 2 and units 5-6 are 24% and 15%, respectively. In units 3-4, the average proportion of EM3 is 8% and varies within a narrow range. EM4 is dominantly present in the core base but almost absent in units 2-6 (Fig. 2.6d).

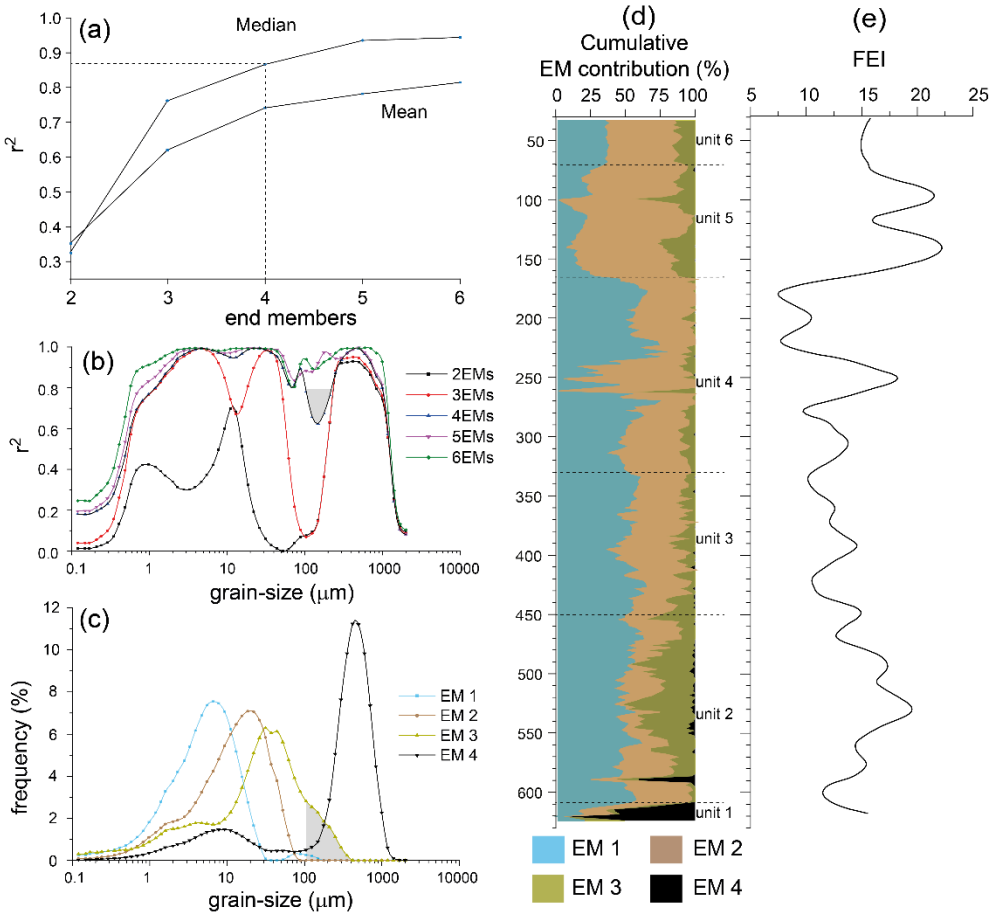

Figure 2.6. The end-member modelling results and the FEI variation against core depth. (a) Median and mean r2 on all grain-size classes as a function of the number of end-members. A four-end-member model is sufficient to explain more than 85% of the total variance; (b) r2 for each size class for end-member models with two to six end-members; (c) The modelled end-members (EMs) according to the four-end-member model (4EMM); (d) Proportional contribution of the EMs of the 4EMM; (e) FEI variation against the core depth based on the 4EMM. Horizontal dashed lines mark the unit boundaries. Shaded areas in (b) and (c) indicate the decreased r2 at grain-size class larger than 100 μm (see 2.4.3).

2.5. A new method for paleoflood reconstruction, the Flood Energy Index (FEI)

To date, linking the coarse fraction of grain-size distributions (e.g., the P90, the percentage of sand fraction, or a coarse EM score) to paleoflood magnitudes is becoming a relatively widely-applied approach in paleohydrological research (e.g., Knox, 2006; Toonen et al., 2015b; Munoz et al., 2018). For several reasons, we consider this method suboptimal. For example, the lack of substantial sand content in a sediment record does not necessarily means that no flood events occurred in the past. Minor floods with a limited inundation area may not pass a uniformly set critical P90 value or minimum EM score, and appear unrecorded in otherwise continuous series. More importantly, if (part of) the grain-size record is 'contaminated', the (problematic) GSDs should be corrected by filtering out the noise. Specifically, in units 2 and 5, the coarse tails of the GSDs (>100 μm) exhibit anomalous shapes (Fig.

2.3). One reason for this could be that this grain-size range holds contaminations from sand-sized Fe-Mn concretions in unit 5 and particulate organic remains that survived from sample pretreatment in unit 2 (e.g., Toonen et al., 2015b). Therefore, we developed a Flood Energy Index that normalizes the raw grain-size parameters by incorporating the flood-sensitive coarse populations and excluding the contaminated grain-size portions. This index highlights the increased floods that occurred within a certain period by quantifying the relative contribution of coarser grains in flood deposits. This means the FEI prepares channel-fill grain-size records for interpretation in terms of flooding phases (cf. Macklin et al., 2005), rather than for single event-magnitude quantifications. What to include and exclude in the coarse grain-class range is dependent on the GSDs, the EM modelling results and laboratory observations.

In this study, we chose the grains-size between 31 and 105 μm as the flood indicator. The upper limit of 105 μm was selected due to its proximity to 100 μm and readily accessible in raw grain-size dataset. The coarse EM3 requires a higher flow energy to be transported than the finer EM2 and therefore can be linked with peak discharge during floods, but the direct use of EM3 is inappropriate due to the 'contaminated' part at its coarse end (Fig. 2.6b-c). The mode of EM2 (20 μm) corresponds with the modes of the bulk GSDs (8-20 μm) in unit 2-6 (Fig. 2.3). The finer EMs (EM1 and EM2) represent suspended and wash load populations, for which it is assumed that limited differentiation occurs between different flood magnitudes, as these fine particles are also in suspension during normal flow. Here, we chose the mode of coarse EM3 as lower boundary to reconstruct FEI as it can better represent the coarse component of floods. Therefore, we define the FEI as:

$$FEI = \left({}^{V_{31-105}}/_{V_{0.12-105}}\right) \times 100$$

Where the $V_{31\text{-}105}$ and $V_{0.12\text{-}105}$ represent the volume fraction with a grain size range of 31-105 μm and 0.12-105 μm, respectively. By doing this, the FEI excludes the grain-size signals in the fraction above 105 μm. The EM4 is not used due to its absence in most part of unit 2-6. FEI variation against core depth is shown in Figure 2.6e. We used a locally weighted polynomial smoothing function to prevent undue emphasis being placed on single data points. In order to assess the reliability of FEI, we conducted a series of statistical analyses comparing the FEI with other paleoflood proxies, including median, mean, 90th percentile (P90) and the mean of sand (>63μm) fraction (MS).

2.6. Discussion

2.6.1. The Holocene floodplain evolution

The Well-Aijen paleochannel contains a fairly complete continuous depositional record of Meuse flood deposits from ~8600 cal a BP up to the beginning of the Common Era (2000 cal BP). This makes the study site very suitable for studying depositional changes and fluvial dynamics in the Lower Meuse catchment, as continuous records are extremely rare in such a dynamic fluvial system (Bos and Zuidhoff, 2015). The reason that the WA record is relative complete, is that organic-rich sequences are very much

stable sedimentary environments that offer the opportunity to derive continuous records that can be precisely dated (Goslin et al., 2018). Our chronology for the organo-clastic part supports this (Fig. 2.5). The distinct GSDs of unit 1 and unit 2 reflect a rapid sedimentary environment change (Fig. 2.4a-b); which implies the channel was abandoned in a short time. The vivianites were observed in the channel bed deposits (unit 1), indicating a reducing environment during or after the deposition. After that, the abandoned WA paleochannel changed into a fluvio-lacustrine environment. At the very base of unit 1 the ^{14}C results produced relatively old basal dates (Table 2.1), and the dates imply a rather low accumulation rate (0.2 mm a^{-1}) for this unit (Fig. 2.5). Also, an exceptionally coarse sand bed (at 615 cm, Fig. 2.2c, 2.5) is interbedded within a relative finer deposition. We suspect this coarse bed was formed during a short-lived flood event and may have caused a hiatus or reworking of sediment. Therefore, we focused our interpretation on the part of the channel-fill above 610 cm which covers the time interval since ~8600 cal BP. This underlines that a risk may exist for ^{14}C dating when using organics buried in active channel bed deposits (Chiverrell et al., 2009; Howard et al., 2009).

The overall fine-grained deposits in core WA16 (Fig. 2.3) reflect that the flood water transporting capacity was limited at the core site. Hence, the well-preserved leaf remains and fresh wood pieces can be considered as originating from local vegetation. Even though the archaeological excavation indicates that humans already appeared at Well-Aijen during the Mesolithic and Neolithic (Bos et al., 2014; Bos and Zuidhoff, 2015), the impact of prehistoric humans on the landscape and river behavior was probably limited (Kalis et al., 2003). This is also evidenced by the high percentage of tree pollen species and low proportion of agricultural pollen species (i.e., *Cerealia*) (supplementary material, Fig. S2.8.5). The moderate sedimentation rate in the organo-clastic part (Fig. 2.5) resulted from the local morphodynamics in a natural depositional setting rather than representing general floodplain accumulation rate (Toonen et al., 2012). From unit 2 to 3, the accumulation rate is nearly halved and the median grain-size shows a minor decrease. This can be attributed to the disconnection from later-formed active river channel and the gradual infilling of the abandoned channel (Toonen et al., 2012). The anti-phase variations of TOM (increasing trend) and core density (decreasing trend) in unit 2 (Fig. 2.2) indicate that the organic matter input was dominant over the clastic material input. This feature is different in unit 3, in which the reduced TOM and elevated core density is indicate of the dominant clastic sediment input. The transition from unit 3 to unit 4 features sediment composition and color change, indicating the transition from abandoned channel into a floodplain that only received sediment input during floods. If this change was caused by a depositional hiatus, we would expect the sharp shifts in the parameters' variation at ~330 cm. However, neither the grain-size from core WA16 nor the pollen data from WA11 show an apparent shift (Fig. S2.8.5, Fig. 2.2c, e-g). Thus, we think this transition reflects a continuous channel infilling rather than a hiatus.

In the Iron Age (unit 4, Fig. 2.5), the significant increase of agricultural pollen indicators (Fig. S2.8.5) indicates that humans exerted profound influence on the landscape since then. At the same time, the

river Meuse began to raise and widen its natural levees, the distal edge of which expanded across the study side (Bos and Zuidhoff, 2015). Although uncertainty exists in the age-depth model, and the sedimentation rate could have fluctuated due to the non-stationarity of the fluvial system (Toonen, 2015), the onset of Iron Age deposition (~2.7 ka BP) at ~314 cm and the polluted black layer at ~70 cm together constrain the overall accumulation rate to 0.9 mm a^{-1} for that interval (Fig. 2.5), which is significantly higher than the accumulation rate in the ^{14}C dated organo-clastic part. Moreover, assuming the existence of a hiatus at ~220 cm (where the lithofacies changed) would give an even higher accumulation rate (>0.9 mm a^{-1}). Prolonged human influence in the catchment (i.e., soil erosion upstream) and floodplain from the Iron Age, Roman Period and Medieval Warm Period (De Moor et al., 2008) is reckoned to account for overall higher sedimentation rates at our site and in the wider floodplain of the lower Meuse (Pierik et al., 2017).

2.6.2. Evaluation of FEI

We suggest two conditions need to be fulfilled in order to use FEI appropriately in paleohydrological contexts. First, the tectonic movements should be minor because it can change the river morphology and the connectivity between sediment trap and river channel. Second, the channel migration should be limited. This is because large-scale migration can produce different index values even when the floods have similar magnitudes. As stated before, the two prerequisites are satisfied in this study. In order to assess the performance of the FEI, results were statistically compared with direct grain-size descriptors (median, mean, P90 and MS), that have been used as proxies in flood magnitude reconstruction (Benedetti, 2003; Arnaud, 2005; Czymzik et al., 2013). Here, three subsets of grain-size data from unit 4, unit 2 and unit 5 were examined (Fig. 2.7). The grain-size composition in unit 4 represents a 'clean' dataset because there are neither concretions nor excess organic matter, which could cause biases in the dataset. Based on the EM modelling results and the sedimentological observations, the datasets from unit 2 and unit 5 were contaminated by concretions and/or organic remains. In these units, we expect that using the direct descriptors is inappropriate and FEI should outperform the other proxies.

In unit 4, the statistical analysis shows that there are good linear relationships ($0.77<r^2<0.97$) between FEI and other proxies (Fig. 2.7a). This means, when using a 'clean' grain-size dataset, all these parameters (FEI, median, mean, P90 and MS) are able to represent the coarse-grained population which link with paleofloods. In contrast, the correlations are poor in organic-rich unit 2 (Fig. 2.7b) with more scattered data points, as the r^2 varies between 0.56 and 0.83. This indicates, either the FEI or the other paleoflood proxies fail(s) to be used as paleoflood indicator(s). This is likely due to the incorporation of organic remains in the grain-size composition (i.e., Toonen et al., 2015b), and our laboratory observations support this. Therefore, we argue that a more reasonable approach in reconstructing past floods is to adopt a reliable grain-size composition rather than incorporating the problematic portion. Certainly, some GSDs may not have been contaminated, but when the problematic GSDs cannot be distinguished from the overall dataset, rejection of the problematic proportion is more logical. This

principle should also be applied to unit 5, in which there are quasi-linear correlations ($0.83<r^2<0.96$) between FEI and other proxies (Fig. 2.7c) regardless of the observed concretions. The correlations plausibly show that all these parameters work well. This is because the post-depositional Fe-Mn concretions were treated as 'real particles' by the laser-diffraction instrument during grain-size analysis. The scanning electron microscope images show that these fragile concretions have irregular shapes with sizes larger than 100 μm (Fig. S2.8.3). To what extent these concretions have affected the grain-size dataset is of great importance in FEI construction. In this case, the reason to exclude the grain-size range larger than 105 μm is that the particle size of the concretions is an order of magnitude larger than the mode of GSDs in unit 2-6 (Fig. 2.3). Thus these concretions have undoubtedly enlarged the values of P90, median, mean and MS. Incorporating the problematic compositions can result in overestimation of the paleoflood magnitudes in paleodischarge reconstructions as the concretions are much coarser than the sediment particles.

The formation of these concretions is associated with soil formation and gley phenomena. As these post-depositional processes are ubiquitous worldwide including in monsoon and equatorial zones, we propose that grain-size datasets should be evaluated before being used in paleoflood reconstructions. The FEI method proposed here provides an approach to remove the effect of the post-depositional processes. Therefore, we think the selective use of grain-size datasets should be considered when the regular laboratory treatment is unable to produce a robust dataset due to the existence of Fe-Mn concretions and residual particulate organics. Based on the above, we think the method of constructing FEI has potential to be popularized when encountering similar challenges elsewhere. By applying this method, the effect of contaminated portions in grain-size datasets can be minimized.

2.6.3. Holocene paleoflooding phases

The FEI variation through the Holocene is given in Figure 2.8. The FEI record starts at 8.6 cal ka BP because of the uncertainty of the basal ^{14}C dates. The higher FEI highlights the flooding phases that are reconstructed in core WA16. The visually determined clastic flooding layers were plotted against the age axis with a scale showing the thickness (Fig. 2.8). We think the closely-spaced thin layers at around 440 cm, 460 cm, 500 cm and 520 cm (Fig. 2.2a) were formed during a series of short flood events. Therefore, these thin layers are integrated as single floods. These observed flooding layers correspond well with the increased flooding phases derived from FEI variation (Fig. 2.8). In the Mesolithic (11.6-6.8 cal ka BP) and Neolithic (6.8-4.0 cal ka BP), five multi-centennial flooding phases occurred; at *c.* 8500, *c.* 8000, *c.* 7600, *c.* 7000 and *c.* 5900 cal a BP. The pollen data (i.e., occurrence of *Cerealia, Anthoceros Punctatus, Rumex and Plantago*) reveal that humans began to alter the landscape by grazing and land reclamation at this stage (Bos and Zuidhoff, 2015). However, human activity in this period is still low and thus unlikely to have exacerbated the magnitude and frequency of floods.

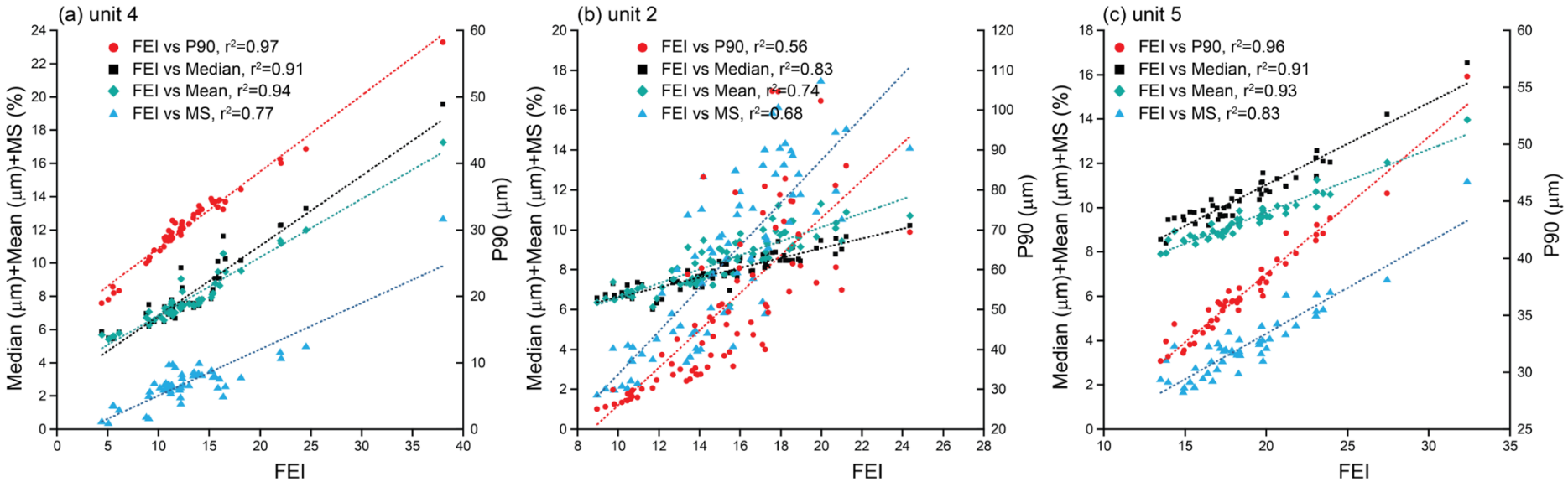

Figure 2.7. Statistical analysis of FEI with other paleoflood proxies: P90= 90th percentile, Median=median grain-size, Mean=mean grain-size, MS = mean of sand fraction. Unit 4 represents sediments with a 'clean' dataset without Fe-Mn concretions and organic matter; while part of the samples from units 2 and 5 contain minor admixtures of organic remains and Fe-Mn concretions, after conventional sample pretreatment, respectively. The results show that there are good linear relationships between FEI and other proxies in units 4 and unit 5, and poor correlations in unit 2.

In the time-period from 5-3 cal ka BP, the FEI is characterized by low values with small fluctuations, indicating the flood activity has been low (Fig. 2.8). Meanwhile, the regional agricultural pollen species also declined (Fig. S2.8.5). This period followed the termination of the Holocene Climatic Optimum (9-5 ka BP) which featured relatively wet and warm climate conditions (Wanner et al., 2008). Intermittent glacial advances have been recorded in the Northern Hemisphere after the Holocene Climatic Optimum (Wanner et al., 2008 and references therein). The dryer and cooler climate phase during the Subboreal (5-2.5 cal ka BP) may have led to a low discharge regime of the Meuse, and suppressed the flooding phases and sedimentation rate. The role of human activity in changing the flooding regime is unclear.

In the late Holocene, the first high flooding phase occurred at *c*. 2800 cal a BP (Fig. 2.8). This period corresponds with the early Iron Age. This phase may have resulted from the 2.8 ka climate anomaly which is characterized by cooler and wetter climate conditions in Europe and North America (Van Geel et al., 1996; 1998). During the Common Era, the FEI index reveals an oscillating flooding magnitude that will have echoed through in an irregular sedimentation rate (Fig. 2.5 and 2.8). Based on the tuned age-model for the late Holocene deposition, the FEI record tentatively reveals that the last three flooding phase occurred at *c*. 2000, *c*. 700 and *c*. 300 cal a BP (Fig. 2.8). The first one coincides with the Roman Period (*c*. 12 BC-250 AD), and this identification agrees with the stratigraphic observation as the FEI values were derived from grain-size information at ~274 cm in core WA16, which corresponds with the onset of early Roman Period deposition (Bos and Zuidhoff, 2015). The latter two phases most likely coincide with the Medieval Warm Period (*c*. 950–1400 AD) and the Little Ice Age (*c*. 1400-1850 AD). During the Dark Ages (*c*. 200-800 AD), flooding is less severe. Previous studies support these interpretations. First, the wet and warm summers that occurred during periods of Roman and medieval prosperity (Büntgen et al., 2011) may have contributed to the intense floods. Second, widespread deforestation and population expansion in the Roman Period and the Medieval Warm Period stimulated soil erosion and further increased the volume of sediment input to the Meuse (Berendsen and Stouthamer, 2000; De Moor et al., 2008; Ward et al., 2008; 2009).

Notably, the FEI is higher with larger amplitude in the late Holocene, indicating the flood intensity is higher in the late Holocene. The more fluctuant flooding regime and high accumulation rate (Fig. 2.5) indicate rather unstable hydroclimatic conditions in the late Holocene. However, to more accurately date and resolve flooding phases for the late Holocene, it would be preferable to sample a paleochannel fill of younger age instead of a middle Holocene channel fill and a late Holocene floodplain overburden. Nevertheless, the FEI index shows considerable potential to resolve the flooding phases both in the subaqueous organic facies as well as in the floodplain deposits, and enables cross-correlations between channel fill and floodplain sites in low land rivers such as the Meuse.

2.7. Conclusion

The Well-Aijen paleochannel contains a record of phasing in paleoflood activity that spans a large part of the Holocene. The lower organo-clastic part of the sequence (unit 2-3) represents a fluvio-lacustrine swamp environment, which formed after the channel abandonment in the early Holocene. Natural depositional processes dominated over the limited human interference. The upper clastic part of the sequence (unit 4-6) formed since the Bronze Age, and was affected by the enhanced human interference which accelerated sediment accumulation rates.

This study indicates that post-depositional Fe-Mn concretions and organic residuals affect the quality of grain-size records, and further influence the EM modelling results and data interpretation in paleohydrological studies. Combining the laboratory observations with the EM modelling results, we argue that the problematic portions of the grain-size distributions should be rejected. By excluding the 'contaminated' portion of the grain-size data, we constructed a Flood Energy Index (FEI) to highlight flooding phases through the Holocene for the Lower Meuse. We think this method is capable of minimizing unwanted signal and has potential to be popularized when encountering similar challenges elsewhere. We suggest the quality of a grain-size dataset should be critically assessed prior to using it for flooding reconstructions.

Multi-centennial periods with increased floods were identified at *c*. 8500, *c*. 8000, *c*. 7600, *c*. 7000 and *c*. 5900 cal a BP within the fluvio-lacustrine part (early-middle Holocene). The low sedimentation rate and low flooding activity in the Subboreal is attributed to a cooler and dryer climate anomaly after the Holocene Climatic Optimum. In the late Holocene, the first flooding phase at c. 2800 cal a BP can be linked to the 2.8 ka climate anomaly. The inferred three last flooding phases occurred at *c*. 2000, *c*. 700 and *c*. 300 cal a BP and coincide with the Roman Period, Medieval Warm Period and Little Ice Age, respectively. Rapid sediment accumulation rates and more severe floods reveal increased fluvial instability in the late Holocene, and also indicate that human exerted a profound influence on fluvial dynamics.

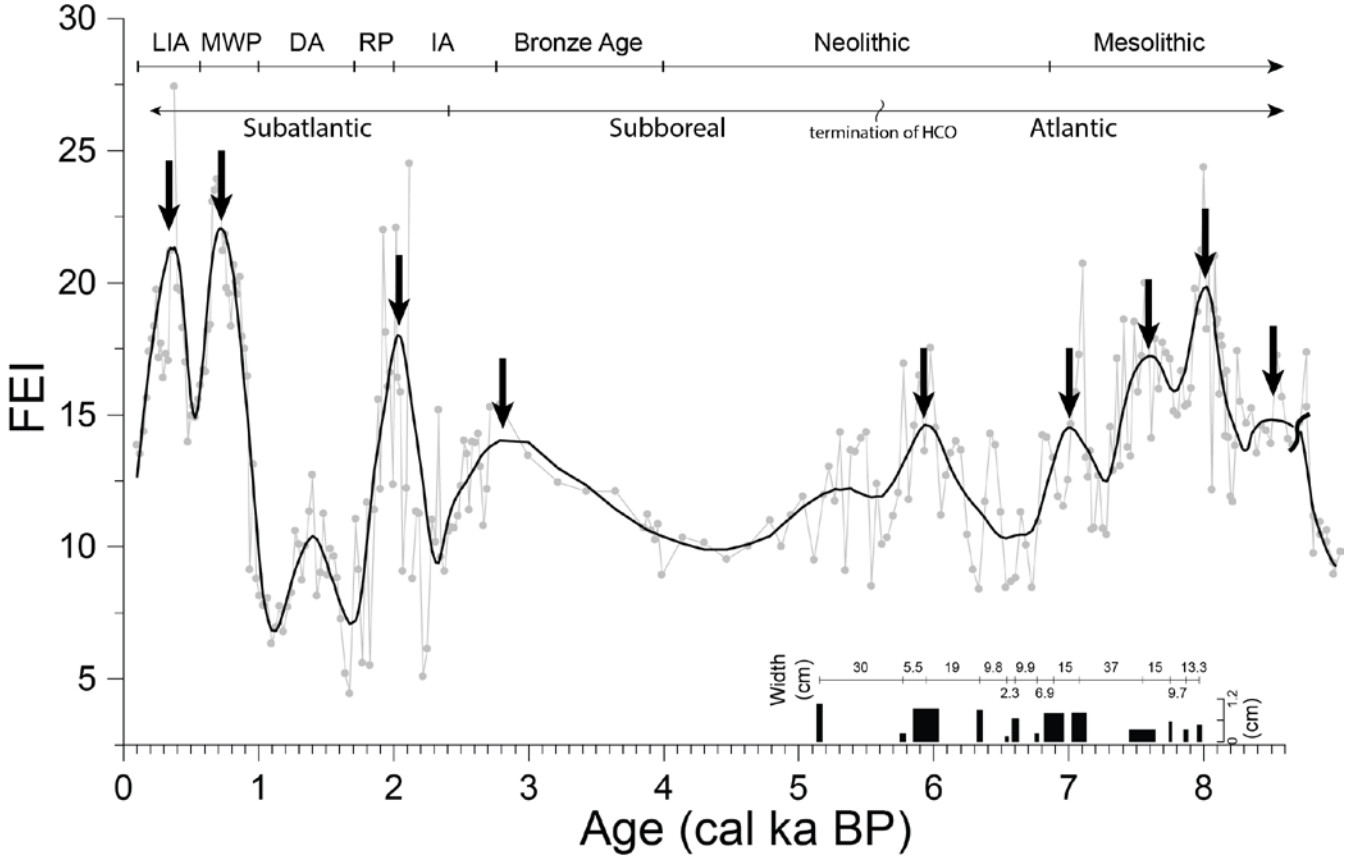

Figure 2.8. The FEI variation through the Holocene. Grey line and dots are raw data; thick black line represents the smoothed curve to prevent undue emphasis being placed on single data points. Arrows above the curve indicate the increased flooding phases according to our sediment analyses. Bars along the age axis represent the thickness of visually determined fine-clastic flood laminae in core WA16. The FEI record starts at 8.6 cal ka BP due to the uncertain ages at the base of core WA16. The top part of the figure indicates the cultural and climatic periods: IA= Iron Age, RP= Roman Period, DA=Dark Ages, MWP= Medieval Warm Period, LIA= Little Ice Age, HCO= Holocene Climate Optimum.

2.8. Supplementary

2.8.1. Correlation of cores WA11 and WA16

Cores WA11 and WA16 were retrieved from the same abandoned channel (WA paleochannel), and the orientation of them parallels to the present Meuse channel (Fig. 2.1b). The distance between two cores is 14 m. For their correlation, we first checked them visually for marker horizons and their boundaries. According to the observations of the inferred sedimentary facies, color change and sediment composition (clastic-rich or organic-rich), we chose the readily recognized layers (millimeter scale) from the two cores as the marker horizons, because these layers represent either the same instantaneous events or very short same episodes of the deposition.

It should be noted that these marker horizons differ from the boundaries of lithofacies units distinguished in the main text (2.4.1). Here, the selection of the marker horizons is mainly based on the color and phase changes. For instance, the boundary between sands and the organic sequence, the interbedded clastic layers within organic sequence, and the representative black mining layer in the upper part. The positions of these marker horizons are shown in Figure S2.8.1 by black arrows. As a second step, we projected the photograph of the two cores and the marker horizons on the coordinate (Fig. S2.8.1). The correlation of these horizons between the two cores enables to compute a linear fitting curve with a very high r^2 (0.9998). It is concluded that the sedimentary lithofacies in the two cores, that are 14 meters apart in space, is essentially the same.

2.8.2. X-ray fluorescence (XRF) analysis

In the two cores, an 8-cm thick black layer between 62 and 70 cm features high magnetic susceptibility. We surmise this layer is related with the mining activity in the middle of the 19th century (Stam, 2002). Five samples were obtained from the black layer and deposits above and below for XRF analysis to determine the trace elements. The results show that the Pb, Cr, Cu and Zn concentration reach the highest level in the black layer and 2-6 times higher than in the upper and lower sediments (Fig. S2.8.2). The lead and zinc mining during the 19th century in the Limburg province (upstream of the Well-Aijen area) should account for the significant increase of these heavy metals.

2.8.3. Analyses of Fe-Mn concretions and grain-size tests

Three to four concretion granules were collected from samples at 54 cm, 89 cm, 131 cm, 153 cm, 177 cm and 208 cm. The pretreatment method is adopted from Konert and Vandenberghe (1997). After picking the concretion granules from the suspensions, they were dried in the stove (60℃) overnight. Under the scanning electron microscope, the concretions have irregular shapes and cellular structure (Fig. S2.8.3). The major oxides consist of SiO_2, Al_2O_3, FeO and MgO and together they account for more than 85%, and the other oxides account for about 15% (Fig. S2.8.3). The concretions from the same and from different depths can have different chemical compositions. For example, MnO appeared

at 131 and 153 cm but is absent in the other four samples. The concretions have strongly different proportion of SiO_2, FeO and Al_2O_3 from 54 and 208 cm depth.

For grain-size reproducibility evaluation, we selected samples from 89 cm, 167 cm, 208 cm, 300 cm, 370 cm and 406 cm. The former three samples contain undissolved concretions, and last two samples have much organic matter. The sample from 300 cm has neither concretions nor organic-rich sediments. Every sample was processed with different methods (a to i, Table S2.8.1), each consisting of different steps. H_2O_2 and HCl are to break down organics and to dissolve carbonates, respectively. $Na_4P_2O_7.10H_2O$ acts as dispersant in grain-size analysis, and the $Na_2S_2O_4$ is used as reducing agent to remove ferric iron.

For samples that contain concretions, methods other than f and g produced grain-size distributions (GSDs) that overlapped well. The GSDs of the sample from 300 cm have the best reproducibility under different methods, which indicates that these methods produced the same results. These observations show that the concretions may have contaminated the GSDs, especially in the coarser part. For the organic-rich samples, all the methods produced good correlations for the GSDs in the finer part (<100 μm), while at grain-size larger than >100 μm, the GSDs show an irregular tail (also see 2.4.4 and Fig. 2.3 in main text).

2.8.4. Tuned age-depth model for the clastic sequence

In the clastic interval of 314-70 cm, we substitute the LOI with FEI index (see 2.4.4 in main text). For larger FEI value (coarser sedimentation), accelerated sedimentation rates are expected than for smaller FEI value (finer sedimentation) in clastic series. Base and top boundaries for the model are derived from the archeological study (Bos and Zuidhoff, 2015) and geochemistry analysis (this study), which constrained the onset of the Iron Age (*c*. 2750 yr BP) at 314 m and *c*. 100 yr BP at 70 cm. The deposits at 274 cm depth (corresponding with the early Roman Period, 2000 yr BP) was used for model calibration. The model uses the following equations (after Minderhoud et al., 2016):

$$\Delta t_i = \frac{D_i}{FEI_i^x} \times \frac{T_N}{\sum_{j=1}^{N} \frac{D_j}{FEI_j^x}} \qquad (2.1)$$

$$Age_i = Age_{j=1} + \sum_{j=1}^{i} \Delta t_j \qquad (2.2)$$

where *i* and *j* identify individual sampled layers, D is the thickness (cm) of each sample. *N* is the total number of samples in the interval to which the model applies. T_N is the time duration covered by the interval (in years) and Age_i is the age of sample layer, with *i=j=1* for the lower most layer. Exponent *x* allows for great contrast (and calibration sensitivity) between fast (high FEI) and slow (low FEI) accumulation rate. The exponent was determined by regression, minimizing the deviation between the

ages for the deposit at 274 cm derived by applying Eq. (2.2) and the one derived by its archeology. The tuned age-depth model is presented in the spreadsheet of the Supplementary material.

2.8.5. Pollen assemblage and cultural periods subdivision

In the Lower Meuse valley and wider surroundings, it is established practice to use presence of agricultural pollen species (*Cerealia, Anthoceros Punctatus, Rumex and Plantago*) and archeological artefacts to infer the prehistoric human activity and (pre)historic vegetation developments in landscape archeological studies and such (e.g., Hoek et al., 2017). These methods have also been applied to the Well-Aijen area specifically. The lower part of core WA11 was used for palynological study by Bos and Zuidhoff (2015) focusing on the vegetation development during the Mesolithic and Neolithic. That study also provided some palynological information on the upper part of the core (Bronze Age, Iron Age and the early Roman Period). Above that level, the material was unsuitable for pollen analysis (too oxidized).

Here, we summarize the pollen diagram in accordance with the cultural periods listed at the right side of Figure S2.8.5. As cores WA11 and WA16 registered the same sedimentary facies (Section 2.8.1 of this supplementary material) and produced the same ^{14}C dating results (Table 2.1 in main text), the information derived from the pollen assemblage can be integrated in core WA16 (Table S2.8.2). The pollen diagram and the summary are based on the work by Bos and Zuidhoff (2015).

Zone 1 (-588 cm). Boreal pollen zone, matching the Middle Mesolithic in the Lower Meuse valley. The pollen assemblage is dominated by thermophilic tree species like *Corylus avellane* and *Quercus robur*, implying a relative cold early Holocene climate in transition to a warm middle Holocene.

Zone 2a (588-422 cm) & 2b (422-353 cm). These two zones span the Atlantic pollen zone, which matches the Middle-Late Mesolithic and the Early-Middle Neolithic in the Lower Meuse valley. The two zones are derived from the high level of tree species (*Quercus robur*, *Corylus avellane*, *Tilia cordata* and *Ulmus glabra*). The lower part of zone 2a has relatively higher percentages of *Pinus sylvestris*, and dates back to the early Atlantic, which corresponds to the Middle Mesolithic. Tree species (*Quercus robur*, *Corylus avellane*, *Tilia cordata* and *Ulmus glabra*) account for more than 97%. The content of *Corylus avellane* declines steadily through zone 2a but rises during zone 2b. *Ulmus glabra* and *Tilia cordata* species reach to high values. The presence of *Hedera helix* and *Viscum album* species indicates warm climate condition (Fig. S2.8.5). In the local pollen diagram (not shown), the abundance of species like *Ranunculus aquatilis*, *Spirogyra*, *and Lemna,* etc., that live in open water, gradually declines from 2a to 2b, indicating the shallowing of an open water environment due to the gradual infilling. The pollen assemblage in zone 2b differs from 2a by, (a) the first human activity in zone 2b, as indicated by agricultural indicators (*Cerealia, Anthoceros Punctatus, Rumex and Plantago*) (Fig. S2.8.5) and increased charcoal spots (Fig. 2.4e, f); (b) the increase of herb pollen species and decline of tree pollen species.

Zone 3a (353-334 cm) & 3b (334-314 cm). These two zones include the Late Neolithic and the Bronze Age. The decline of *Ulmus glabra* indicates the Atlantic to Subboreal transition, which is regionally characteristic in the Meuse valley (Bunnik, 2005a; Zuidhoff and Bos, 2011a, b). Meanwhile, the first appearance of *Fagus sylvatica* in 3b points out that this interval corresponds to the Bronze Age (Bunnik, 2005a, b). The tree pollen has a slight increase and is dominated by *Quercus robur* and *Corylus avellane*, while the agricultural indicator species decline. The climate in this period is generally colder and dryer, possibly reflected by the increase of *Pinus sylvestris* pollen (Fig. S2.8.5). Note that this zone is a relative condensed interval in core WA11 and WA16 alike (main text).

Zone 4a (314-274 cm) & 4b (274 cm-). These two zones are regarded to reflect the Iron Age (four samples in WA11) and the early Roman Period (two samples in WA11; Bos and Zuidhoff, 2015). The subdominant abundance of *Quercus robur* and *Corylus avellane* accompanied by higher levels of grains, grasses, heather and beech in zone 4a (Fig. S2.8.5) indicate this part belongs to the early Subatlantic, which corresponds to the Iron Age. Zone 4b is distinguished from 4a by the appearance of *Carpinus betulus*, the increase of *Fagus sylvatica*, *Calluna vulgaris* and *Cerealia* and increase of tree pollen species.

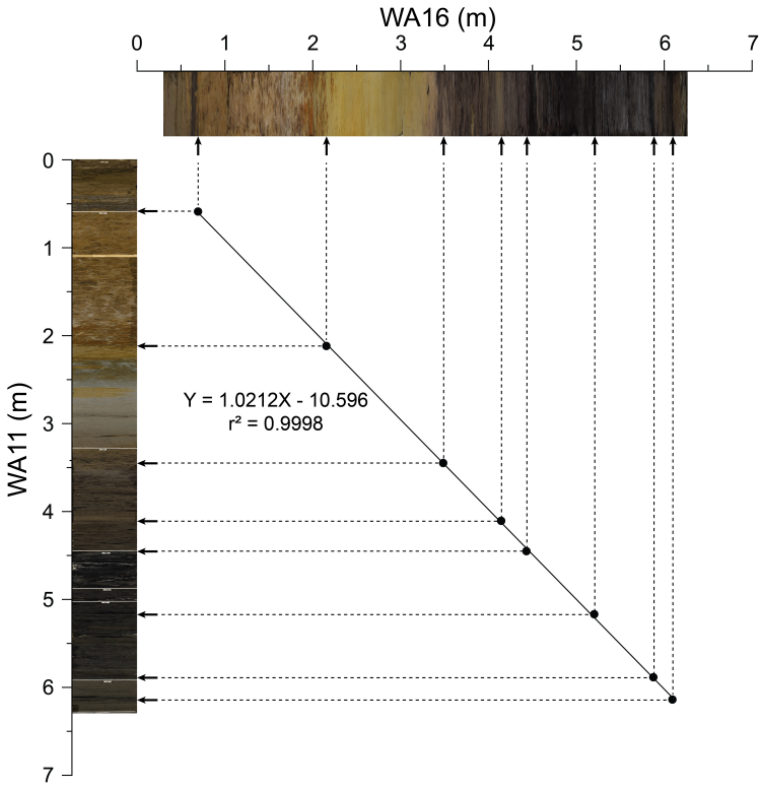

Figure S2.8.1. Correlation of cores WA11 and WA16. Arrows indicate the position of the selected marker horizons. These marker horizons were projected on the coordinate as shown by the black dots.

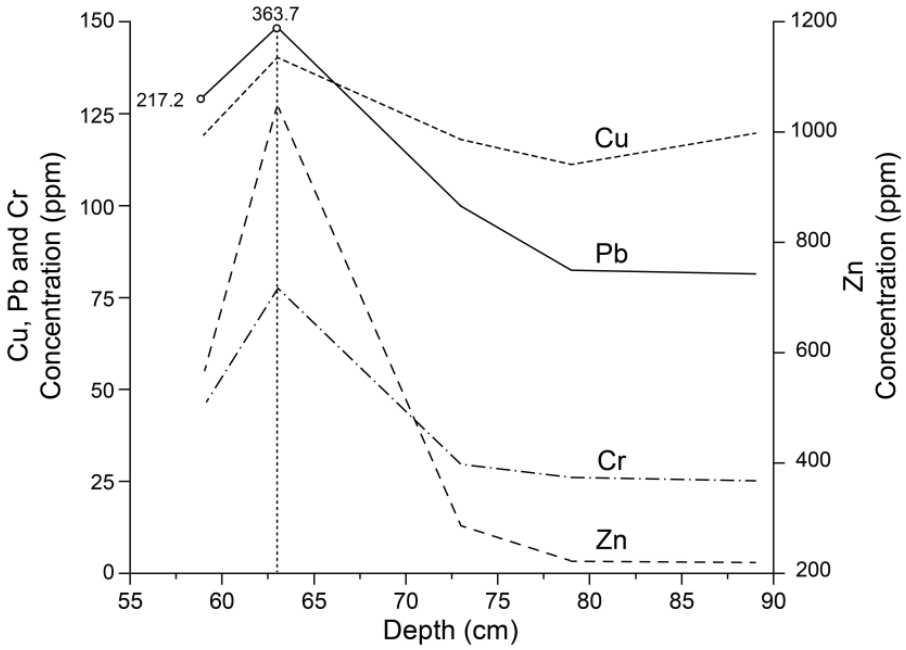

Figure S2.8.2. XRF analysis of the sediments from the black layer (between 62 and 70 cm) shows that the concentrations of heavy metals (Pb, Cr, Cu and Zn) reach peak values within the black layer (vertical dashed line) and decrease rapidly above and below this layer.

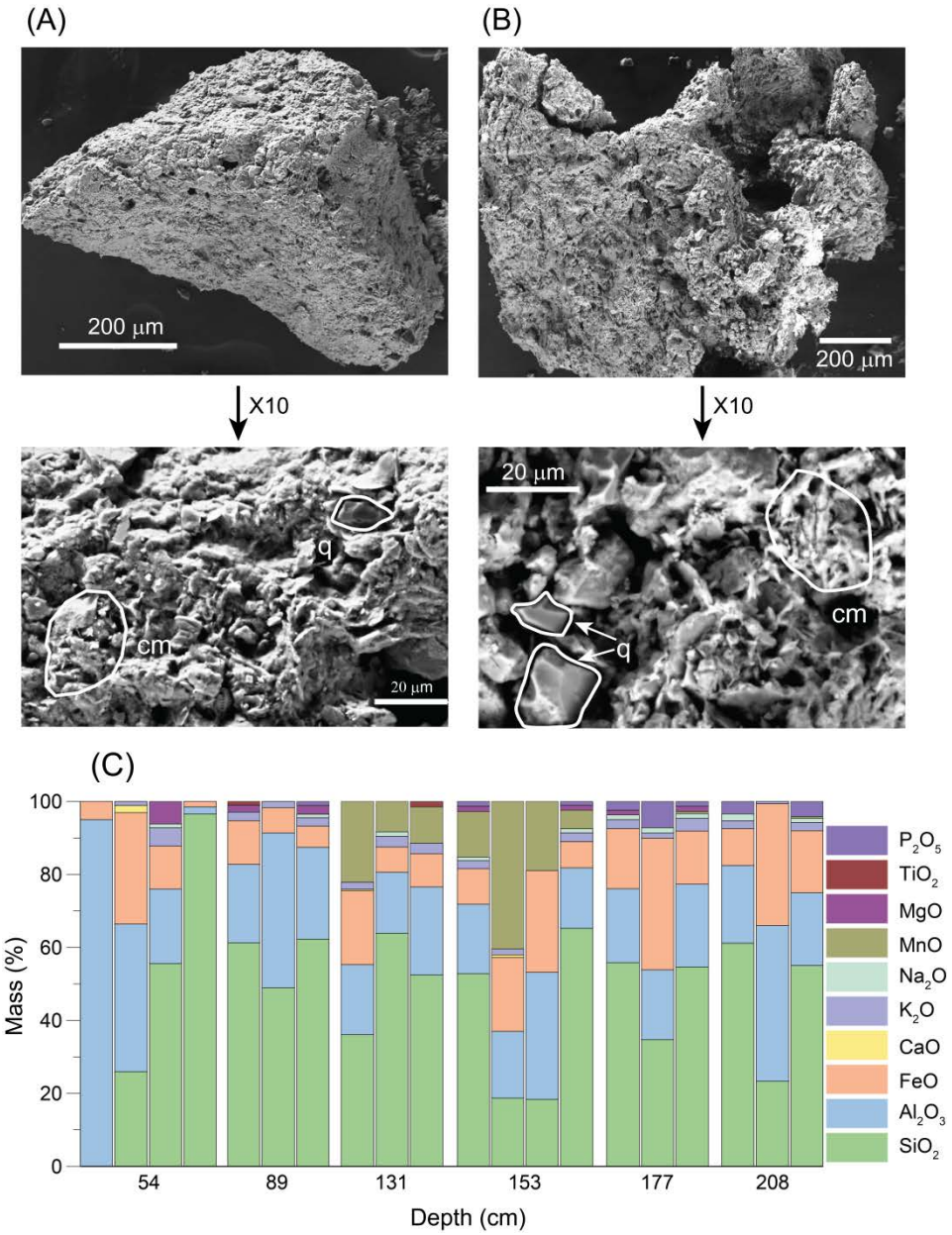

Figure S2.8.3. A, B) Scanning electron microscope images of the concretions, composed mainly of quartz grains and cements (q: quartz, cm: cements); C) the relative content of oxides for each sample.

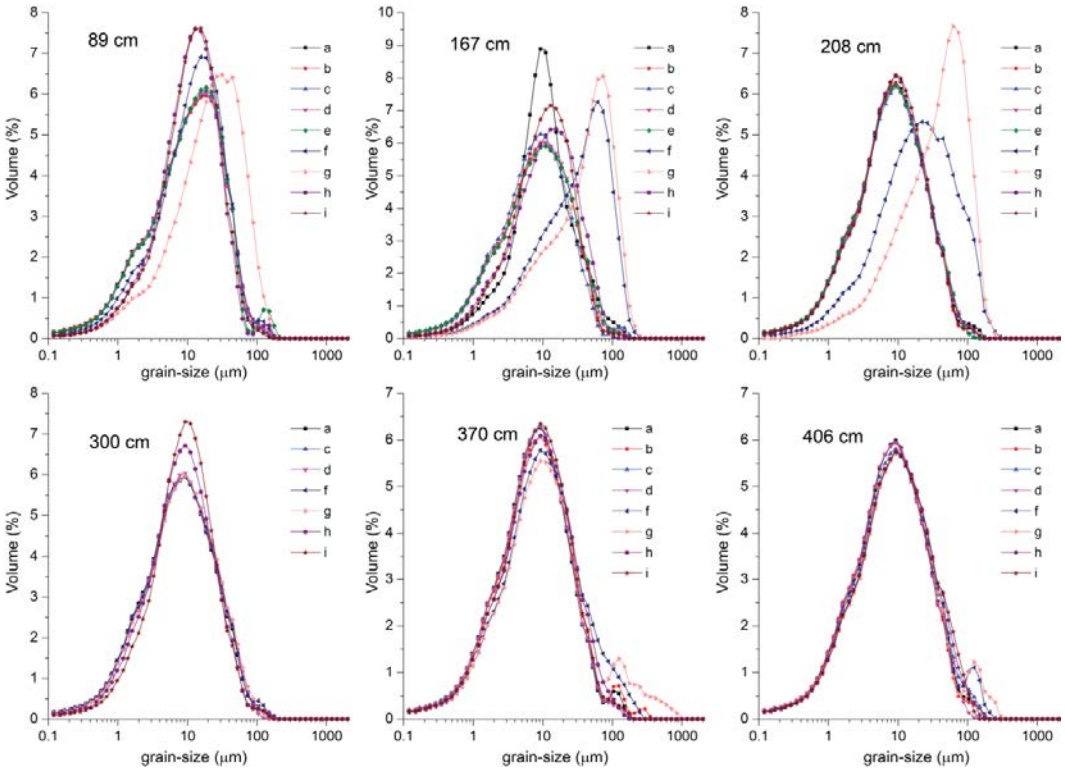

Figure S2.8.4. Grain-size distributions produced from six samples by using different pretreatment methods, a to i. The curve derived from method a reflects standard sample pretreatment and is compared with results based on the other pretreatments, b to i. The samples at 89 cm, 167 cm and 208 cm contain Fe-Mn concretions. The sample at 300 cm does not have Fe-Mn concretions and organic matter, thus methods b and e were not applied. The samples at 370 cm and 406 cm were obtained from the lower organo-clastic part of core WA16, and these two samples do not contain Fe-Mn concretions thus we did not apply method e.

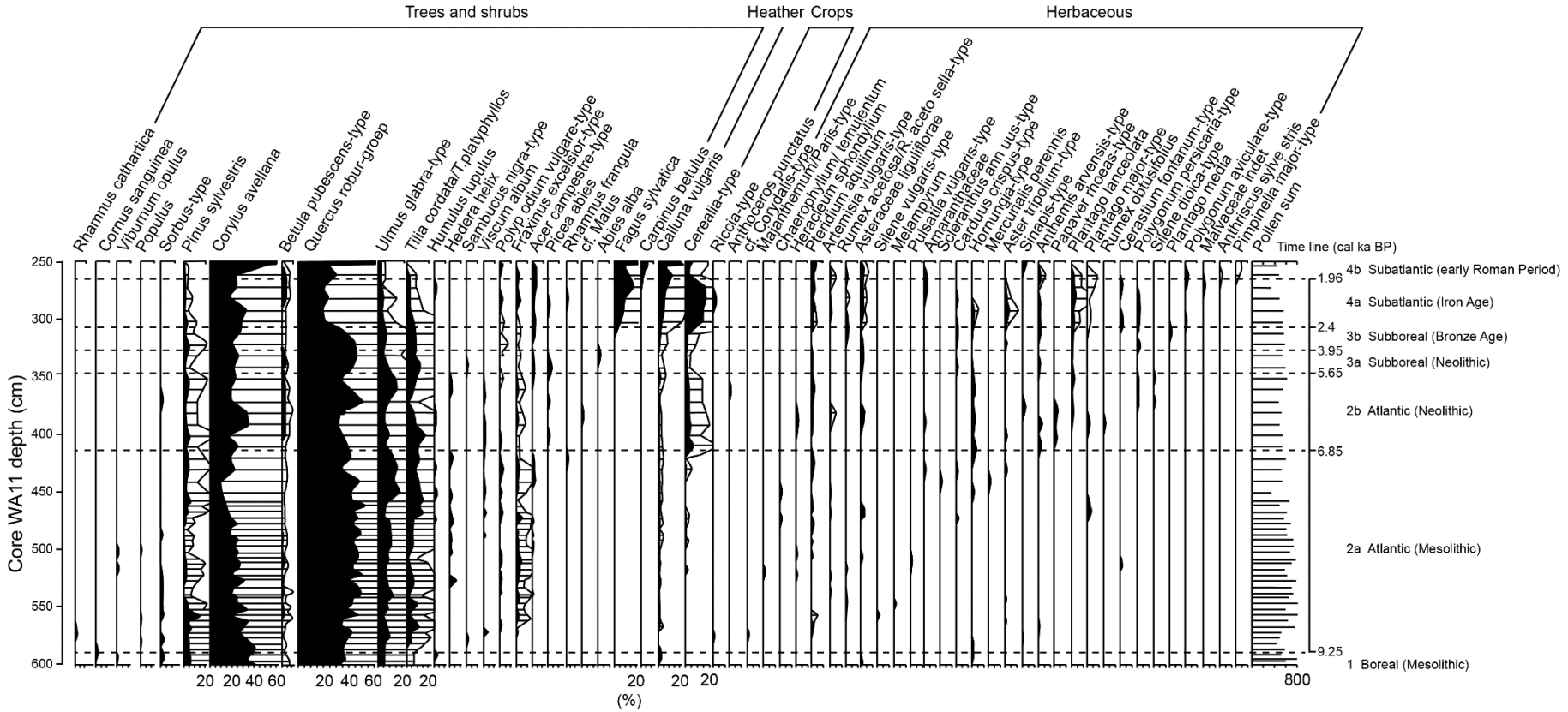

Figure S2.8.5. Regional pollen diagram of core WA11 (after Bos and Zuidhoff, 2015). Cultural and climatic periods are plotted at the right side. Dashed lines show the boundaries of the pollen zones.

Table S2.8.1. Consecutive steps in the different pre-treatment methods

Methods	Reagent and dosage
a	10 ml of 30% H_2O_2, 5 ml of 10% HCl, 300mg $Na_4P_2O_7.10H_2O$
b	10 ml of 30% H_2O_2, 5 ml of 10% HCl, 300mg $Na_4P_2O_7.10H_2O$, 3 minutes ultrasonic homogenizer
c	10 ml of 30% H_2O_2, 5 ml of 10% HCl, 300mg $Na_4P_2O_7.10H_2O$, 300mg $Na_2S_2O_4$
d	10 ml of 30% H_2O_2, 5 ml of 10% HCl, 300mg $Na_4P_2O_7.10H_2O$, 300mg $Na_2S_2O_4$, 3 minutes ultrasonic homogenizer
e	10 ml of 30% H_2O_2, 5 ml of 10% HCl, 300mg $Na_4P_2O_7.10H_2O$, physical disruption
f	20 ml of 10% HCl, 10 ml of 30% H_2O_2, 5 ml of 10% HCl, 300mg $Na_4P_2O_7.10H_2O$
g	20 ml of 10% HCl, 10 ml of 30% H_2O_2, 5 ml of 10% HCl, 300mg $Na_4P_2O_7.10H_2O$, 300mg $Na_2S_2O_4$
h	20 ml of 10% HCl, 10 ml of 30% H_2O_2, 5 ml of 10% HCl, 300mg $Na_4P_2O_7.10H_2O$, 3 minutes ultrasonic homogenizer
i	20 ml of 10% HCl, 10 ml of 30% H_2O_2, 5 ml of 10% HCl, 300mg $Na_4P_2O_7.10H_2O$, 300mg $Na_2S_2O_4$, 3 minutes ultrasonic homogenizer

Table S2.8.2. The bottom depth of each pollen zone and inferred cultural period based on core WA11 (summarized from Bos and Zuidhoff (2015)), the calculation of projected depth in core WA16 is based on the cores correlation (Section 2.8.1 of this supplementary material). Note the bottom boundary of pollen zone 1 is not given.

Pollen zone	Cultural periods	Bottom depth in WA11 (cm)	Projected bottom depth in WA16 (cm)
4b	early Roman Period	270	274
4a	Iron Age	310	314
3b	Bronze Age	330	334
3a	Neolithic	350	353
2b		420	422
2a	Mesolithic	590	588
1			

3. Paleoflooding reconstruction from Holocene levee deposits in the Lower Meuse valley, the Netherlands

Published as: Fei Peng, Cornelis Kasse, Maarten A. Prins, Reinier Ellenkamp, Maxim Krasnoperov, Ronald T. van Balen (2020). Geomorphology 352, 107002

Abstract

This study investigates the Holocene levee deposits and paleoflooding history of the Lower Meuse in the Netherlands based on archeological investigations and sedimentary analyses (grain size, end-member modelling, magnetic susceptibility and thermogravimetric analyses). The levee on the left bank in the study area near Ooijen contains a continuous sedimentary record in the NW downstream part. The archeological evidence and sedimentary results, including a grain size based flood energy index (LFEI), indicate that the Lower Meuse experienced a quiescent flooding period and low sedimentation rates during the mid-late Mesolithic when the levee was low and human influence was minor. Deposition during the Mesolithic shows a fining-upward trend and a highly-developed soil containing abundant artefacts. During the Neolithic and Bronze Age, the flooding intensity was low but gradually increased to a moderate level probably because of deforestation and increased runoff. Limited Bronze Age findings may reflect decreased human activity because of the increased flooding. Starting from the Iron Age, the Meuse experienced a generally enhanced flooding regime, which is reflected by erosion and coarsened sedimentation in the Iron Age and Roman Period. The high peak discharges during the Iron Age may have re-opened a low-lying paleochannel near to the levee during the intensified floods. This general increasing trend is interrupted by the lower flooding phase in the early Middle Ages (Dark Ages). From the middle to the late Middle Ages, the floods intensified again. The coarsening deposition and higher sedimentation rates since the Iron Age resulted from increased floods and higher sediment supply by deforestation and soil erosion. The findings of this study agree with a recent paleoflood reconstruction for the Lower Meuse by using a floodplain archive, implying that levee sediment records have potential in paleohydrological studies if the completeness of the record and chronological information is guaranteed.

3.1. Introduction

Floodplain sediments are used to study river evolution because they contain information on past flooding regimes, landscape change and human activity (cf. Knox, 2006; Benito et al., 2008; Notebaert and Verstraeten, 2010). Floodplain sediments provide good archives for paleo-hydrological studies, because of their availability, accessibility and completeness (e.g. Kochel and Baker, 1982; Yang et al., 2000; Toonen et al., 2015a; Toonen et al., 2017). Wide floodplains, in particular, provide excellent records because they have sufficient space to deposit flooding sediments. Apart from sedimentary archives on floodplains, the reconstructed behavior of river channels may also provide important

information on discharge changes. Examples include fluvial planform changes, longitudinal gradient changes, and vertical elevation changes (incision versus aggradation) (Phillips, 2010).

Levees, the connector between the channel and floodplain, however, have obtained relatively less attention in paleoflooding studies. This is because of the more limited sediment preservation potential on levees (Allen, 1965; Brierley et al., 1997), as the sediments on levees can be easily eroded by later channel migration, floods and human-induced river regulation. Also, the small size of levees relative to the wide floodplain may lead to levees being easily disregarded. Finally, levee sediments consist of clastic materials with little organic matter, which hampers AMS ^{14}C dating and often produces unreliable OSL dating results because of insufficient exposure prior to burial (Duller, 2004; Brook et al., 2006; Fuchs and Owen, 2008; Cunningham and Wallinga, 2012; Zhao et al., 2018). Consequently, levee sediments are commonly not used in paleohydrological studies.

However, like floodplain sedimentary archives (e.g. Toonen et al., 2015a; Peng et al., 2019), the alternating coarser and finer levee sediments can in principle be used to infer flooding regime changes, if other factors (i.e., tectonic movements, channel migration and incision) can be ruled out or constrained by additional data. The relative contributions of finer and coarser deposits can be determined by performing end-member modelling analysis on grain size distributions in vertical sections (e.g. Toonen et al., 2015a; Peng et al., 2019). End-member modelling analysis has been successfully applied to the various sedimentary systems, including floodplain deposits, to understand their source, transport mechanism and depositional environment (i.e., Weltje and Prins, 2003; Prins et al., 2007; Toonen, 2015; Peng et al., 2019). These studies indicate that the end-member modelling approach is capable of distinguishing the different contributing components that reflect the corresponding depositional processes. In fluvial environments (floodplains and levees), a large proportion of coarse end members reflects high discharges, whereas large amounts of fine end members can be associated with low floods, and sometimes with intense soil formation (as a result of strongly reduced sedimentation rates). In addition, long-term human occupation of a levee may also reflect a phase of lower flooding magnitudes, and therefore such archeological information can be combined with inferences from the sedimentary grain size record.

By far, most detailed sedimentological and geomorphological studies on levees have been conducted in the North American river basins (e.g., the Mississippi River in the USA, the Saskatchewan and Columbia rivers in Canada) and the Tuross River in Australia (Fisk, 1944, 1947; Wolman and Leopold, 1957; Farrell, 1987; Smith et al., 1989; Ferguson and Brierley, 2002). According to Brierley et al. (1997), levees have the following four characteristics: (i) they are proximal to channel margins; (ii) they have a triangular cross section; (iii) they are ribbon-like, elongated, and aligned parallel to the channel; (iv) their highest elevation is at or close to the edge of the channel, and the elevation slopes away toward floodplain. However, these key geomorphological and sedimentary attributes of fluvial levees show remarkable variability even within the same river system. For instance, in the Lower Meuse valley in

the Netherlands, the development of the levees depends on the tectonic setting. Levees are well developed and can easily be distinguished on the uplifting Peel Block and subsiding Venlo Block (Fig. 3.1A) because of limited lateral channel migration during the Holocene (Kasse et al., 1995). Therefore, long-term vertical aggradation could occur on the levees. However, in the subsiding Roer Valley Graben (Fig. 3.1A), located farther upstream, the levees are generally lower because of the high rates of lateral channel migration that have eroded pre-existing levee sediments.

In this study we analyze the sedimentological and archeological record of a well-developed Holocene levee, located along the Lower Meuse River, on the Venlo Block. Three vertical sections, located in a man-made trench perpendicular to the levee, were continuously sampled and analyzed. We integrate the chronological framework offered by archeological surveys with the sedimentary analyses (grain size, end-member modeling, magnetic susceptibility and TGA analyses). The main objectives of this study are to discuss the feasibility of levee sediments for paleoflood reconstructions, to determine the flooding regime during each cultural period since the late Mesolithic, and to compare the flooding results of this study to those obtained previously in a floodplain setting about 9 km downstream (Peng et al., 2019).

3.2. Research area

The Meuse originates in northeastern France, flows through the uplifting Ardennes and subsiding Roer Valley rift system, and finally debouches into the North Sea. It has a length of 900 km and a catchment area of 33,000 km2. As a rain-fed river, the annual average discharge of the Lower Meuse is about 230 m3/s. In the Roer Valley rift system, the Meuse passes through the subsiding Roer Valley Graben, and the uplifting Peel Block and subsiding Venlo Block (Fig. 3.1A; Van Balen et al., 2005) before turning to the west in the Rhine-Meuse delta and finally flowing into the North Sea. The study area is located along the Lower Meuse near Ooijen in southeastern Netherlands, and lies on the Venlo Block, in the transition area from a narrow floodplain setting (uplifting Peel Block) to a wider floodplain setting (relatively subsiding Venlo Block; Fig. 3.1A). Bounded by the Late Pleniglacial terraces in the west and Younger Dryas dunes in the east, the landforms in-between are mainly comprised of river terraces and floodplains that formed in the Late Glacial (Bølling, Allerød and Younger Dryas) and Holocene (Kasse et al., 1995).

During the transition from the Late Glacial to the Holocene, the Meuse changed from a braided river with higher peak discharges to a meandering river system with lower peak discharges in response to climate amelioration (Kasse et al., 1995; Huisink, 1999; Tebbens et al., 1999). This river morphological transition resulted in channel abandonment. The abandoned and buried braid channels can be identified on the LIDAR imagery and are referred to as (Ooijen Abandoned Channels) OAC-1 and OAC-2 (Fig. 3.1C) in this study. At the start of the Holocene the Meuse changed to a low-sinuosity meandering river. The river has experienced very little lateral migration in the course of the Holocene and hence high levees have formed in this area (Kasse et al., 1995). The investigated part of the levee is located next to

the present-day Meuse, on the NW part of the point-bar near Ooijen (Fig. 3.1C). The elevation of the present river channel is 10.7 m (+NAP), and the highest part of the levee reaches to 15.5 m (+NAP) in the SE and decreases to 14.6 m (+NAP) in the NW (Fig. 3.1D).

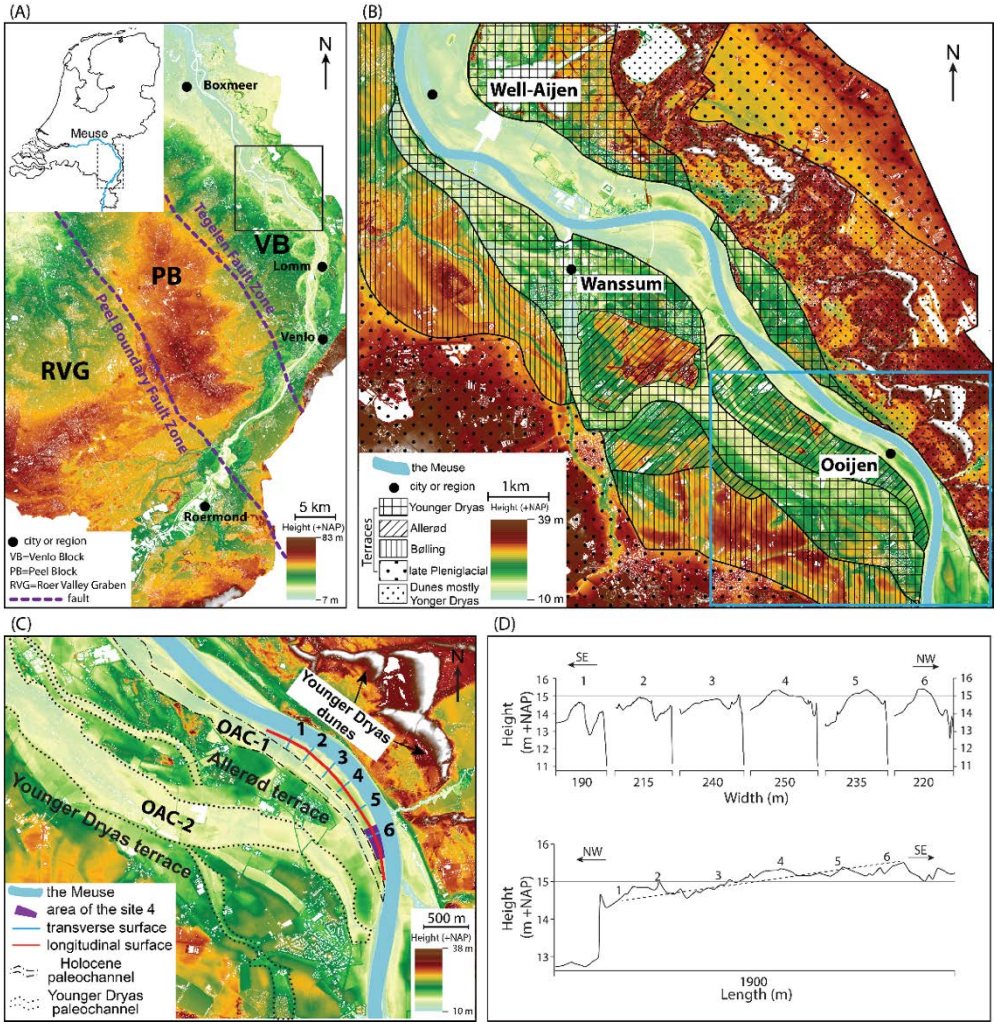

Figure 3.1. (A) Digital elevation map (DEM) of the southeastern Netherlands with Lower Meuse (dashed box in the insert) and the tectonic blocks. The uplifting Peel Block (PB) is separated from the subsiding Venlo Block (VB) and Roer Valley Graben (RVG) by fault zones (Van Balen et al., 2005). The light-green area depicts the distribution of the Holocene floodplain, from which it shows a narrow floodplain on the PB, that gradually widens at the VB. Solid box shows the study area (Ooijen). (B) DEM including the Ooijen and Well-Aijen, Late Glacial and Late Pleniglacial terraces (after Kasse et al., 1995). The light-green area along the Meuse River is the Holocene floodplain. Blue box delineates the Ooijen area depicted in (C). (C) DEM of the study area near Ooijen. The dashed lines outline the abandoned channels including OAC-1 and OAC-2. OAC-1 separates the investigated levee from the Allerød terrace. West and East of the Meuse, Late Glacial terraces and Younger Dryas dunes are present (Kasse et al., 1995). Red line shows the convex part of the levee, and six transects were chosen to show the morphology of the surface. The locations of trench-41 and trench-57 are situated at transects 3 and 2 of the levee, respectively. The purple area depicts a previous archeological site (site 4, see Section 3.5.1). (D) The topographic transects perpendicular (upper diagram) and parallel to the levee (lower diagram). The levee at transect 6 is ~0.9 m higher than the levee at transect 1.

3.3. Material and methods

3.3.1. Location selection, archeological investigations and sampling

To control future flooding events in the Lower Meuse valley, the floodplains and river banks have been and will be lowered. Prior to the digging activities, a series of archeological investigations have been carried out in the last two decades in the Well-Aijen and Ooijen-Wanssum areas (Fig. 3.1A, B; and see Isarin et al., 2017 and references therein). The main goals of these investigations were to reconstruct the paleoecological and paleogeographical developments, and to trace prehistoric human activity. The chronological framework was based on artefacts (mainly flint and pottery) typology, combined with OSL and ^{14}C dating (Ellenkamp et al., 2018).

In 2016, a project (code: OOYWA2) was carried out near Ooijen (Fig. 3.1C, center coordinate: 51.51° N, 6.16° E). Boreholes, cross sections and trenches were drilled and excavated in the levee. The results from these investigations (Ellenkamp et al., 2018), including the lithostratigraphical subdivision and chronology based on cultural periods, were used in this study. We also adopted the labelling of the seven units. The samples for sedimentary analysis were obtained from three vertical sections in trench-57, located close to the northwestern tip of the levee (transect 2 in Fig. 3.1C). We did not take samples in trench-41 (transect 3 in Fig. 3.1C), located near the central part of the levee because this trench was no longer available for sampling. However, the stratigraphical information from this trench is also described below, based on Ellenkamp et al. (2018), because it provides useful information about the general evolution of the levee. The lengths of the three sampled vertical sections in trench-57, sections A, C and B, are 256 cm, 230 cm and 204 cm, respectively. Based on the results of the archeological investigations, the three sections are semi-continuous and span approximately the last 10,000 yr of the Holocene period (from the Mesolithic to modern time). The sampling resolution adopted in the vertical sections is 2 cm. This interval is approximately equal to 100 yr of sedimentation, which we consider to be a resolution suitable to determine flooding phases on a centennial and millennial time-scale.

3.3.2. Magnetic susceptibility (MS)

The mass-specific MS (χ) was measured using an Agico Multi-function MFK1-FA Kappabridge in the paleomagnetic laboratory at Utrecht University. All the measurements were carried out with a frequency of 976 Hz.

In previous decades, a large volume of papers has reported the MS records of loess, lacustrine and marine sediment sequences (e.g. Thompson et al., 1975; An et al., 2001; Litt et al., 2001; Vandenberghe et al., 2004; Lee et al., 2008; Ao et al., 2010; Herb et al., 2013). The correlation between MS variations and other lithological and geochemical proxies (like grain size composition, soil layers and isotope data) is widely used in paleoclimatology, but few MS records for Holocene fluvial levee sediments have been reported up to now. Variations of MS in levee sediments might reflect changing fluvial transport and/or sediment source conditions, and can also represent local soil formation.

3.3.3. Thermogravimetric analysis (TGA)

Thermogravimetric analysis is used to obtain the loss-on-ignition (LOI) (Heiri et al., 2001) for each sample. The analysis is performed on a Leco TGA701 analyzer at Vrije Universiteit Amsterdam. The mass loss of each sample was obtained in a process of stepwise heating from room temperature to 1000°C to obtain the organic matter fractions. We used the LOI550 (loss-on-ignition at temperature 550°C) to determine the total organic matter content (TOM) in this study. Organic matter content can provide information on the maturity of the soils (Boyle, 2004; Santisteban et al., 2004).

3.3.4. Grain size analysis and end-member modelling

The method described by Konert and Vandenberghe (1997) was used for sample preparation prior to grain size analysis. For each sample, 10 ml 30% H2O2 and 5 ml 10% HCl was used to remove organic matter and calcium carbonates, respectively. After pretreatment, grain size distributions (GSDs), ranging between 0.1 and 2000 μm, were measured with a Sympatec HELOS KR laser-diffraction instrument at Vrije Universiteit Amsterdam. The grain size analysis resolution is 2 cm for sections A and B, and 4 cm for section C.

We used end-member modelling to decompose the whole GSDs dataset from the three sampled sections into a series of end members. The end members can be interpreted in terms of sediment source, transport and deposition, which cannot be identified using univariate grain size parameters alone (Prins et al., 2007; Van Hateren et al., 2018). Here, we applied the AnalySize end-member modeling package (Paterson and Heslop, 2015). A class-wise r2 was used to determine the minimum number of end members needed to adequately describe the GSD dataset (Paterson and Heslop, 2015; Van Hateren et al., 2018). The end-member mixing coefficients are used to determine the temporal flood energy variability by calculating an end-member ratio that highlights variability in the coarse end of the grain size distributions, i.e., the bedload component of the levee sediments.

3.3.5. Chronology

The sediments in trench-57 are mainly composed of sand, silt and silty clay. No organic macro remains suitable for ^{14}C dating were observed. Meanwhile, the clastic materials used for OSL dating have systematically produced ages that are too old and contradictory to the obtained archaeological information (Ellenkamp et al., 2018). In this context, we constrain the chronological framework to archeological periods. We define the formation time of each unit to archeological periods rather than constructing a conventional radiometric-dating-based chronology model. The stratigraphic position of the archeological remains from each subunit horizon and ^{14}C dating information from adjacent trenches in the same levee (Ellenkamp et al., 2018) played important roles in constraining the ages of the different units. Chronological information (the start and end of each unit) from subunit 4Ab upwards is derived from archeological results (Ellenkamp et al., 2018). The age interval for each archeological period is based on the Table 4.1 from Ruijters et al. (2017). The ages of underlying subunits 4C and 4BC are

inferred from the stratigraphic relationships and a previous paleochannel study (OAC-1) (Tebbens et al., 1999).

3.4. Results

3.4.1. Geomorphological analysis

A digital elevation map (DEM) of the study area, and its interpretation, are shown in Figs. 3.1B and 3.1C. The levee has a SE-NW orientation and its total length is ~1.9 km (Fig. 3.1C, D). The DEM and six cross-sectional topographic plots show a general slope of the crest of the levee of 0.092 m/m to the NW (Fig. 3.1C, D). In a transverse direction (SW), the topography of the levee has a minor slope of 0.012 m/m (Fig. 3.2). To the SW of the levee, an old channel (OAC-1) separates the investigated levee from the Allerød river terrace (Fig. 3.1C). This channel was abandoned in the early Holocene (Tebbens et al., 1999). Farther to the west another abandoned channel (OAC-2) is present (Fig. 3.1C). This channel incised into the Younger Dryas terrace; it was abandoned at the end of the Younger Dryas (Kasse et al., 1995). However, because of the low elevation of channel OAC-2, it may have functioned as a secondary channel during high floods in the Holocene. With the three sampled sections, trench-57 is located near the northwestern end of the levee (transect 2; Fig. 3.1C, D), in a relatively low position, which provided optimal conditions for completeness of the sedimentary record.

3.4.2. Stratigraphic descriptions and sedimentary results

Generally, the sedimentary sequence (in trench-57) shows a homogeneous structure, without visible flood laminae. The levee deposits in trench-57 have been grouped into seven sedimentary units (Ellenkamp et al., 2018). The subdivision is based on sediment texture, soil structure and color. Most units were subdivided into 2-3 subunits based on soil characteristics (Ellenkamp et al., 2018) (Fig. 3.2). The vertical and lateral variations of MS, TOM and median grain size in the vertical sections combined with the stratigraphic subdivision are shown in Fig. 3.3. The GSDs of each unit have similar characteristics in the three sampled sections.

End-member modelling results show that a four-end-member model is capable of explaining more than 95% of the total grain size variation (Fig. 3.4a), and its performance is consistently high throughout the dominant size range (Fig. 3.4b). EM1 has a primary mode at 60 μm and a secondary mode at 5 μm. EM2, EM3 and EM4 all have a unimodal distribution, with modes at 230 μm, 420 μm, 840 μm, respectively (Fig. 3.4c). We also decomposed the GSDs into five, six and seven end members. These models show that EM1 cannot be further decomposed by increasing the number of end members. A clear feature of the results is that, in each section, the variation of fine EM1 roughly parallels the MS and TOM variations (Fig. 3.3) and has an opposite relation to the median grain size variation.

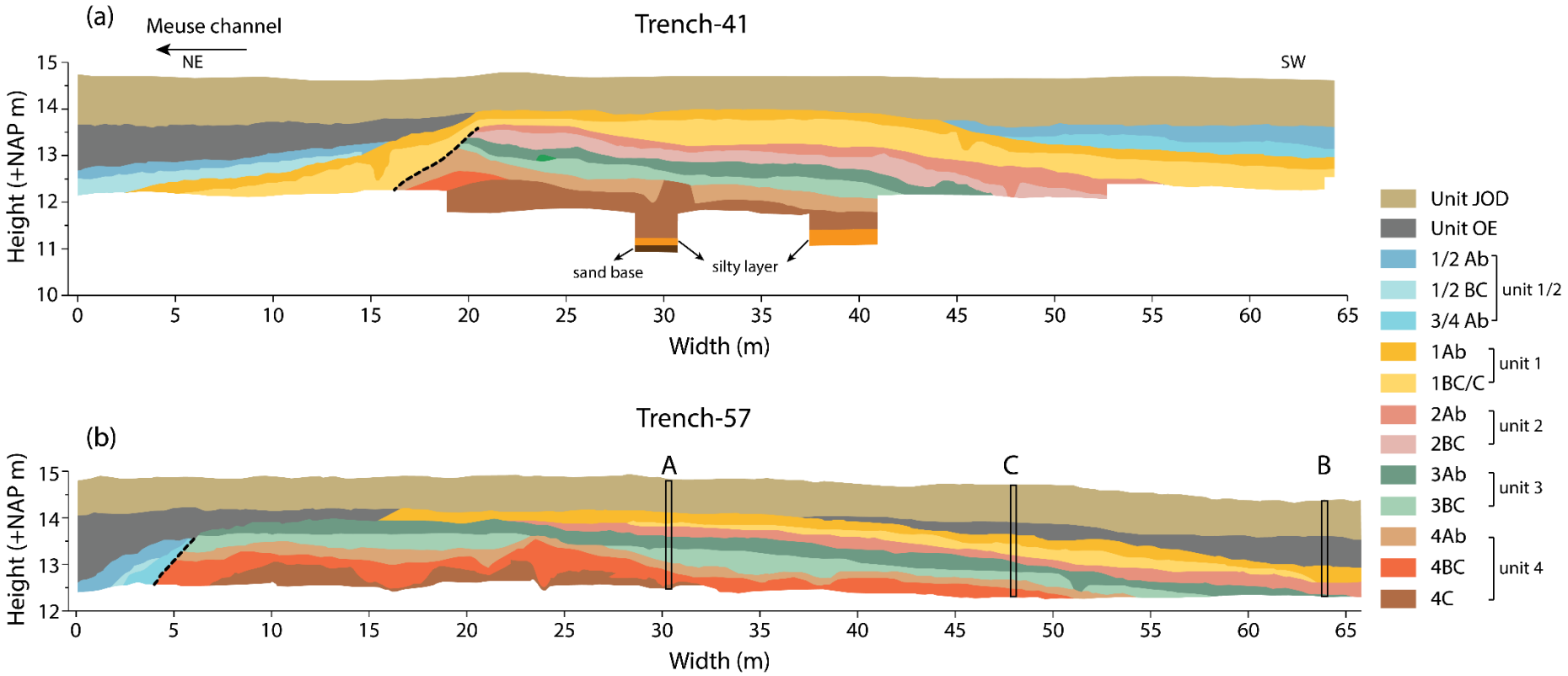

Figure 3.2. Seven units are shown in the stratigraphical profiles of trench-41 (a) and trench-57 (b). The vertical bars in (b) signify the positions of the sampled sections A, C and B. Trench-41 and trench-57 are situated at transects 3 and 2 of the levee (Fig. 3.1C), respectively. Please refer to Table 3.1 for archeological periods. Dashed lines show the erosional contact. NAP = Amsterdam Ordnance Datum.

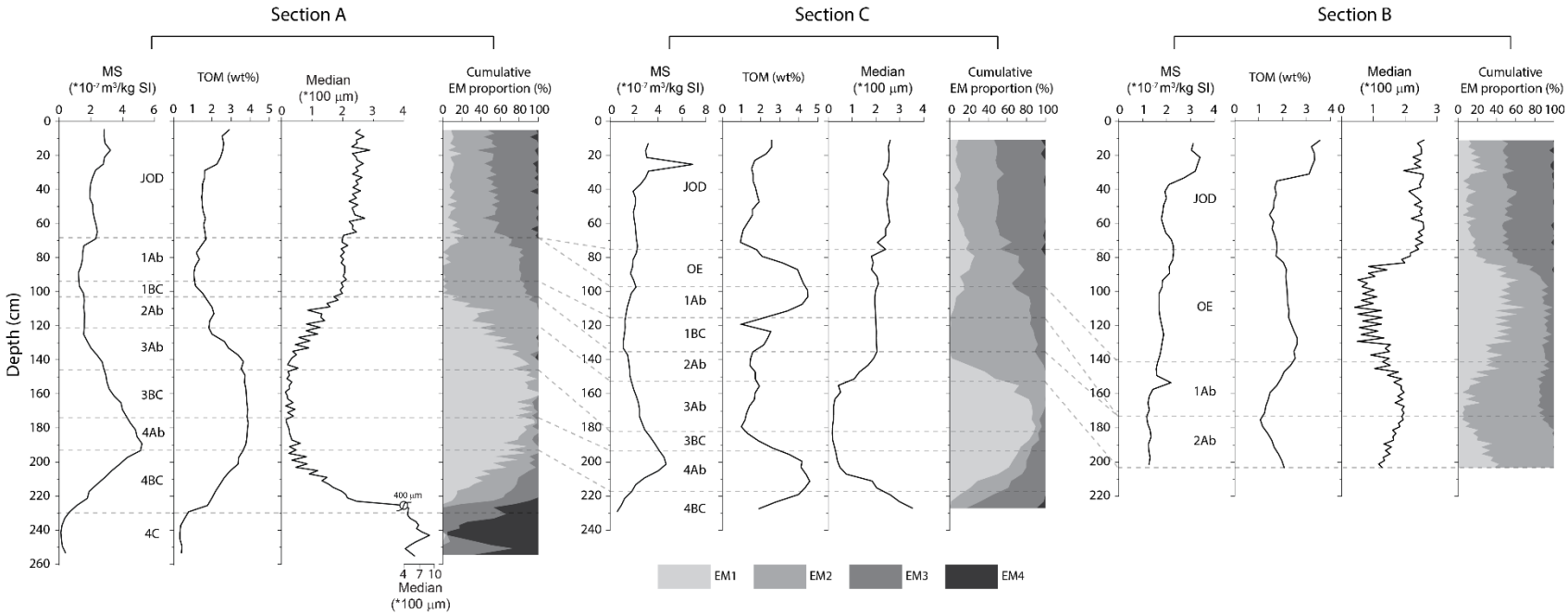

Figure 3.3. Sedimentary characteristics of the three sections. For each section, the magnetic susceptibility (MS), total organic matter (TOM), median grain-size and the cumulative end-member (EM) proportion records are shown from left to right. Note a cut-off at 400 μm in the median grain size curve in section A. The EM proportions are derived from the EM modelling analysis. The dashed lines show the correlation of the units in the sections. Sampling in section B starts from 2Ab subunit upwards. The OE unit is missing in section A and well developed in section B.

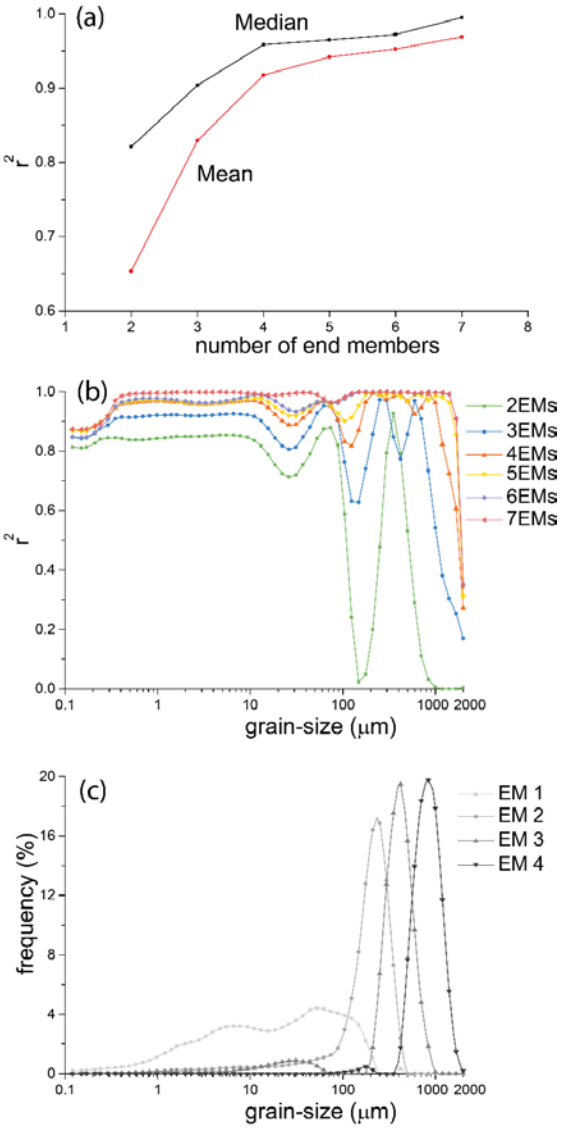

Figure 3.4. The end-member modelling results. (a) The median and mean r^2 across all grain size classes as a function of the number of end members. A four-end-member model is sufficient to explain more than 95% of the total variance. (b) r^2 for each size class for end-member models with two to seven end members. (c) The end members according to the four-end-member model.

3.4.2.1. Very coarse sand and clay deposits at the base

The basal sand and clay sediments were only exposed in trench-41 (Fig. 3.2a), which was no longer available for sampling; they were not encountered in trench-57 because of a high groundwater level. The sediments are yellow-brown, poorly sorted and consist of silty clays overlying the very coarse sands. Grain size and MS analyses were not performed for these sediments. Below we describe the sedimentary results (MS, TOM and grain size) in the framework of the archeological subdivision because the variations of the sedimentary characteristics largely coincide with the archeological subdivision.

3.4.2.2. Unit 4 (4C-4BC-4Ab)

Unit 4 has the largest thickness and has been well preserved in the center of the levee (section A); it thins toward the western part of the trench (Fig. 3.2). This unit was not exposed in section B because of the high groundwater level.

This unit consists of three subunits with different colors and textures (Fig. 3.5a). Subunit 4C features a clearly horizontally layered structure (Fig. 3.5a) and consists of brown-yellow, rusty sand deposits. Small shell fragments were observed in this subunit. The MS and TOM in 4C are very low, about 0.2 x10-7 m3/kg and 0.3 wt%, respectively, and the median grain size varies between 400 and 850 μm. Subunits 4BC and 4Ab show dark brown colors and a homogenous structure indicating soil formation (Fig. 3.5a). In section A, the MS and TOM show a consistent increase from 0.6 to 5 x10-7 m3/kg and from 0.7 to 4 wt% in 4BC, respectively. Subsequently, the MS drops slightly while the TOM remains unchanged in 4Ab. In section C, the TOM shows a different behavior in 4Ab where it drops after reaching high peak values (4 wt%). The median grain size rapidly decreases to ~20 μm in the two subunits (Fig. 3.3).

Overall, unit 4 shows a fining-upward trend in sections A and C, (Fig. 3.3). This is reflected by the median grain size record, but even more clearly by the end-member modelling results: the coarse end member EM4 is only dominant in subunit 4C, whereas the proportion of the finest end member, EM1, steadily increases upwards to 90% in 4Ab (Fig. 3.3). In addition, the grain size compositions in sections A and C show a synchronous variation (Fig. 3.3); there is no clear lateral grain size change, indicating vertical aggradation on a levee setting, instead of, for example, deposition by lateral point-bar migration. Subunit 4Ab is the oldest sedimentary layer in which early-middle Mesolithic archaeological remains have been found.

3.4.2.3. Unit 3 (3BC-3Ab)

Unit 3 differs from the underlying unit 4 by its brownish and darker color and densely distributed small burrows indicating soil formation during deposition (especially in subunit 3BC, Fig. 3.5b). This unit contains finer sediments (silty clay, featuring a soil layer) and was not exposed in section B. This unit is subdivided in two subunits, 3BC and 3Ab. Subunit 3BC has a brown color and 3Ab shows a slightly darker color (Fig. 3.5b, c). The sediments exhibit a homogenous structure and no laminae were observed. Subunit 3Ab has recognizable charcoal spots (not shown here) that were rarely observed in underlying subunit 3BC. Hence, subunit 3Ab was used as a “guide layer” for correlation during the field investigation.

In sections A and C, the MS decreases upwards steadily from ~4.0 to 1.8 x10-7 m3/kg (Fig. 3.3) while the TOM records show different patterns. In section A, the TOM value remains high (~3.7 wt%) in subunit 3BC and decreases to 1.9 wt% in subunit 3Ab, but in section C the value decreases sharply (from 4.6 to 1.1 wt%) in subunit 3BC and rises to 1.7 wt% in subunit 3Ab (Fig. 3.3). The median grain size has little variation in 3BC but begins to increase gradually to 100 μm in 3Ab in sections A and C (Fig. 3.3). Corresponding with a coarsening-upward trend, the dominant very fine EM1 in subunit 3BC gradually decreases to about 40% in subunit 3Ab, and the contribution of coarser EM2 rises to around 45% (Fig. 3.3). In the whole unit the proportion of EM3 is very limited (<10%).

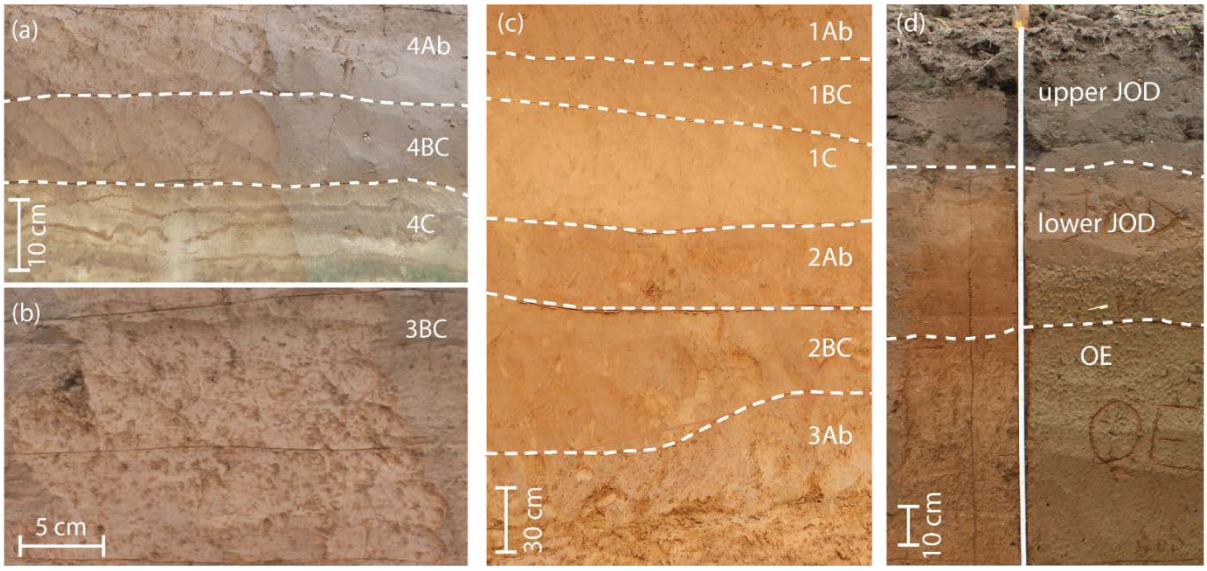

Figure 3.5. Photographs of each (sub)unit of the Ooijen levee deposits. Dashed lines in each panel represent (sub)unit boundaries. (a) Unit 4 consists of sand at the base and shows a fining-upward trend in the grain size composition. Subunit 4C features horizontally bedded sand with some clay-iron illuviation laminae and 4Ab is a developed soil layer with brownish color. (b) Subunit 3BC has a brownish color and densely distributed burrows. (c) Unit 2 and overlying unit 1. Composition of subunit 2BC is coarser than the underlying 3Ab subunit. Subunit 1C has yellow-brown color and is coarser than the underlying 2Ab. Soil formation in 2Ab is less pronounced than in 3Ab. (d) Units OE and JOD exposed in the west part of trench-57. A clear boundary exists within JOD between the lower layer (previous plough sublayer) and the upper layer (plough sublayer).

3.4.2.4. Unit 2 (2BC-2Ab)

In the field, unit 2 was distinguished from the underlying clay-rich subunit 3Ab by its sandy composition (Fig. 3.5c). In trench-57, only subunit 2Ab was present. This subunit represents a soil layer with dark brown color. The yellow-brown subunit 2BC was only present in trench-41 (Fig. 3.2). The MS, TOM and median grain size show similar vertical variations in the three sections (Fig. 3.3). The MS has small variation at around 1.2 x10-7 m3/kg, and the TOM decreases slightly to 1.3 wt% (Fig. 3.3). The median grain size steadily increases from 100 to 200 μm (Fig. 3.3). This is also reflected in the end-member modelling results, where the EM2 proportion increases upwards and accounts for more than 75%, at the expense of a decreasing EM1 (Fig. 3.3). EM3 occurs in very low abundances near the top of the unit, whereas EM4 is absent throughout unit 2.

3.4.2.5. Unit 1 (1C/1BC-1Ab)

Unit 1 differs from unit 2 by its coarse-grained texture and brownish yellow color (Fig. 3.5c). In trench-41, subunits 1C, 1BC and 1Ab were distinguished (Fig. 3.2a). At the eastern part of the levee, unit 1 overlies the older units 2-4 with an erosional contact related to reactivation of the Maas channel (Fig. 3.2a). In trench-57 only 1BC and 1Ab were exposed (Fig. 3.2b). Subunits 1BC/C consist of yellow-brown, silty to fine and coarse sand. The sediments in subunit 1Ab have a darker brown color and are coarser than underlying sediments. There are no clear laminae observed in this subunit and the depositional profile shows a homogenous structure.

From subunit 1BC to subunit 1Ab in sections A and C, the MS increases slightly from 1.1 to 2.2 x10-7 m3/kg (Fig. 3.3), and the TOM record generally shows first a decreasing trend in subunit 1BC, but subsequently an increasing trend in the soil layer corresponding with subunit 1Ab (Fig. 3.3). The TOM increase is most pronounced in section C (Fig. 3.3). The median grain size shows little variation (with averages of 200 µm) in sections A and C, but decreases from 200 to 140 µm in section B. Interestingly, all three sections show a similar trend in their cumulative EM graphs: a simultaneous increase of EM3 and EM1 at the expense of a EM2 decrease in subunit 1Ab (Fig. 3.6). This is different in the underlying units, in which the proportions of fine end members increase (decrease) as the coarse end members decrease (increase) (Fig. 3.6).

3.4.2.6. Unit 1/2 (½ BC, ½ Ab and ¾ Ab)

Unit 1/2 was discovered in the later stage of the archeological investigations and was not sampled. This unit is only present at the flanks of the levee (Fig. 3.2). The deposits have a similar texture as those of unit 1 and are coarser than the overlying OE sediments. Based on color and texture, three subunits were defined, ½ BC, ½ Ab and ¾ Ab. In the east, these sediments dip toward the Meuse channel (Fig. 3.2) and sharply overlie the older units 3 and 4 with an erosional contact (Fig. 3.2b). In trench-41, the ½ BC and ½ Ab subunits were present at the northeastern part of the levee, and ½ Ab and ¾ Ab were found at the southwestern part.

3.4.2.7. Units OE and JOD

The OE unit covers the subunits ½ BC, ½ Ab and ¾ Ab at the eastern flank (OE and JOD are abreviations for the Dutch words “oeverafzettingen” and “jong overstromingsdek”, respectively). At the western part of trench-57, the OE unit directly overlies the subunit 1Ab. The OE unit was exposed in sections B and C (Fig. 3.3). The overlying JOD unit is subdivided into two parts: an upper plough sublayer (produced by modern farming) with darker color and an underlying previous plough sublayer with less organic matter and lighter color (Fig. 3.5d).

In the two units, the MS varies at 2.0 x10-7 m3/kg with a slightly increasing trend to ~3 x10-7 m3/kg towards the top of unit JOD. In section C, the TOM rapidly decreases from 4.5 to 1 wt% in OE and then increases to 1.5 wt% in the lower JOD sublayer, and in section B the TOM gently decreases from 2.7 to 1.5 wt% (Fig. 3.3). In the lower to middle intervals of OE (below the depth of 80 cm in section C and 90 cm in section B), the median grain size shows a decreasing trend, and the proportions of EM1 continue to increase whereas the proportion of EM3 decreases slightly. This feature is different from that in subunit 1Ab. Above the depth of 80 cm in section C and 90 cm in section B, the median grain size increases to ~240 µm in the JOD unit (Fig. 3.3). In line with this result, the proportion of EM1 decreases to 10% and the proportion of EM3 increases to 50% in JOD unit (Fig. 3.3). The proportion of EM1 in unit OE from section B is about two times higher than in section C. In the JOD unit, the proportions of EM1-EM3 reach similar values, but the coarsest EM4 also appears occasionally (Fig. 3.3).

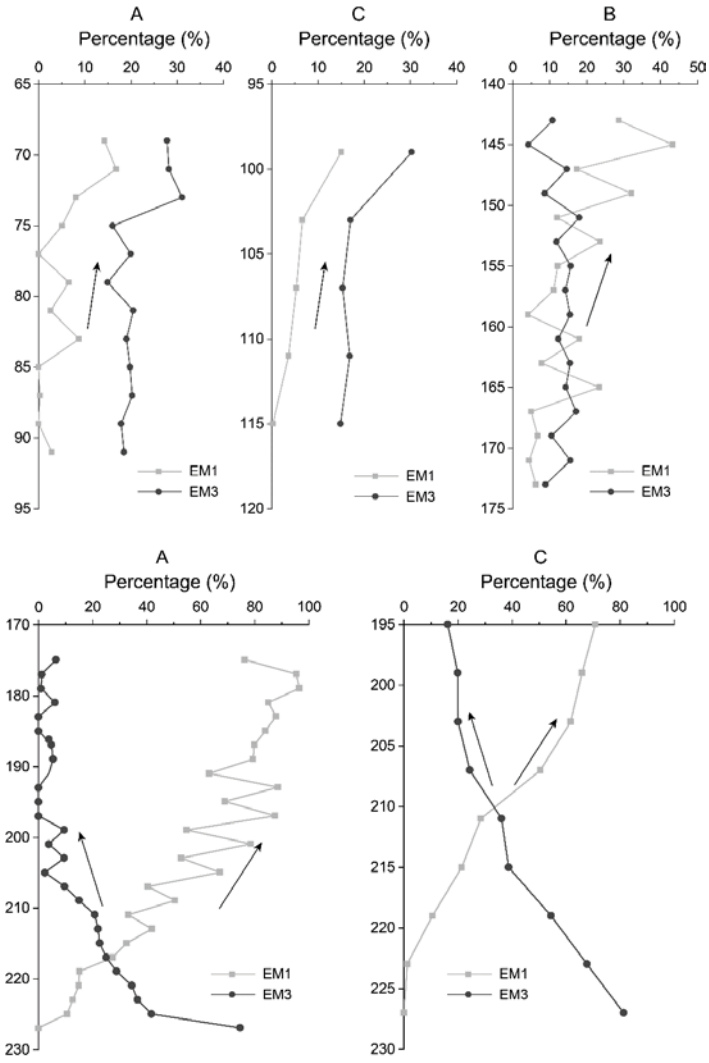

Figure 3.6. The proportions of EM1 and EM3 in the four-end-member model in three sections from subunit 1Ab (upper panel) and 4BC-4Ab (lower panel). The variations of the two end members show that EM1 (suspended load) and EM3 (intermediate bedload component) increase simultaneously in subunit 1Ab, while in unit 4 they have opposite changes.

3.4.3. Chrono-stratigraphic framework and age-model

Tebbens et al. (1999) obtained samples from the base of the OAC-1 paleochannel that were ^{14}C dated at 9170±200 (calibrated median age: 10,369 BP; calibrated with IntCal 13 curve (Reimer et al., 2013)), which gives a minimum age of the OAC-1 channel abandonment. A ^{14}C date from the 4Ab subunit at the investigated levee (close to transect 2, Fig. 3.1C) produced an age of 8930±40 (calibrated median age: 10,046 BP). Zuidhoff and Huizer (2015) reported an OSL age (9900±900) for the point-bar deposits obtained from 1.9 m beneath the present-day surface (between transects 3 and 4, Fig. 3.1C). During this time the Meuse channel flowed at the present levee location. Considering the uncertainty, the time interval of the two ^{14}C ages (both calibrated ages fall into the middle Mesolithic) agrees with the OSL age and further constrains the minimum ages of subunits 4C and 4BC that formed during the early/middle Mesolithic.

In subunit 4Ab, the archeological findings of land use and habitation (fireplaces, flint processing sites and processed tools) feature early-middle Mesolithic characteristics (Fig. 3.7a). This is evidenced by a ^{14}C date (8930 ± 40, Table 3.1) at the base of 4Ab, which indicate an age for this subunit of ca. 10 ka cal BP. The estimated sedimentation rate is 9 cm/kyr for subunit 4Ab (Fig. 3.8).

At the transition of subunits 4Ab to 3BC, hearths and stone processing sites were found. The allochthonous materials, such as Wommersom quartzite and Obourg flint belong to the Sauveterrien cultural period (8.5-6.5 ka BP). Subunit 3BC showed a high intensity of land use and stone and flint processing, and a large number of artefacts (25,300 pieces of flints) that were dated in the late Mesolithic (8.4-6.9 ka BP) (Fig. 3.7b). Two ^{14}C dates provide a solid age for this period (Table 3.1). The sedimentation rate for 3BC is 17 cm/kyr. At the transition of subunit 3BC to 3Ab, late Mesolithic (8.4-6.9 ka BP) artefact assemblages were found (Fig. 3.7c), including flint processing sites and the first presence of potteries. Therefore, we conclude that subunit 3BC formed during the interval of 8.4-6.9 ka BP (Fig. 3.8). In the lower part of subunit 3Ab, potteries with Bischheim/Swifterbant and LBK (Linear Pottery Culture, 7.5-6.5 ka BP) cultural characteristics (Fig. 3.7d) were found. Hence, the lower 3Ab sediments may have formed at the transition to early Neolithic. In the surface of 3Ab, late Neolithic potteries, flints and natural stones were found (Fig. 3.7e). Therefore, the middle to top part of the subunit 3Ab was formed during the middle-late Neolithic, and two ^{14}C dates provide ages (Table 3.1) in agreement with a middle Neolithic period. Hence, subunit 3Ab was formed during the Neolithic (6.9-3.9 ka BP) and its sedimentation rate is about 9 cm/kyr (Fig. 3.8).

In the highest part of subunit 1Ab on the studied levee, Iron Age potteries and Middle Age artefacts were found. These two periods were separated on the flanks of the levee, in which the Iron Age findings were found in subunit 1Ab (Fig. 3.7f) while early Middle Ages findings were embedded within OE deposits. This indicates that subunits 1BC-1Ab have formed in the Iron Age and that the OE sequence as formed during the early Middle Ages (Dark Ages). Based on that, we calculate the sedimentation rates during the Iron Age and Middle Ages to be 45 cm/kyr and 21 cm/kyr, respectively. Therefore, subunit JOD was formed during the late Middle Ages as it overlies the Middle Ages pottery, and this is corroborated by an OSL date at the base of JOD. The sedimentation rate in JOD reached the largest level, 86 cm/kyr. Unit 1/2 was buried under the OE subunit and overlies subunit 1Ab. Therefore, unit 1/2 was likely formed during the time period between the Iron Age and early Middle Ages (possibly in the Roman Period). Constrained by the youngest findings (late Neolithic) in subunit 3Ab and the oldest findings (early-middle Iron Age) in subunit 1BC, it is reasonable to infer that subunit 2Ab was deposited during the Bronze Age. However, during the archeological investigation, little archeological finds were found that could provide solid evidence for a Bronze Age habitation on the levee. We obtained the sedimentation rate of 15 cm/kyr for Bronze Age.

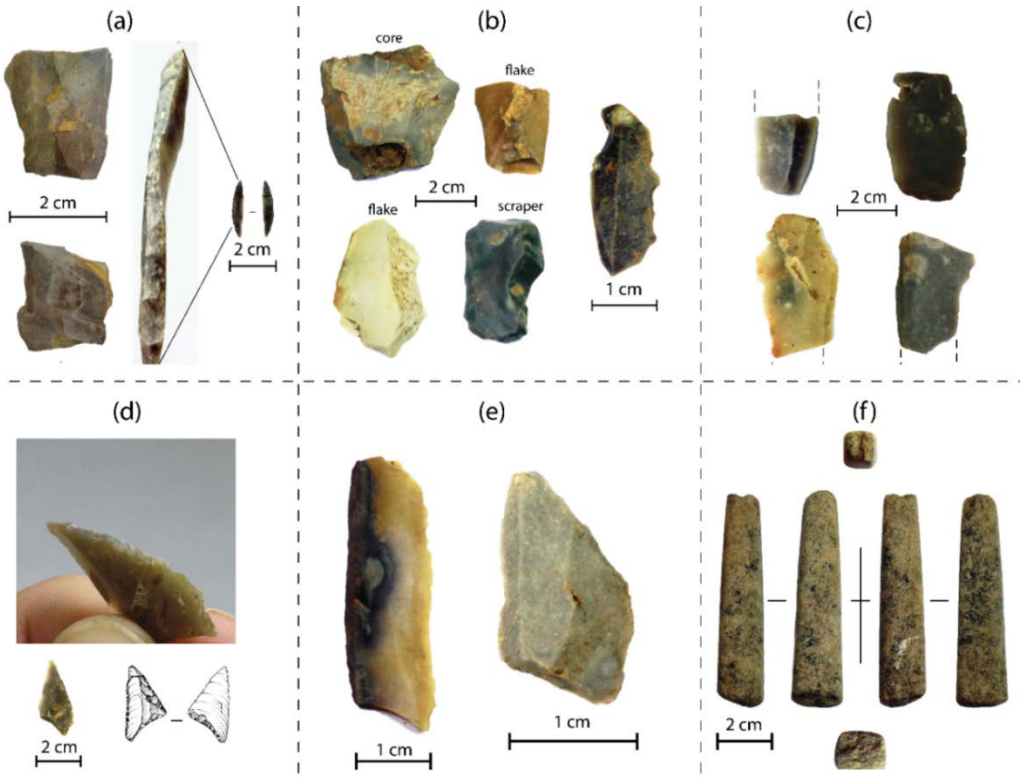

Figure 3.7. Selected artefacts from the archeological investigations (Ellenkamp et al., 2018) on the levee from different cultural periods. (a) Lanceolate microlith-point with totally retouched side-edge from subunit 4Ab. (b) Late Mesolithic denticulate blade from 3BC subunit. The four on the left are a core, a flake and a scraper made from flint. The one on the right is a flint tool. (c) Upper-left is the lithic flake found at the 3BC-3Ab interface (late Mesolithic), and its distal end was made from glassy flint. The other three are flints used for lithic manufacturing processes. (d) Trapezoidal point with retouched long edge and base-point from 3Ab subunit with Neolithic feature. (e) Left is a micro-blade made from coastal-flint pebble, right one is a trapeze with broken top-end (impact-fracture) from the upper part of 3Ab. (f) Iron Age wetstones or fragments of stone pendant with a quadrangular cross section discovered in subunit 1C. The tools are made of fine-grained stones and were processed to smoothen and flatten their surface.

Based on the above derived chronostratigraphic information, the age-depth model for each levee section is constructed (Fig. 3.8). In section A, the Roman Period and Middle Ages deposits are absent (Fig. 3.8). In section C and B, only the Roman Period deposits are absent (Fig. 3.8). To reflect the temporal variation of the paleofloods for each cultural period, the ages were linearly interpolated within each cultural period according to the upper and lower age boundaries. In section 3.5.3 we discuss the rationality of this method.

3.4.4. Flood energy reconstruction based on decomposed levee grain size records

The distinctly different grain size distribution of EM1 in comparison to EM2-EM4 indicates that the fine-grained EM1 represents a different transport process than EM2-EM4. In addition, the consistent presence of EM1 in the four, five, six and seven end-member models imply that EM1 cannot be decomposed and represents a single transport process. In this levee context, we interpret the finest EM1

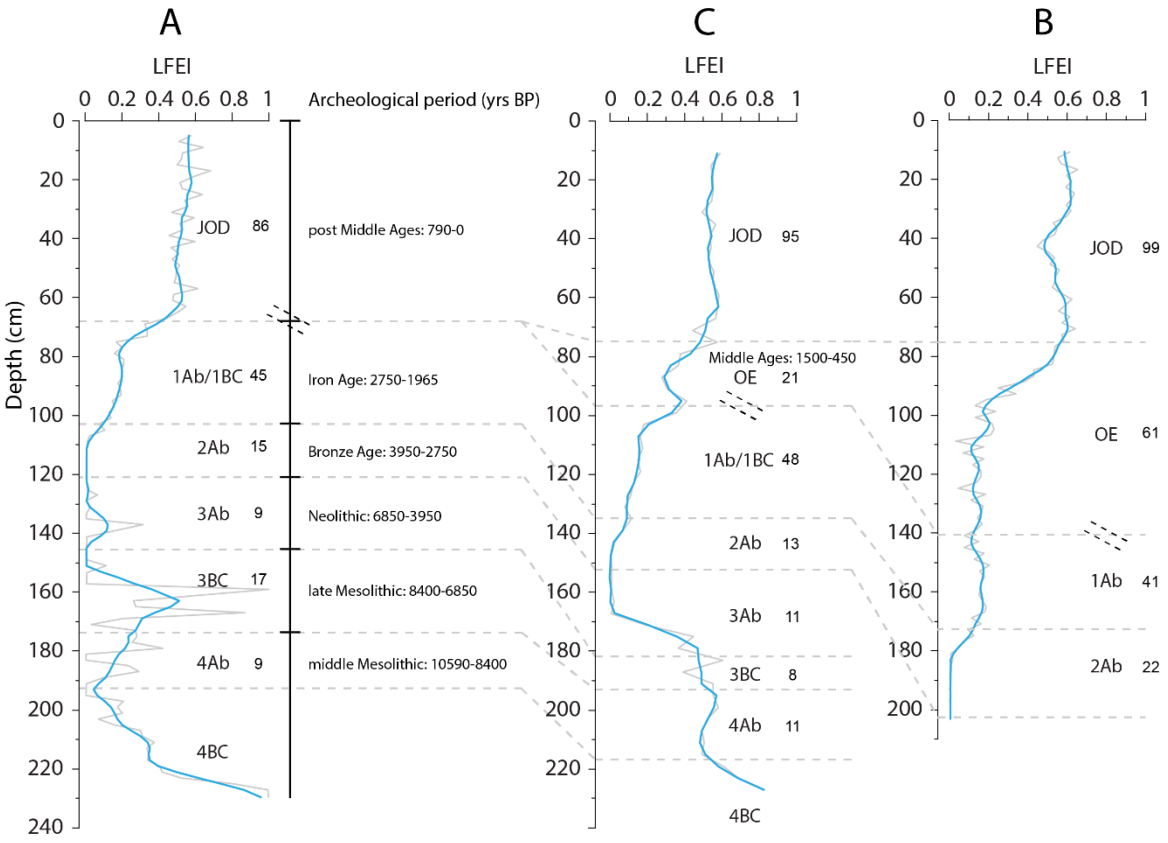

Figure 3.8. The levee-based flood energy index (LFEI) and chrono-stratigraphic correlations. The grey curves represent all data points. The blue curves are smoothed LFEI records by using a locally weighted polynomial smoothing function (LOESS) to prevent undue emphasis being placed on single data points. The horizontal dash lines indicate the boundary of each cultural period in each section. The diagonal dash lines indicate the sedimentary hiatus. The numbers along the curve are calculated sedimentation rate (cm/kyr) in each period. In section A, the Roman Period and Middle Ages deposits are absent. In section C and B, only the Roman Period deposits are absent.

as suspended sediment load and coarse EM2-EM4 as bedload (a very similar mixing model has also been observed in Rhine fluvial sediments (Erkens et al., 2013). The suspended load (EM1) and bedload (EM2-EM4) represent different hydrological/sedimentary transport processes. By constructing an index consisting of only the bedload end members, we are able to derive a proxy for flood energy variation, independent of the contribution of the suspended load.

Our levee sediments based Flood Energy Index (LFEI) is based on the ratio of the coarsest bedload end members, EM3+EM4, over the total sum of the bedload end members EM2-EM4:

$$LFEI=(EM3+EM4)/(EM2+EM3+EM4) \quad (1)$$

The LFEI records and the chronological information for the three sections are plotted against depth in Fig. 3.8. Because subunit 4C represents the top of point-bar deposits underlying the levee sediments (see Section 3.5.1) and no archeological artefacts were found in subunit 4BC, this study only focuses on the paleofloods since the middle Mesolithic (subunit 4Ab, from ca. 10590 a BP). The raw LFEI variation for each section was processed by using a locally weighted polynomial smoothing function

(LOESS) to prevent placing undue emphasis on single data points (Fig. 3.8). The temporal variation of the LFEI is shown for each levee section in Fig. 3.9.

3.5. Discussion

3.5.1. Longitudinal differential levee sedimentation

Unit 4 consists of coarse sand and sand-clay deposits, which in this fluvial context should be interpreted as channel or point-bar deposits and overlying floodplain deposits. Subunit 4C constitutes the top of point-bar deposits that formed during channel migration. Evidence are the coarse grain size characteristics (Fig. 3.3) and the embedded shell fragments, indicating a riverine environment. The fine-grained deposits from subunit 4BC to unit JOD formed after the channel had migrated to its present position. This means that the paleohydrological information, derived from the sedimentary analyses and archeological investigations, reflects the overbank flooding regime with vertical aggradation that was not influenced by lateral river migration.

The DEM analyses showed that the studied location is situated on a levee. The stratigraphic build-up and lithological composition show that the subunits 4BC to JOD are also deposited in a levee environment. For example, the convex lower units 3 and 4 represent a small levee in an early stage of deposition.

The accumulation process of the NW part of the levee is different from that of the SE part. Previous archeological investigations on the SE part of the levee (site 4 in Fig. 3.1C) have shown near-surface Neolithic pottery (Heunks, 2000). Hence it was concluded that the SE part of the levee was stable (almost no deposition) in the past ~7 ka. This is in strong contrast with the NW part of the levee, in which sediments were deposited with archeological remnants from the Mesolithic to the Middle Ages or Present. This indicates a different sedimentary and geomorphological evolution for the two parts of the levee. Two reasons are proposed to explain this. First, the northern part, where trench-57 and trench-41 are located, is situated on the more downstream inner bank of the channel bend (Fig. 3.1C). Small northeastward bend migration will have resulted in space for deposition on the inner bank. Conversely, the part of the levee at site 4 is located next to a straight channel that had nearly no lateral migration (Fig. 3.1C). Therefore, limited space has been produced for deposition at site 4. The second explanation is based on the slope of the crest of the levee during the early Holocene. Based on DEM information, the present average elevation at the NW part of the levee (trench-57) is ~14.6 m, which is ~90 cm lower than the SE part (Fig. 3.1D). A lower elevation at the NW part of the levee will have favored more sedimentation during flooding.

Unlike a commonly seen continuous sedimentation in floodplain settings, the Ooijen levee shows that sedimentation rates can be variable along a levee at the channel bend scale because of different deposition processes. This agrees with previous research in the region in which it was concluded that sedimentation and morphology varies between river bends and even within a single bend (Ruijters et

al., 2017). Therefore, morphological pre-investigations should be performed for locating the best spot (continuous sedimentation) on a levee for flooding reconstructions.

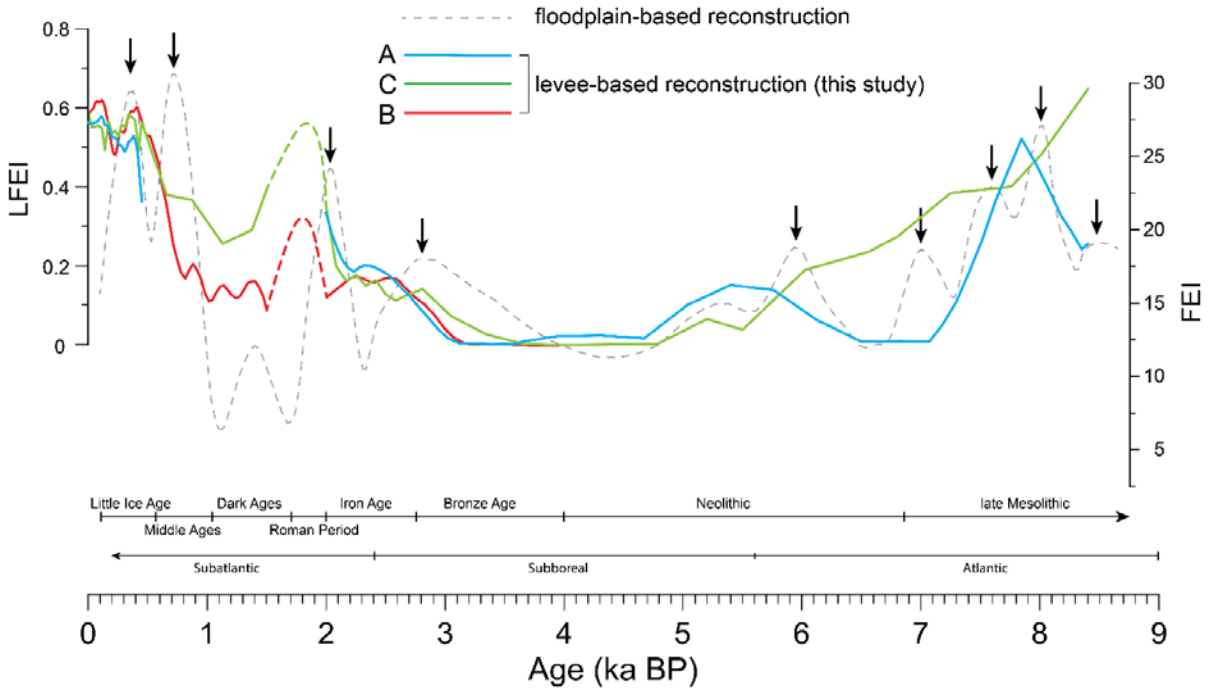

Figure 3.9. Holocene Lower Meuse paleoflood reconstructions based on floodplain sediments (FEI, grey dashed line) (Peng et al., 2019) and levee sediments (LFEI, colored lines, this study). The two independent reconstructions show a gradually weakened flooding regime during the Mesolithic followed by a low sedimentation rate and flooding activity during the Neolithic and Bronze Age. Instability of the fluvial behavior since the Iron Age is evidenced by a high sedimentation rate and more severe flooding. This trend is interrupted by the lower flooding phase in the early Middle Ages (Dark Ages). Colored dashed lines are inferred from the field observations (see Section 3.5.2.3).

3.5.2. The influence of flooding phases and human activity on levee sedimentation

The paleoflood reconstruction is based on grain size analysis of sediment units, soil characteristics and archeological finds that enable chronological control. During floods and flooding phases the sedimentation was more prominent, while soil formation and human activity were more important during low flooding conditions. However, it is emphasized that sedimentation, soil formation and occupation are not mutually exclusive on a levee setting. The increasing degree of soil formation (Ab layers) with depth (Fig. 3.5a-c), and the absence of parental materials (C horizons) indicate that the deposited sediments were transformed into soils immediately after sedimentation. Thus, soil formation and sedimentation took place concurrently on the levee. One should also bear in mind that other factors, for instance, the vertical growth of the levee, the change of sediment source and composition, and channel migration may complicate the interpretation of flooding variations. For example, the aggradation of sediments on the levee elevated its surface and this increases the threshold of bankfull discharge. In addition, human activity in the Meuse catchment since the Neolithic has altered the

sediment source and therefore the grain size characteristics of the sediment input to the fluvial system. Model simulations and field sediment investigations have shown that deforestation and farming from the mid-Holocene onwards in the Meuse catchment led to severe soil erosion and increased floodplain sedimentation, and to increased discharges (De Moor et al., 2008; Ward et al., 2008; Bos and Zuidhoff, 2015). A higher sediment load caused by increased anthropogenic activity will be reflected by higher sedimentation rates on the levee. Our LFEI index, however, reflects variations in flooding energy, which are the combined result of climate change (precipitation) and land-use change. Deforestation and agriculture activities resulted in increased runoff caused by decreased interception and evapotranspiration and less infiltration.

3.5.2.1. Decreasing flooding during the late Mesolithic

We interpret the 4BC as the transition from the point-bar environment to a levee setting, and this is shown by the gradually reduced grain size (Fig. 3.3). Gradually reduced river flooding since the middle Mesolithic can be inferred from the fine-grained subunit 4Ab-3BC deposits (Fig. 3.3), and from the high proportion of fine EM1 and low proportion of coarse EM2-EM4. The low flooding regime in the later stage of the Mesolithic partly accounts for the highly developed soil layers (4Ab-3BC) that are evidenced by high TOM and MS. The 3BC sediments show similarities with the underlying 4Ab subunit in section A with well-developed soil formation and fine sediments (Fig. 3.5a, b) implying the two subunits likely formed in the same flooding regime. The densely distributed burrows in 3BC are indicative for strong bioturbation. Bioturbation is unlikely to happen during a high flooding regime. A regime of lower river flooding activity favored prehistoric humans' occupation on the levee in the middle Mesolithic. The ^{14}C results and archeological findings (Table 3.1) from the two subunits indicate they formed during the middle Mesolithic (4Ab) and the late Mesolithic (3BC). The LFEI variations determined from section A decrease steadily through the late Mesolithic. This implies a reduced deposition of the coarsest bedload components, and thus lower flooding intensity. The low flooding conditions persisted through the late Mesolithic (subunit 3BC) until the start of the Neolithic (subunit 3Ab). During the late Mesolithic, anthropogenic activities increased, as indicated by the wide distribution of the different artefact types on the levee (Table 3.1, Fig. 3.7b-d), including homogenous flint concentrations, processed stones (these indicate that the research area had been a site for flint processing) and fireplaces. The archeological investigations concluded that the levee has been occupied for a long time during the Mesolithic period (Ellenkamp et al., 2018), but the human impact on the landscape was still limited (Bos and Zuidhoff, 2015; Peng et al., 2019) and unlikely to have resulted in an apparent change in the sediment source and composition. The low sedimentation rate (Fig. 3.8) supports this interpretation. The levee, directly seated on a point-bar deposit (subunit 4C), was at a juvenile stage at that time. These observations agree with the reduced LFEI, representing subdued flooding and decreased discharge on a millennial-scale. The top of subunit 3BC has a relatively flat

surface, which differs from the upper surface of underlying unit 4 (Fig. 3.2). This may be a result of long-term human activity that has flattened the ground surface.

3.5.2.2. Low to moderate fluvial activity during the Neolithic and Bronze Age

The Neolithic and Bronze Age sedimentary records show a coarsening-upwards trend, with a decrease of the proportion of fine EM1 (3Ab and 2Ab subunits in Fig. 3.3), indicating that the Lower Meuse changed from a low flooding regime in the early Neolithic into a moderate flooding regime during the late Neolithic and Bronze Age. In addition to the sedimentary observations, the magnitudes of the LFEI index in sections A and C also evidence a moderate flooding phase in the middle Neolithic and in the late Bronze Age, in between a low flooding intensity from the late Neolithic to the middle Bronze Age (Fig. 3.9). Middle to late Neolithic potteries and flints were found at the top of subunit 3Ab (Ellenkamp et al., 2018). The artefacts have a higher distribution density than the lower Mesolithic ones. This is mainly caused by a change in human behavior using the levee more intensively during the Neolithic than during the Mesolithic (Ruijters et al., 2017). Furthermore, the charcoal spots that were observed in subunit 3Ab, could be caused by human-induced fire events. These findings indicate a stable environment and human settlement during the Neolithic.

In the Well-Aijen floodplain area, which is located ~9 km NW of Ooijen (Fig. 3.1B), an increase of crop plants species (i.e., Cerealia, Plantago lanceolata and Anthoceros punctatus) was identified at the start of the Neolithic (Bos and Zuidhoff, 2015), indicating the increase of agricultural activities in the surrounding landscape (Bos and Zuidhoff, 2015). The small increase of the LFEI flooding index during the middle Neolithic (Fig. 3.9) may thus be related to increased runoff caused by farming and deforestation.

Very limited Bronze Age artefacts have been discovered in subunit 2Ab, hinting at a reduction of human activity on the levee. The soil formation in subunit 2Ab is less pronounced compared to the soil subunits 3Ab and 4Ab (Fig. 3.5a-c). Bos and Zuidhoff (2015) reported that human activity was still present in the Well-Aijen area but less pronounced than in the early-middle Neolithic (Fig. 3.1B). In the Netherlands and other regions of northwestern Europe, a population decline and socioeconomic collapse at the end of the Bronze Age have been suggested (Van Geel et al., 1996; Gerritsen, 2003; Armit et al., 2014). However, the causal relationship of the moderate flooding regime in the later stage of the Bronze Age and less human occupation on the levee is unclear, as this deterministic idea that population collapse at the end of the northwestern European Bronze Age was caused by rapid climate change in the Atlantic region is still under debate (i.e. Van Geel et al., 1996; Tipping et al., 2008; Armit et al., 2014).

3.5.2.3. High flooding and rapid sediment accumulation since the Iron Age

In the Iron Age, the direct evidence of gradually enhanced flooding is shown by the coarse median grain size of unit 1 and the increase of EM3 (bedload component) from subunit 1BC upwards, though the median grain size value decreases slightly in section B (Fig. 3.3). The archeological excavation revealed

evidence of erosion by the Meuse of the eastern flank of the levee, where parts of units 2-4 were eroded during the Iron Age (Fig. 3.2). The gradual combined increase of LFEI and sedimentation rate at the start of the Iron Age suggests that both are mainly caused by increased flooding. During the Roman Period (unit 1/2), erosion occurred at the eastern flank (Fig. 3.2b) which implies a high-energy depositional environment. This unit has not been sampled. During the archeological investigations, the sediments in this unit appeared coarser than the overlying OE unit. Therefore, we infer a more dynamic fluvial condition in the Roman Period compared to the early Middle Ages (Dark Ages). In the early Middle Ages, a decrease of the median grain size, a continuous increase of the fine EM1 (suspended load) and a decrease of the EM2-EM3 proportions in the lower to middle part of the OE unit are observed (Figs. 3.3 and 3.8). Low values of LFEI (Fig. 3.9) indicates a phase of relatively low flood magnitudes. It should be noted that the overall flooding activity inferred from LFEI in this period was still higher than in earlier times (Mesolithic). Since the middle to late Middle Ages a coarsening-upward trend occurred and the bedload end members are dominant (Fig. 3.3, upper part of OE). Minor contributions of the coarsest end member EM4 (with a mode at 840 µm) likely reflect intensified flooding after the Middle Ages (Fig. 3.3). High floods since the Iron Age seem likely considering the elevated levee height, because floods with constant and/or decreased magnitude were unlikely to have caused erosion of unit 4 and a coarsening-upward sequence.

In the Iron Age deposits (subunit 1Ab), the increased proportion of the fine end member (EM1, representing suspended load) in the upper part of subunit 1Ab (Fig. 3.6) indicates a relatively low-energy sedimentary environment. At the same time, the increased proportion of EM3 (Fig. 3.6) points to high-energy hydrodynamic conditions. Another characteristic of this levee is that the convex slope is gradually decreasing since the deposition of unit 1 (Fig. 3.2). Both the end member variation and the gradually flattened levee surface can be explained by the re-opening of the paleochannel OAC-1. This paleochannel is ~1 m lower than its present surrounding area and extends to the SE where it connects to the Meuse channel (Fig. 3.1C). During peak discharge events, water flowed through the depression, which could serve as a chute channel to accommodate excess water and carry suspended sediments to the west flank of the levee. The proximity of the west flank (sections B and C) to paleochannel OAC-1 could have led to relatively long-term inundation because the two sections were located at the lower elevations since the Iron Age (Fig. 3.2b). Consequently, the fine sediments (EM1) settled after the initial deposition of coarse sediments (EM2 and EM3). This interpretation agrees with units 2-4 being thicker in section A than in section B; whereas the younger subunits 1Ab and OE in section B are thicker than in A and C. In addition, the higher proportion of EM1 in OE in section B compared to section C also supports this interpretation. An active flooding phase during the Iron Age seemingly disagrees with the archeological results, since Iron Age pottery was found in the top of 1Ab, indicating anthropogenic occupation and suggesting less flooding. We propose this is associated with the high elevation of unit 1 (Fig. 3.2). From the early Iron Age (subunit 1BC), higher peak discharges with coarse sediments could

reach the levee. However, the elevated levee was only inundated temporarily, and humans could re-occupy the levee after floods. A recent modeling study (Johnston et al., 2019) supports our explanation. The simulations reveal that small levees are inundated from crest to distal areas as floodwaters spill out of the channel and flow down the levee. On a mature high levee, floodwaters flow around the levee perimeter and inundate the distal levee first, causing the highest deposition rate at the distal part because it is inundated longest with sediment-laden floodwater. This inundation behavior has also been described by (Filgueira-Rivera et al., 2007) for the Columbia River (Canada), where less severe floods preferentially aggrade the distal levee areas, resulting in long periods of inundation and more rapid deposition of the distal levee.

In the Well-Aijen area (Fig. 3.1B), a paleoecological study (Bos and Zuidhoff, 2015) shows that the apparent increase of heather species (which favor nitrogen and phosphate-poor soils) in the Iron Age was the result of over-cultivation and grazing. In the Lomm and Boxmeer areas (Fig. 3.1A), evidence of increased floods during the Iron Age was also found (Zuidhoff and Bos, 2011a, 2011b). In the central part of the Netherlands, a shift to a wetter climate at the start of the Iron Age (~2800 BP) has been demonstrated based on vegetation reconstruction and lake-level changes (Van Geel et al., 1996; Engels et al., 2016; Van den Bos et al., 2018). In the Roman Period and the subsequent mid-late Middle Ages, the Lower Meuse catchment experienced large-scale deforestation, farming, channel regulation and population expansion, resulting in severe soil erosion, increased overbank sedimentation and increased runoff (Fig. 3.8; De Moor et al., 2008; Ward et al., 2009). These human factors, coupled with the wet and warm summers (Büntgen et al., 2011) during the late Holocene, together contributed to the increased flooding intensity and coarse sediment deposition. The erosion surface during the Iron Age (Fig. 3.2), and the significant increase of the sedimentation rate, indicate the human-induced changes dominate over the climate factor in the late Holocene.

3.5.3. Applicability of Ooijen levee sediments in paleoflood reconstruction

The focus of this study is to explore the potential of using levee deposits in paleoflood reconstruction, instead of studying the factors that determine levee formation and evolution. However, we are aware that levee development can also affect the relation of floods with deposition. For instance, changes in channel dimension and discharge, lateral channel migration, changes in sediment supply, changes in flood basin configuration (connection between channel and floodplain) and bed forms may all affect levee deposition (e.g., Törnqvist and Bridge, 2002; Adams et al., 2004; Pierik et al., 2017). Therefore, using sedimentary archives from levees for paleoflood studies is not straightforward because levee growth is conventionally regarded as a dynamic process, leading to a lower sediment preservation potential than floodplain and lacustrine sediments. For instance, in the Roer Valley Graben in the Lower Meuse catchment, the Holocene Meuse River shows highly sinuous channels and active lateral migration; therefore, it is impractical to conduct paleoflood reconstruction from such levee sediments because the levees are young and susceptible to channel migration. In this context, levee deposition is

not the first choice in a paleohydrological study if other more suitable fluvial archives are available. However, the Ooijen levee demonstrates advantages related to the well-preserved stratigraphy, limited Holocene channel migration and good archaeological dating control. In addition, gradual channel downcutting during the Holocene is unlikely to have influenced the grain size record. The elevation of the top of the point-bar and channel sands below the levee does not show an incisional trend towards the present-day Meuse River. Downcutting behavior of the Lower Meuse was more notable during the climate transition from the Late Glacial to the Holocene (Kasse et al., 1995; Tebbens et al., 1999). In addition, the relative subsidence of the Venlo Block (Van Balen et al., 2005) and gradually increased sediment input from the Meuse catchment in the middle to late Holocene (Ward et al., 2009) do not favor river incision. The archeological results were used to constrain the stratigraphic age in this study. The archaeological finds of several cultural periods are in a vertically stacked sequence and mixing of artefacts from different periods in one unit was hardly observed (no palimpsest horizons). We are aware of the potential existence of erosive or non-depositional surfaces during levee formation. It is possible that decadal hiatuses are present. However, the stacked archeological findings (from early Mesolithic to the Middle Ages) clearly indicate that deposition was continuous on a centennial to millennial scale. Based on these considerations, aided with the archeological investigations and vegetation development studies, the Ooijen site is regarded to contain a reliable flooding record.

Peng et al. (2019) analyzed the Holocene paleoflooding history of the Lower Meuse in a floodplain setting at Well-Aijen (Fig. 3.1B). The flooding reconstruction results are shown in Fig. 3.9, alongside the LFEI flooding index record based on the end-member modeling results for the three levee sections at the Ooijen site presented in this study. Comparison of the two independent reconstructions from different settings shows that they agree quite well: both show a gradually weakened flooding regime since the late Mesolithic (Atlantic period) followed by a low sedimentation rate and flooding activity during the Neolithic and Bronze Age (Subboreal period) (Fig. 3.9). An increased dynamic fluvial behavior since the Bronze Age (Subatlantic period) is evidenced by a high sedimentation rate and more severe flooding (Fig. 3.9). This trend was interrupted by short lower flooding phases in the Iron Age and early Middle Ages (Dark Ages). The comparison of the two reconstructions indicates that well-preserved levee deposits can also be used to determine the history of paleoflooding regimes.

3.6. Conclusion

We applied grain size analyses, end-member modeling, magnetic susceptibility and thermogravimetric analyses to a sedimentary record on a levee to infer flooding intensities, and combined it with archeological evidence, to arrive at a Holocene paleoflooding history of the Lower Meuse in the Netherlands. The flooding intensity changes are a combined result of human land-use change (deforestation and agriculture) and climatic changes (precipitation) and the land-use change also caused variation in sedimentation rates, which indicates that the human-induced changes dominate over the climate since the Iron Age. Starting from the middle Mesolithic, the results reveal a gradually decreasing

and low flooding regime in the Mesolithic, during which the young levee was low. In this period, humans began to occupy the levee but the anthropogenic influence on the landscape in the Lower Meuse valley was still low. The appearance of humans on the levee agrees with the inferred reduced flooding intensity. Subsequently, the Neolithic and Bronze Age periods experienced a low, but gradually increasing flooding regime. The Iron Age witnessed the start of a period of enhanced flooding with the deposition of coarser sediments. Intense flooding conditions lasted through the Roman Period until the early Middle Ages (Dark Ages), during which the Lower Meuse experienced a phase of weakened flooding intensity. From the middle to the late Middle Ages, the flooding conditions intensified again. We propose that the coarsening-upward trend and high accumulation rates since the Iron Age resulted from increased flooding and high sediment supply caused by human interference in the Meuse catchment.

Former investigations revealed that the SE part of the levee had little sedimentation in the last seven thousand years, whereas more recent archeological investigations showed that the NW part of the levee has preserved a continuous sedimentary record from the Mesolithic onwards. This different depositional history between two sites on the same levee can be attributed to the channel evolution and elevation difference. This indicates that morphological pre-investigations are critical for determining the optimal location for stratigraphic and sedimentological paleoflood investigations in a levee setting.

The general findings of this study agree well with a paleoflood reconstruction for the Lower Meuse valley ~9 km downstream, which was based on the grain size characteristics of fine-grained, suspended-load dominated lake and floodplain sediments. This implies that well-preserved levee sediments, along stable channel courses, can be a suitable candidate for paleohydrological studies.

4. Rapid flood intensification and environmental response of the Lower Meuse during the Allerød-Younger Dryas climate oscillation

Fei Peng, Ronald van Balen, Christiaan Beets, Cornelis Kasse, Maarten Prins, Nathalie Van der Putten, Simon Troelstra, Hessel Woolderink, John Van der Woude. Submitted to Geomorphology.

Abstract

Lateglacial climatic oscillations exerted profound impacts on the Meuse fluvial system. In the Lower Meuse (southern Netherlands), geomorphological studies in the last decades mainly centred on Lateglacial vegetation evolution, channel pattern changes and river terrace formation. Little information has been reported about the paleohydrology and its relation with the local and regional vegetation history and the climate conditions. This study investigates a sediment core that contains flood sediments deposited from the early Allerød up to the middle Holocene. We conducted grain size analyses, thermogravimetric analysis (organic matter and calcium carbonate content), pollen and macrofossil analysis, and determined the oxygen and carbon stable isotope ratios of biogenic carbonate. The chronology of the core is based on AMS 14C dating and pollen biostratigraphical correlation. The pollen and macrofossil studies reveal that the core site was a lake environment during the Allerød and Younger Dryas periods. The Allerød period oxygen isotope record from biogenic carbonate (opercula of the freshwater gastropod Bithynia tentaculata) is believed to have captured the intra-Allerød Cold Period (IACP). Its synchronous variation with the carbon isotope record and calcium carbonate content indicates a dominant evaporative effect on carbonate chemistry of the lake environments at the core site during the warm Allerød period. End-member modelling decomposes the grain-size distributions into two sandy end members (bed load) and two silty-clayey end members (suspended load). In order to highlight the flood signal, two flooding energy indexes (FEI-1 and FEI-2), reflecting the coarseness of the suspended load and bed load, respectively, were constructed. Both indexes show a relatively high flood condition during the IACP, followed by a low flood phase in the Late Allerød and quickly intensified flood conditions at the onset of the Younger Dryas. In the second phase of the Younger Dryas, deposition of sandy aeolian sediments to the core site complicates the paleoflood identification using FEI-2. This study shows a high sensitivity of the hydrological process and sedimentary environment at the Lower Meuse to the regional climate system.

4.1. Introduction

The Lateglacial is characterized by a series of large and abrupt climate shifts which are expressed by warming and cooling alternations. During the transition from Greenland Interstadial-1 (Bølling-Allerød) to Greenland Stadial-1 (Younger Dryas) occurring at ~12.9 ka Cal BP (e.g., Rasmussen et al., 2006; Clark et al., 2012; Rasmussen et al., 2014), climatic oscillations have induced important impacts on the

global ecological environment and hydrological processes. Therefore, the Lateglacial period is regarded as a time period suitable to study the effects of rapid climatic changes on paleohydrological processes. In the southern Netherlands, the Meuse river experienced a series of river morphological changes from the Lateglacial to the Holocene (Vandenberghe et al., 1994; Kasse et al., 1995; Tebbens et al., 1999; Woolderink et al., 2018). The general consensus is that the river changed from a multi-channel low-sinuosity system in the Bølling to a high-sinuous pattern during the Allerød, and this was followed by a braided river system in the Younger Dryas cold period. From the Holocene onwards, the Meuse became a single-channel with a meandering style again.

For the Holocene time period, Peng et al. (2019), Peng et al. (2020) and Toonen et al. (2015a) respectively reconstructed paleofloods for the Lower Meuse and Lower Rhine by analyzing fluvial sediment records preserved in various sedimentological settings (levee, floodplain, channel-fills). However, the highly variable Lateglacial fluvial network makes it challenging to find suitable sediment records which allow the study of the different flooding stages in the Lateglacial period, and this further hinders the correlation of the flooding regime with climatic oscillations. This is because the Allerød fluvial terrace has largely been eroded by the wide, braided system in the Younger Dryas, and to a minor extent also by the Holocene Meuse river. To further extend the paleoflooding history to the Lateglacial and to understand its sensitivity to rapid climate change, we analyzed a sediment core from a small fluvial lake which formed as a result of channel neck cut-off during the early Allerød (Van Leeuwen, 2014). Multiple proxy-analyses were applied, including grain size, organic matter and calcium carbonate content, pollen, macro fossils and oxygen and carbon isotopes from biogenic carbonate. End-member modelling analysis was applied to decompose the grain-size distribution dataset in a number of representative sedimentary components reflecting suspended load and bed load. The record was chronologically constrained through AMS ^{14}C dating and pollen-based biostratigraphical correlation to the established regional pollen assemblage zones (Hoek, 1997). Below, we first show the lithological characteristics and grain size results, followed by local pollen and macro fossil zone subdivision. Second, we discuss the Lateglacial vegetation history in the Lower Meuse catchment, supported by our new pollen data. In addition, the local pollen zone subdivision is correlated to the regional established pollen assemblage zones to obtain the biostratigraphical information. Then, we study the Lateglacial paleofloods of the Lower Meuse, using the grain-size end-member modelling method, assisted by the other analyzed sedimentary parameters. Finally, we study the linkage of the flooding conditions and sedimentological processes with the regional and local climate changes.

4.2. Geological setting and Lateglacial river evolution

The ~925 km long Meuse river has a catchment covering 33,000 km^2, and flows through north-eastern France, Belgium and the southern part of the Netherlands (Fig. 4.1A). In Nijmegen, it turns to the west

before flowing into the North Sea (Fig. 4.1A). In the south-eastern part of the Netherlands, the Meuse

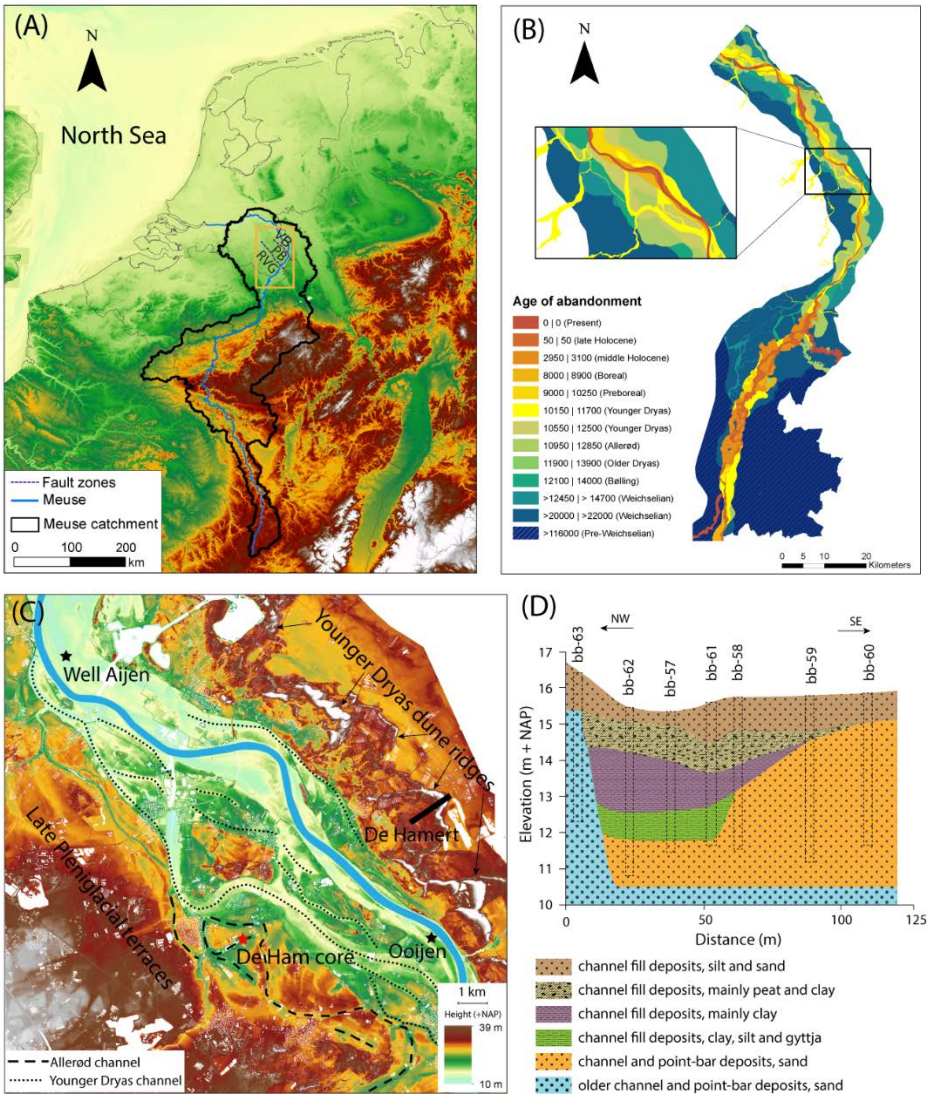

Figure 4.1. (A) Digital elevation map showing the Meuse catchment. The square frames the Lower Meuse detailed in (B). RVG = Roer Valley Graben; PB = Peel Block; VB = Venlo Block. (B) River terraces map of the Lower Meuse catchment (after Woolderink et al, 2018). The present Meuse shows a meandering shape in the study area. (C) Enlarged digital elevation map of the study area. The Well-Aijen (floodplain) and Ooijen (levee) sites are investigated in previous studies for Holocene paleoflood reconstructions. De Ham core is located in an Allerød paleochannel which is situated between the present floodplain and the late Pleniglacial terrace. The red star indicates the De Ham core site and the location of the cross section shown in (D). Younger Dryas parabolic dune ridges are located at the east side of the Meuse channel. The black bar shows the sampling transect across the aeolian dunes at De Hamert. (D) Coring transect at the De Ham paleochannel (after Van Leeuwen, 2014). The legend and colours are also used in figures 2 and 5 for core lithology. The De Ham core is situated at bb-62.

flows through the Roer Valley Rift System which consists of the relatively subsiding Roer Valley Graben, uplifting Peel Block and subsiding Venlo Block (Fig. 4.1A). In the Roer Valley Graben, the Holocene Meuse floodplain is about 3.5 km wide and well-developed due to the sinuous channel. On the Peel Block, the Holocene floodplain is very narrow (~500 m wide) along a relatively straight and incised channel. On the Venlo Block, the floodplain gradually widens towards the Rhine–Meuse delta.

During the last decades, the paleochannels and river terraces on the Venlo Block have been extensively investigated (Fig. 4.1B). In the studied part of the Meuse valley, the morphology is characterized by a series of river terraces which formed due to incision during the Lateglacial period (Kasse et al., 1995; Woolderink et al., 2018). At the start of the Late Glacial, during the Bølling interstadial period (14.7-14.1 ka cal BP), temperature and precipitation increased and the braided river system gradually changed into a low-sinuosity meandering system (Fig. 4.1B) which coincided with a phase of incision. This transitional system eventually evolved into a high-sinuosity meandering system in the following Allerød interstadial period (14.1-12.9 ka cal BP). However, the exact timing of this change is unclear. According to pollen data obtained from the infill of abandoned meander loops, the Meuse started to meander at the start of the Allerød period (Vandenberghe et al., 1994; Kasse et al., 1995; Hoek, 1997). However, bulk ^{14}C data suggest that the meandering system was already active during the Bølling period (Tebbens et al., 1999). During Allerød, the lateral channel migration sediments accreted on the channel point-bar forming up to 7.5-m-thick fining-upward sequences (Van Huissteden and Kasse, 2001). The warm Allerød interstadial is followed by the relatively cold Younger Dryas stadial period, during which the Meuse changed to a braided system (Fig. 4.1B). As a consequence, many of the pre-developed sinuous channels were eroded and only remnant scars are visible at present. Incision of the Lower Meuse during the late Younger Dryas resulted in aeolian deflation of sediment from terrace remnants and (seasonally) exposed river bars, forming parabolic aeolian dunes on the eastern banks of the river (Fig. 4.1C) (Bohncke et al., 1993; Kasse et al., 1995). At the transition to the warm Holocene, the braided river system could not continue to exist due to the combined effect of the rapid temperature increase, the decrease in peak discharge and the vegetation recovery. At the start of the Holocene, local permafrost disappeared and the increase of the infiltration capacity of the soil led to lower peak discharges and a higher base flow compared to the Younger Dryas (Van Huissteden and Kasse, 2001). Because of the rapid reforestation during the early Holocene, the sediment supply decreased again and the Meuse river started to incise. This response of vegetation was much faster than at the Late Pleniglacial to the Bølling / Allerød transition.

The study site, De Ham, is located in between previously investigated sites (Fig. 4.1C, Well-Aijen and Ooijen), where we obtained floodplain and levee sediments, respectively, to reconstruct Holocene flooding stages (Peng et al., 2019; Peng et al., 2020). The De Ham site is located a bit further from the Meuse channel and closer to the Late Pleniglacial terrace (Fig. 4.1C). The core site is located in an abandoned Lateglacial meander. The complete sinuous shape of the paleochannel is still visible (Fig. 4.1C). A previous investigation showed that the investigated channel was abandoned in the early Allerød (Van Leeuwen, 2014). After neck cut-off, the paleochannel acted as an isolated fluvial lake. A transect of seven cores with depth of 4-5 m was drilled and six sedimentary units were determined (Van Leeuwen, 2014), mainly based on differences in lithology (Fig. 4.1D). From the base to the top, the paleochannel infill consists of older sandy terrace deposits (possibly formed in the Bølling period),

followed by organic-rich clayey-silty deposits and silty-sandy channel infillings in the upper part (Fig. 4.1D).

4.3. Material and methods

4.3.1. Coring description and sampling

The De Ham core was hand-drilled with a gouge in January, 2019. The core reached a depth of ~4.2 m. The core was wrapped, and transported to the VU Amsterdam and stored in a cold room at 4 °C. The core contains a 40-cm coarse sequence in the base, followed by a 70-cm, dark coloured, organic-rich interval. Above this is a 190-cm detrital interval with little organic matter, showing a grey and brown colour (among this interval a ~35-cm sand layer was not retrieved in the field). At the top is a ~10-cm peat layer without clastic material (Fig. 4.2a). In order to obtain a complete sedimentary record, we continuously sampled the core at a 2-cm resolution for grain size and thermogravimetric analysis, resulting in 148 samples. In addition, we collected 28 samples for pollen analysis and 15 samples for macrofossil analysis distributed throughout the core. Another 20 samples collected from the 380-290 cm depth interval have been used for oxygen ($\delta^{18}O$) and carbon isotope ($\delta^{13}C$) analysis of opercula biogenic carbonate. In order to allow for differentiation between sandy fluvial and Younger Dryas aeolian influx in the De Ham core, the De Hamert dune formed in the Younger Dryas (Teunissen, 1983; Bohncke et al., 1993) on the eastern river bank (Fig. 4.1C) was chosen for sampling. This is because of its proximity to the De Ham core site and its good preservation as evidenced by the parabolic dune morphology (Fig. 4.1C) and the well-preserved Holocene podzol soil in the top of the dune system.

4.3.2. Grain size analysis and end-member modelling

The method described by Konert and Vandenberghe (1997) was used for sample preparation prior to grain size analysis. For each sample, 10 ml 30% H_2O_2 and 5ml 10% HCl was used to remove organic matter and calcium carbonates, respectively. After pretreatment, grain-size distributions (GSDs), ranging between 0.1 and 2000 μm were measured with a Sympatec HELOS KR laser-diffraction instrument at the VU Amsterdam.

We used end-member modelling to decompose the GSDs dataset into a series of end members. End-member modelling is a useful tool to infer causes of variability in grain size over time and/or space. This can further help infer provenance and geological processes such as dominant mode of erosion, transport and deposition (Prins et al., 2007; Van Hateren et al., 2018). Here, we applied the AnalySize end-member modelling package (Paterson and Heslop, 2015) to the GSDs dataset to obtain the end members. The class-wise r^2 was used to determine the minimum number of end members needed to adequately describe the GSD dataset (Prins and Weltje, 1999; Van Hateren et al., 2018). The end members are used to distinguish bed load versus suspended load subpopulations, which enables the identification of various sub-facies and sedimentary processes.

4.3.3. Thermogravimetric analysis (TGA)

Thermogravimetric analysis is used to obtain the total organic matter (TOM) content and calcium carbonate content (expressed as loss-on-ignition (LOI)) for each sample (Heiri et al., 2001). The analysis is performed on a Leco TGA701 analyser at VU Amsterdam. The mass loss was obtained in a process of stepwise heating from room temperature to 1000 °C. LOI550 (loss-on-ignition at temperature 550 °C) is used to determine the TOM content, and the LOI1000 (loss-on-ignition at temperature 1000 °C) represents the calcium carbonate content.

4.3.4. Stable isotope analyses

Opercula of the freshwater gastropod *Bithynia tentaculata* were chosen for stable oxygen and carbon isotope analyses in this study. Samples were wet-sieved to remove fine clastic material by using a 63 µm sieve, and the residuals were dried overnight on a 60 °C drying plate. Then the opercula were picked under the stereomicroscope. Since a single operculum represents a time-span of 1-1.5 years, they were homogenized before analysis. The stable $\delta^{13}C$ and $\delta^{18}O$ isotope ratios of the samples were analyzed on a Finnigan MAT 253 Isotope Ratio Mass Spectrometer equipped with Thermo Finnigan Gasbench II at the VU Amsterdam. This apparatus measures the isotopes of CO_2, which is generated by adding few drops of water-free phosphoric acid (100 % H_3PO_4) to the samples at a temperature of 45° C in a clean vial flushed with Helium. The internationally used standard IAEA-603 is measured as a control standard (n=10). The long-term reproducibility for this standard is < 0.12‰ and < 0.15 ‰ for $\delta^{13}C$ and $\delta^{18}O$, respectively.

4.3.5. Pollen and macrofossils analysis

Palynological samples were prepared following the standard methods by Faegri et al. (1989) and Moore et al. (1991). After processing, the residues were mounted on a slide in glycerin for pollen identification and counting at 630x magnification. The pollen taxa include trees, shrubs, upland and wetland herbs and aquatics. The percentage pollen diagram was made using the Tilia software package (Grimm, 1992, 2004).

Fifteen samples for macrofossil analysis were heated in a 5% KOH solution near boiling point for 10-15 minutes and subsequently washed through a 150 µm mesh sieve. The sample material was systematically examined at 15-40x magnification, using a stereomicroscope. Seeds, fruits, leaves and other remains of interest were picked and determined. Macrofossil finds are presented as presence/absence data. The diagram was constructed using the Tilia software package (Grimm, 1992, 2004).

4.3.6. AMS ^{14}C dating and age model

AMS ^{14}C dating was performed at Beta Analytic testing laboratory, Miami (USA). Seeds from different terrestrial species and wood pieces were selected for ^{14}C dating (Table 4.1). Because the amount of

datable material in the 2-cm interval samples was limited, seeds from several adjoining samples were combined to meet the (least required mass) requirements for AMS dating (Table 4.1). In addition to AMS dating, additional age-control points were derived from the pollen data through correlation with the regional pollen biochronostratigraphy. In the Netherlands, vegetation history has been well studied for both the Lateglacial and Holocene (Bohncke et al., 1987; Van Geel et al., 1989; Hoek, 1997; Hoek and Bohncke, 2002; Hoek et al., 2017). These results provide a solid reference for biostratigraphic correlation. The pollen assemblage zones in this study were correlated to established regional pollen zones (see Table 2 in Hoek, 1997), which were compiled on the basis of over 250 palynologically investigated sites relating to the Lateglacial period. In the end, all chronological information was integrated to construct the age-depth model of the De Ham core (see Section 4.3.2).

Table 4.1. AMS ^{14}C dating results and calibrated ages with 2σ standard deviation.

lab code	depth (cm)	^{14}C ages (year BP)	cal. range (year BP)	cal. median (year BP)	dated materials
Beta-535687	204-200	10220±30	12095-11775	11939	*Betula* seeds
Beta-535686	320-310	10950±40	12929-12710	12788	Seeds of *Betula*, *Filipendula*, *Carex*, *Apiaceae*, *Heracleum*
Beta-535685	376-374	11380±40	13306-13124	13221	Wood fragment
Beta-535684	390-374	11160±40	13112-12922	13042	Leaf fragments and seeds of *Betula*, *Filipendula* and *Carex*

4.4. Results

4.4.1. Sedimentary characteristics, grain size, TGA and isotope results

Based on the integrated sedimentary results, including core lithology (which is related to sedimentary facies), median grain size, grain-size distribution, organic matter and carbonate content, we divided the De Ham core into six sedimentary units (SU hereafter).

SU-1 (420-380 cm) - This unit represents the lower part of channel infill, consisting of grey silts and sands with a fining-upward trend. The colour of this interval gradually changes upwards from medium grey to dark grey (Fig. 4.2a). There is no clear lamination in this interval. The median grain size decreases from ~140 μm at the lower part to 17 μm at 380 cm (Fig. 4.2b). Sand is the dominant component near the base of the core, with a clear transition to silt-dominated sediments in the upper half of SU-1 (Fig. 4.2c). The total organic matter (TOM) and calcium carbonate content increase gradually to 5% and 10%, respectively (Fig. 4.2d). The fining-upward trend is reflected in the GSDs, the major mode of which shifted from 100-180 μm to ~50 μm (Fig. 4.3a).

SU-2 (380-310 cm) - This unit is distinguished from SU-1 by its fine-grained grain-size characteristics. The unit consists of laminated silty and clayey sediments, exhibiting a dark colour with embedded organic laminae (Fig. 4.2a). The median grain size has a consistently low value (< 10 μm), except at

355 cm where a ~4-cm thick sandy layer is present with median grain size of 160 µm (Fig. 4.2b). The clay and fine silt proportions increase to the maximum level of 30% and 50% in this unit, respectively (Fig. 4.2c). The TOM and calcium carbonate content increase respectively to 20% and 42% at the dark organic-rich gyttja interval (350-310 cm) (Fig. 4.2d). Through the De Ham core, opercula were only present in the interval between 378-293 cm. $\delta^{18}O$ values of the opercula range from -5.66 to -3.87‰ and $\delta^{13}C$ values range from -9.2 to -6.7‰ (Fig. 4.2e). The most negative excursion of $\delta^{18}O$ (between -5.6‰ and -4.8‰) and $\delta^{13}C$ (between -9.2‰ and -7.5‰) occurs at 380-360 cm. The GSDs have unimodal ranging between 7 and 12 µm except at 355 cm and 357 cm where the modes shifted to 180 µm (Fig. 4.3b).

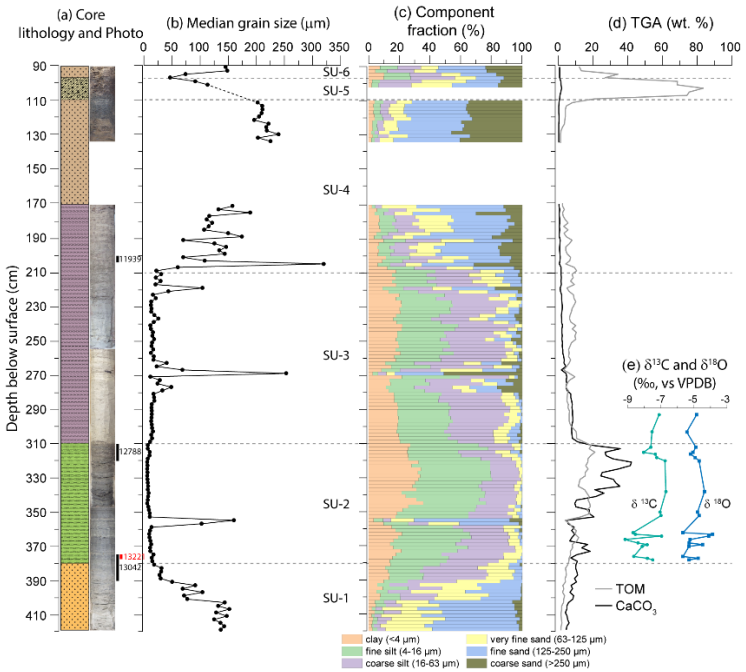

Figure 4.2. Sedimentary results of De Ham core. Dashed lines divide each sedimentary unit (SU). (a) core lithology and photo; vertical bars along the core photo represent the dated interval and calibrated 14C dating results (see Table 1); (b) median grain size; (c) grain size distribution, with size fraction classification cf. Wenthworth (1992); (d) total organic matter (TOM) and calcium carbonate (CaCO3) content; (e) oxygen and carbon isotope variations of the opercula biogenic carbonate.

SU-3 (310-210 cm) – The boundary between SU-2 and SU-3 is characterised by a sharp lithological change. The homogeneous sediments show a grey colour and organic fragments are observed occasionally. The median grain size shows only a slight increase at 310 cm. In the coarser intervals, between 281-261 cm and at 220 cm, the median grain size reaches values of up to 250 µm and 123 µm, respectively (Fig. 4.2b). Clay and silt are the dominant fractions, accounting for ~20% and ~65%, respectively, with the total sand fraction showing considerable variations (Fig. 4.2c). At the transition of SU-2 and SU-3, both the TOM and calcium carbonate content decline abruptly (Fig. 4.2d). The modes of the GSDs vary between 10 and 30 µm, except in the interval of 281-261 cm and at 220 cm, in which the modal size ranges between 200-300 µm and 250 µm, respectively (Fig. 4.3c). The colour

change (from light brown to grey) at 255 cm visible on the photograph (Fig. 2a) is related to the variable light conditions in the field, and does not reflect a real change in sediment colour.

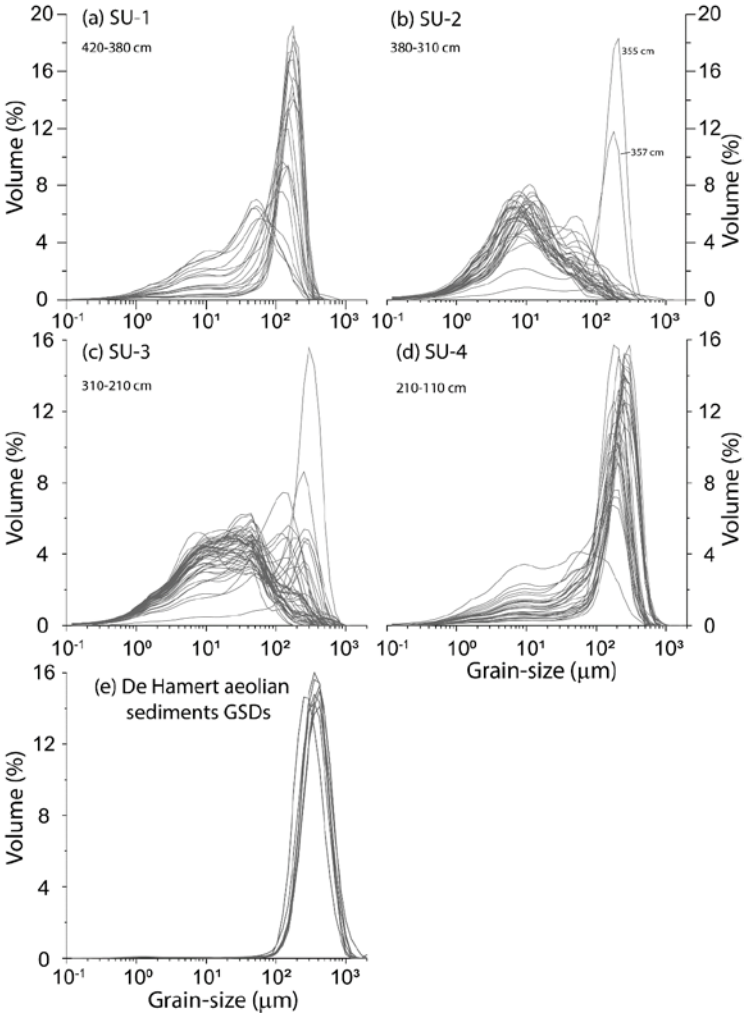

Figure 4.3. Grain size distributions (GSDs) of the sediments in SU 1-4 in De Ham core and De Hamert aeolian sediments. The major mode in SU-1 shifted from 100-180 µm to ~50 µm, representing by the fining-upward trend. In SU-2, the mode range changes to 7-12 µm except at 355-357 cm. In SU-3, the modes of sediments range at 10-30 µm, except in the 281-261 cm and ~220 cm intervals in which the modes range at 200-300 µm and 250 µm, respectively. In SU-4, the GSDs have a bimodal pattern, with a variable coarse mode at 180-300 µm and a minor one at ~10 µm. The aeolian sediments show unimodal pattern with the mode at 250-420 µm.

SU-4 (210-110 cm) - This unit is characterized by its brown coarse-grained, sand-dominated sediments (Fig. 4.2a). The sediments mainly consist of silts and sands, and millimetre-sized coarse sand grains are observed. The grain size of the missing sandy interval is unknown, but it is comparable with its adjacent layer, according to the field notes. The median grain size increases from 26 µm at 210 cm to 250 µm at 130 cm (Fig. 4.2b). The silt fraction gradually reduces upwards to 10%, and the sand component rises to about 80% (Fig. 4.2c). The TOM (<10%) and calcium carbonate content (<5%) reach their lowest values in this unit (Fig. 4.2d). The GSDs show a bimodal pattern in this interval, with a finer mode at ~10 µm and a variable coarse mode at 180-300 µm (Fig. 4.3d).

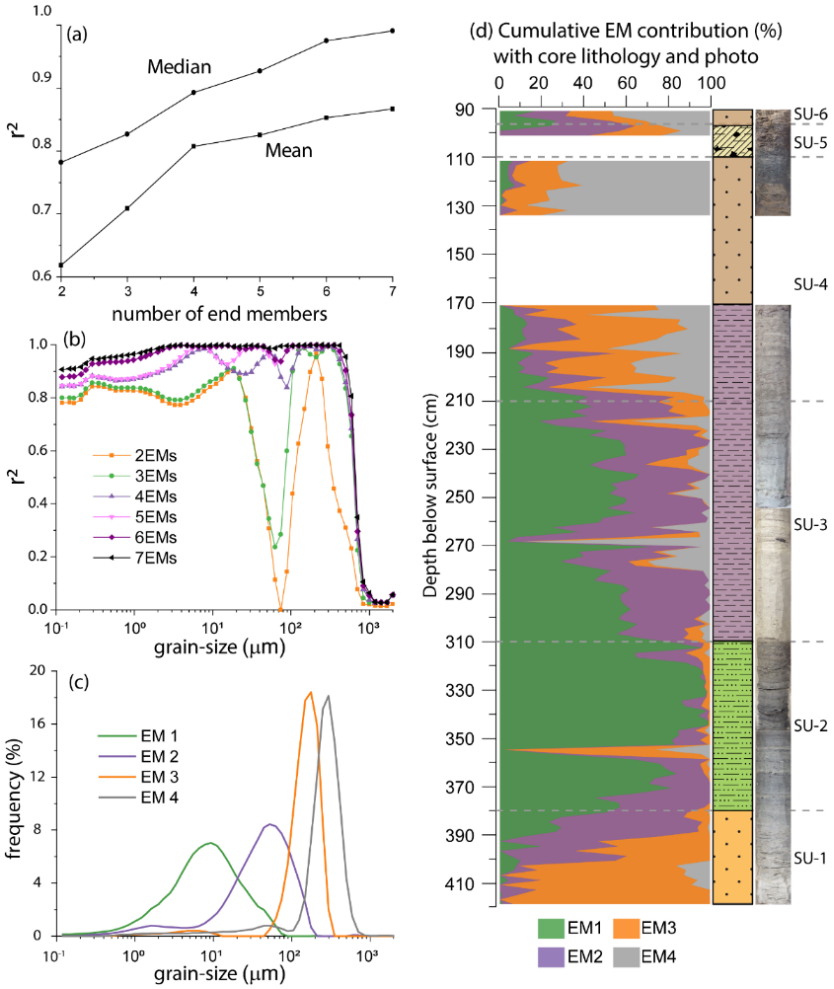

Figure 4.41. End member modelling results. (a) Median and mean r^2 on all grain size classes as a function of the number of end members. A four-end-member model is capable of explaining > 90% of the total variance; (b) r^2 for each size class for end-member models with two to seven end members; (c) the modelled end members according to the four-end-member model; (d) proportional contribution of the EMs of the 4EMM with core lithology and photo.

SU-5 (110-97 cm) - This unit is a peat layer (Fig. 4.2a) and has nearly no clastic grains. The TOM reaches to a maximum of 84% in this interval while the calcium carbonate is low (Fig. 4.2d).

SU-6 (97-90 cm) - This unit consists of silty sands with organic matter content of 10-30 % (Fig. 4.2c, d).

The De Hamert aeolian sediments GSDs exhibit unimodal pattern and have well-defined modes in the range 250-420 µm (Fig. 4.3e). This information will be used as a fingerprint of aeolian sediments (see Section 4.5.2.1).

Figure 4.5. Pollen diagram of the De Ham core. From left to right are core lithology and photo, arboreal pollen (AP including all trees and Humulus, Hedera and Juniperus shrub taxa) and non-arboreal pollen (NAP including the upland herb taxa). The Ericales curve represents Empetrum plus Ericaceae. The diagram is divided into seven pollen zones; numbers in the main AP/NAP diagram above the dashed lines are additional age points derived from Hoek (1997) (see Section 4.4.3.2 and regional pollen zones at right side).

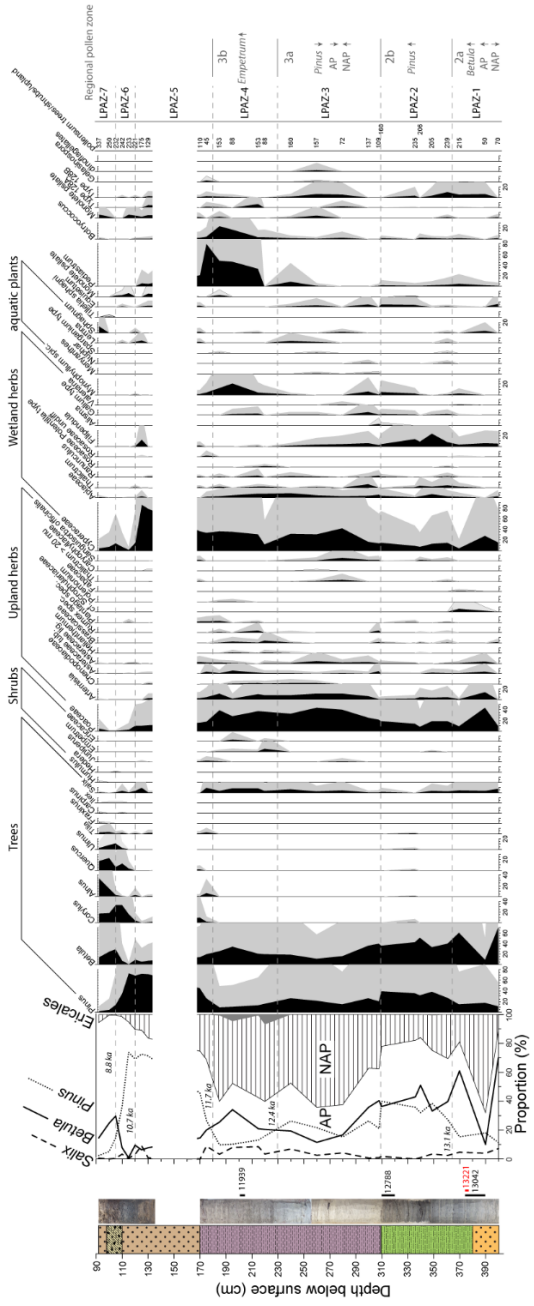

4.4.2. End-member modelling results

The end-member modelling results show that a four-end-member model is capable of reproducing ~90% of the total variance in the GSD dataset (Fig. 4.4a). A three-end-member model performs poorly in the range of 30-80 µm, while a five-end-member model is unable to significantly improve the modelling performance (Fig. 4.4b). To comply with the principle of parsimony (Weltje, 1997; Prins, 1999), the four-end-member model is adopted in this study. The four end members have a unimodal GSD but with different modal sizes. EM1 and EM2 have modes at 9 and 53 µm, respectively (Fig. 4.4c). EM3 and EM4 are considerable coarser-grained than EM1 and EM2, and have modes at 170 and 300 µm, respectively (Fig. 4.4c). The cumulative percentages of the four end members are plotted against core depth in Figure. 4.4d. In SU-1, the EM3 is dominant but it reduces from ~90% at the base to less than 10% at the top (Fig. 4.4d). In the upper part of SU-2, the EM1 proportion increases to 95% in the organic-rich part at the expense of EM2 (Fig. 4.4d). In SU-3, this is followed by a relatively constant proportion of EM1 (~50%) and EM2 (~30%) with fluctuating percentages of EM3 and especially EM4 (Fig. 4.4d). In SU-4, the abrupt coarsening at ~210 cm is reflected by the sharp increase in EM4 and EM3, and the overall coarsening-upwards in this unit lies in the gradual increase in especially EM4 (Fig. 4.4d).

4.4.3. Vegetation development and Biochronostratigraphy

4.4.3.1. Pollen and macrofossil analysis

The pollen diagram is given in Figure 4.5. Arboreal pollen (AP) taxa include all trees and *Humulus*, *Hedera* and *Juniperus* shrub taxa. Of the non-arboreal pollen taxa (NAP) only the upland herb taxa are used in the AP/NAP-ratio, in order to avoid overrepresentation of local wetland (i.e., marsh and aquatic) NAP-taxa. Ericales (*Empetrum* and Ericaceae) have been placed separately in the AP/NAP-ratio diagram. The pollen sum was defined as the sum of all trees, shrubs and the upland herbs. Wetland plants, aquatic plants and algae were excluded as these taxa are of local origin. Based on changes in the pollen assemblages, we divided the diagram into seven local pollen assemblage zones (LPAZ).

LPAZ-1 (400-365 cm) features high *Betula* and low *Pinus* percentages. The NAP taxa have high percentages at the base of LPAZ-1 and decline rapidly upwards (Fig. 4.5).

LPAZ-2 (365-310 cm) shows high *Pinus* and *Betula* percentages while *Salix* declines. The wetland herbs increase and the NAP percentages are low (Fig. 4.5).

In LPAZ-3 (310-230 cm), percentages of AP decrease while those of NAP increase steadily, including taxa such as Poaceae, *Artemisia*, Asteraceae tub. and Asteraceae lig. Most wetland herbs gradually reduce except Cyperaceae (Fig. 4.5).

In LPAZ-4 (230-180 cm), the percentage of *Pinus* slightly declines while *Betula* increases. Open land species like *Empetrum* and Ericaceae appear in this zone, together with upland herbs like Asteraceae, *Helianthemum*, Brassicaceae and *Rumex* (Fig. 4.5). *Polemonium* occurs for the first time in this zone, a subarctic species, indicating an open landscape.

In LPAZ-5 (180-120 cm), the pollen record shows continuity in the species composition, despite the missing/lacking sandy interval (170-135 cm). The pollen diagram shows a decline of *Betula* and a strong increase of *Pinus*. Low percentages of *Corylus*, *Alnus*, *Tilia* are related to soil formation and bioturbation in the top of the sand layer. The amount of Poaceae declines, and a small *Juniperus* peak is observed at the start of LPAZ-5, marking the start of stabilization of the landscape. *Empetrum* and Ericaceae have disappeared.

LPAZ-6 (120-105 cm) has high AP values. The amount of *Pinus*, shrubs and upland herbs declines, and the amounts of *Betula*, *Corylus* and *Quercus* show an increase.

In LPAZ-7 (above 105 cm), the percentages of *Alnus*, *Quercus*, *Ulmus* and *Tilia* have their highest values. The NAP taxa (shrubs and upland herbs) reach their lowest percentages (Fig. 4.5).

Based on a selection of in-lake taxa present in the De Ham core, three macrofossil assemblage zones (MAZ) were distinguished (Fig. 4.6). MAZ-1 (390-310 cm) is characterised by the presence of *Bithynia tentaculata* opercula, *ostracods* and carbonate precipitation (Fig. 4.6). Aquatic plants (macrophytes) such as Nymphaeaceae and *Potamogeton* spp. together with *Cristatella mucedo* (Bryozoa statoblast) are present over the complete MAZ-1. MAZ-1 can be subdivided into two subzones: 1a and 1b, based on the first occurrence of *Gloeotrichia* type and Characeae at 350 cm depth. In the top part of subzone 1b, *Myriophyllum spicatum* and *Hottonia palustris* appear (Fig. 4.6). At the transition to MAZ-2 (310-230 cm), *Gloeotrichia* type, *Myriophyllum spicatum* and *Hottonia palustris* disappear. *Bithynia tentaculata*, *ostracods* and carbonate precipitation, as well as Nymphaeaceae and *Potamogeton* are present until 290 cm and 270 cm depth, respectively. Characeae are present throughout this zone (Fig. 4.6). In MAZ-3 (230-170 cm), *Potamogeton*, *Cristatella mucedo* (Bryozoa statoblast), *Gloeotrichia* type, *Myriophyllum spicatum* and *Hottonia palustris* reappear while Characeae disappear (Fig. 4.6).

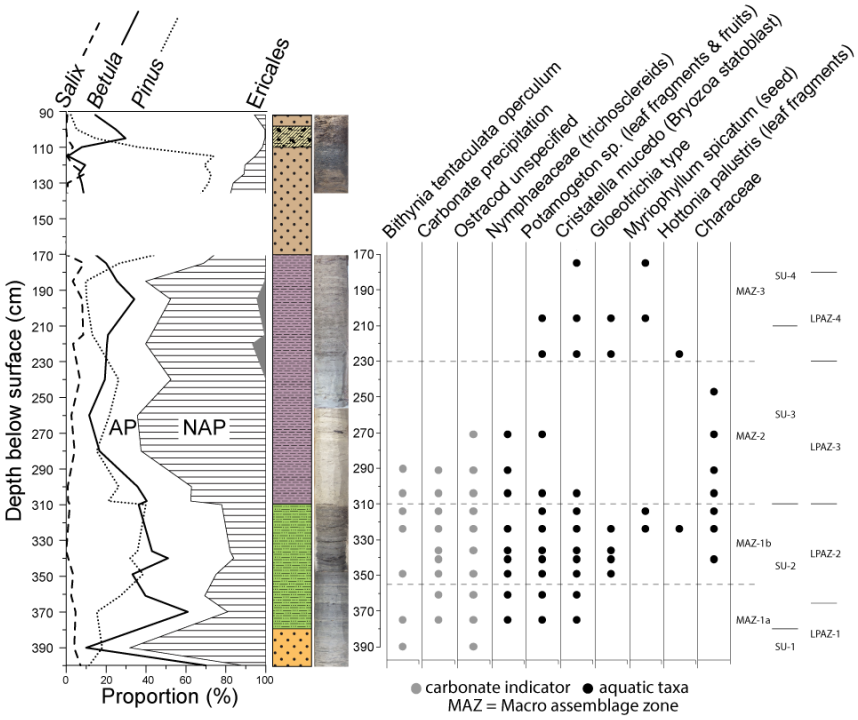

Figure 4.6. Macro fossil diagram of the in-lake taxa (in black) of the De Ham core, expressed as presence/absence. In grey we show the carbonate indicators. Sedimentary units (SU) and local pollen assemblage zones (LPAZ) are shown at right side for comparison.

4.4.3.2. Chronological model-results from biostratigraphic interpretation

The AMS ^{14}C dates were calibrated using the IntCal13 curve (Reimer et al., 2013). The dating results are listed in Table 4.1. AMS ^{14}C dates from 390-374 cm, 376-374 cm, 320-310 cm and 204-200 cm provide ages of *c.* 13.0 ka cal BP and 13.2 ka cal BP, 12.8 ka cal BP and 11.9 ka cal BP, respectively (Table 4.1, Fig. 4.2a). These dates indicate that most of the De Ham core sediments were deposited during the Allerød and Younger Dryas. The aquatic plant and fauna taxa (Fig. 4.5, 4.6), together with the presence of clayey sediments (Fig. 4.2a) show that the core site was a lake environment in the interval 390-170 cm. LPAZ-1 and LPAZ-2 represent regional vegetation conditions during the Allerød, as confirmed by the AMS dating (Fig. 4.5). These pollen zones roughly correspond with MAZ-1a and 1b, respectively (Fig. 4.5, 4.6). The low pollen sum in LPAZ-1 is associated with the nature of the sandy deposits (Fig. 4.2a, c). The increased pollen sum in LPAZ-2 reflects a high preservation capacity and lake level during the late Allerød. MAZ-1a is indicative for shallow fresh-water lakes/ponds. *Myriophyllum spicatum*, *Hottonia palustris*, Characeae and carbonate precipitation are indicators of calcareous water conditions (Streeter et al., 2016).

According to the variation and relative abundance of pollen taxa, LPAZ-1 and LPAZ-2 correspond with zone 2a (Allerød *Betula* phase) and 2b (Allerød *Pinus* phase) of Hoek (1997) (Fig. 4.5). The correlation of the regional pollen diagram with the Greenland GISP2 ice core shows that the transition from zone 2a to 2b occurred at ~13.1 ka cal BP (Hoek, 1997). Considering the AMS ^{14}C dates above and below this LPAZ-1-LPAZ-2 boundary of 12.8 ka cal BP and 13.2 ka cal BP, respectively, it is reasonable to

assume an age of 13.1 ka cal BP for this boundary (Fig. 4.5), and this also indicates that the ^{14}C date from interval 390-374 cm is slightly too young.

Both LPAZ-3 and LPAZ-4 feature reduced AP (*Betula* and *Pinus*) and high NAP (i.e., appearance of *Artemisia* and Asteraceae) while *Empetrum* and Ericaceae only appear in LPAZ-4 (Fig. 4.5). The characteristics of the two zones correspond well with the regional zones 3a and 3b of the Younger Dryas (Hoek, 1997) (Fig. 4.5). The disappearance of *Myriophyllum spicatum* seeds and *Bithynia tentaculata* opercula in MAZ-2 might suggest a temperature decrease, as *Myriophyllum* needs an optimum July temperature of > 10°C, and *Bithynia tentaculata* is frost sensitive (Gittenberger et al., 2004; Gaillard and Birks, 2007). The increased percentages of upland herbs in LPAZ-4 (Fig. 4.5) indicates a more open landscape, i.e., the appearance of *Polemonium* reflects a subarctic environment. In LPAZ-4, the high percentages of wetland herbs and consistent presence of *Myriophyllum* in both the pollen and macrofossil data (Fig. 4.5, 4.6) indicate that the core site was still a lake during the late part of the Younger Dryas. Based on these observations, we argue for a two-phase Younger Dryas climate pattern in the Lower Meuse catchment which is reflected by LPAZ-3 and LPAZ-4. The proposition of a two-phase Younger Dryas has been suggested previously from multiproxy climate data for Western Europe (Isarin et al., 1998; Isarin and Bohncke, 1999; Schenk et al., 2018). In more detail, it is suggested that a relatively cold and humid phase was followed by a dry phase (i.e., Isarin et al., 1998; Muschitiello et al., 2015; Hepp et al., 2019), although an opposite pattern (a drier early Younger Dryas) has also been proposed (i.e., Brauer et al., 1999; Brauer et al., 2008). We adopted an age of 12.4 ka cal BP based on the transition between zones 3a and 3b from Hoek (1997) for the boundary of LPAZ-3 and LPAZ-4 here (Fig. 4.5), and this seemingly agrees well with the AMS ^{14}C dating results of 12.8 ka cal BP at 320-310 cm and 11.9 ka cal BP at 204-200 cm in the De Ham sequence.

The decline of NAP and Ericales and increasing *Pinus* values at the base of LPAZ-5 (Fig. 4.5) mark the onset of the Holocene (Preboreal, 11.7-10.7 ka cal BP). The AP taxa increase at the expense of shrubs and upland herbs (Fig. 4.5), indicating a restoration of the forest. The low values of *Corylus*, *Alnus*, *Querus* and *Tilia* (Fig. 4.5) seem to imply that the lower part of LPAZ-5 corresponds to the Atlantic period, as these taxa are common since the middle Holocene and they are absent in regional pollen diagrams of the early Holocene (cf. Iversen, 1973; Hoek, 1997; Bos et al., 2007; Hoek et al., 2017). However, we interpret these low percentages as the result of soil formation and/or bioturbation (i.e., plant root penetration and burrowing), as was observed during sampling of the sandy interval. Based on these observations, we suggest that the boundary of LPAZ-4 and LPAZ-5 is the transition of the Lateglacial to the Holocene period at *c*. 11.7 ka cal BP (Fig. 4.5), in accordance with Hoek (1997). In LPAZ-6, *Corylus*, *Quercus* and *Ulmus* start to increase, and *Pinus* is decreasing. Shrubs and upland herbs are nearly absent, resulting in high percentages of AP taxa. In addition, the increased pollen sum (Fig. 4.5) implies a dense vegetation cover. This zone corresponds to the Boreal (10.7-8.8 ka cal BP) period in the regional vegetation development (Iversen, 1973). The high values of *Quercus*, *Alnus*, *Tilia*

and *Ulmus*, and low values of *Pinus* and *Betula*, together with the shrubs and herbs observed in LPAZ-7, correspond with Holocene vegetation reconstructions (Kasse et al., 1995; Bos and Zuidhoff, 2015) in the Lower Meuse and also with the NW European pollen zones. Based on this, we interpret the base of LPAZ-7 as the start of the Atlantic period (8.8-5.6 ka cal BP). The obtained time boundaries based on the regional biostratigraphy, together with the AMS ^{14}C dating were used to establish a chronological model of the De Ham core (Fig. 4.7a). Accordingly, the sedimentation rate is calculated based on the age model (Fig. 4.7b).

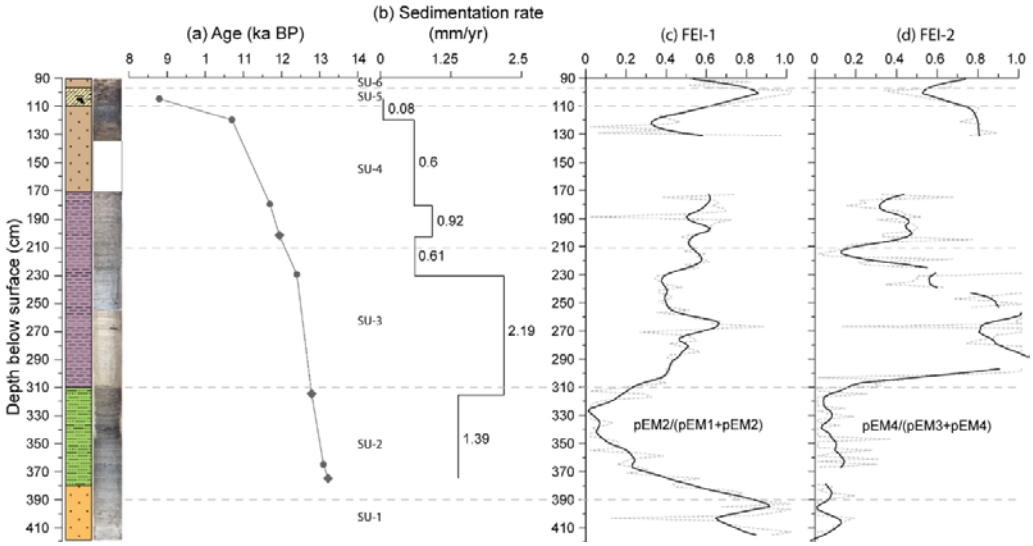

Figure 4.7. (a) Linear age model based on the AMS 14C dating (diamonds) and pollen biostratigraphical correlation (dots); (b) sedimentation rate; (c-d) flood energy indexes calculated after the end member modelling analyses on the grain size dataset. The dotted grey lines are raw data, and solid black lines are processed curves by using a locally estimated scatterplot smoothing method to prevent undue emphasis being placed on single data. The interruptions in (d) indicate where no valid data points are present.

4.5. Discussion

4.5.1. Paleoclimate in the Lower Meuse catchment during the Allerød and Younger Dryas

The core site is situated in an oxbow lake which is close to the active channel (Fig. 4.1C). During the Allerød period, the meandering river more or less flowed at the same height level (no incision) because of a regular discharge (Kasse et al., 1995; Woolderink et al., 2018). These two factors resulted in a high groundwater table and therefore, both flooding water and groundwater were important sources to the shallow lake. In this shallow lake setting, the preserved calcium carbonate content in sediments relies on its precipitation and dissolution rate:

$$Ca^{2+} + 2HCO_3^- \leftrightarrow CaCO_3 + CO_2 + H_2O \qquad \text{(Eq. 4.1)}$$

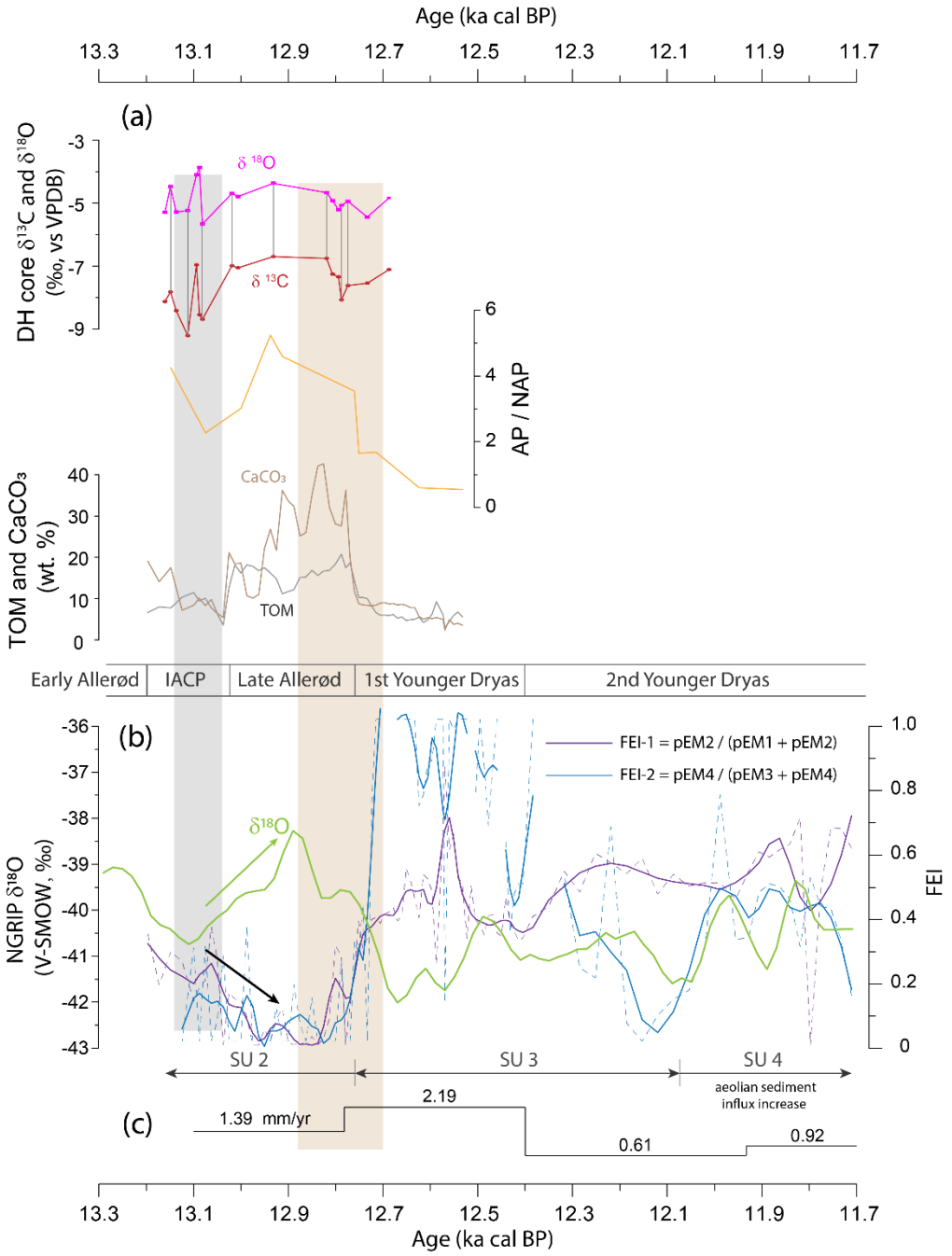

Figure 4.8. De Ham sedimentary record and reconstructed Lateglacial floods at the Allerød and Younger Dryas periods. (a) $\delta^{18}O$ and $\delta^{13}C$ of the opercula biogenic carbonate, AP / NAP, TOM and calcium carbonate content records show apparent variations during the Allerød and the transition to the Younger Dryas; (b) comparison of the two flooding energy indexes and NGRIP ice core 18O records; (c) sedimentation rate. Grey and brown shaded areas show the intra-Allerød Cold Period and Allerød-Younger Dryas transition period, respectively.

The calcium carbonate precipitation is primarily dependent on the bicarbonate content of the groundwater feeding the lake. Assuming a relatively constant bicarbonate content of the ground water, the authigenic carbonates are commonly precipitated by warming and/or photosynthetic utilization of CO_2 resulting in calcium carbonate supersaturation in the water column. In most temperate high-latitude regions authigenic carbonates are precipitated mainly in summer during periods of maximum warming

and phytoplankton productivity. Furthermore, the amount of evaporation has a major influence on the isotope composition of standing water bodies, especially in small-scale lakes (Leng et al., 1999; Teranes and McKenzie, 2001; Leng and Marshall, 2004). In this case, the temporal variation of calcium carbonate content can serve as a proxy of paleo-temperature and lake productivity (Stuiver, 1970; Roberts et al., 2008). *Bithynia tentaculata* is a common freshwater prosobranch gastropod with a life span of one to three years, although growth may stop after the first year (Fretter and Graham, 1976; Graham, 1988). Therefore, analyzing the biogenic carbonates from opercula of *Bithynia tentaculata* can provide years-average $\delta^{18}O$ and $\delta^{13}C$ values that are generally ascribed to variations in temperature and precipitation isotope composition (Leng and Marshall, 2004).

In the Allerød 13.2-12.7 ka cal BP interval, a covariation of calcium carbonate with $\delta^{18}O$ and $\delta^{13}C$ is observed (Fig. 4.8a). The high (low) calcium carbonate content values correspond with heavier (lighter) $\delta^{18}O$ and $\delta^{13}C$. During the Allerød, both photosynthesis and evaporation were higher during the summer than in winter time in this small-scale lake. Stronger photosynthesis promoted the uptake of CO_2 by vegetation that led to carbonate super-saturation in the water column (see Eq. 4.1), and depletion of ^{12}C and enrichment of ^{13}C in the lake because the photosynthetic organisms prefer using ^{12}C in lake water (Meyers and Teranes, 2002). The former resulted in higher calcium carbonate precipitation and the latter explains enrichment of ^{13}C in biogenic carbonate (Fig. 4.8a). Meanwhile, high evaporation in summer caused heavier oxygen isotope left in the lake (Fig. 8a). This explanation indicates a dominant evaporation effect in the lake during the Allerød. The observations imply a dynamic response of the sedimentary environment to the local climate.

The more negative excursion in the $\delta^{18}O$ record and lower TOM and calcium carbonate content in the De Ham core at around 13.1 ka BP corresponds with the intra- Allerød Cold Period, a cold climatic reversal observed in GISP2 ice-cores (Stuiver and Grootes, 2000) (Fig. 4.8b). Warmer climate conditions during the Late Allerød are reflected both in the ice-core oxygen isotope records and by generally high $\delta^{18}O$ and $\delta^{13}C$ values in the De Ham core (Fig. 4.8a, b). The decreased AP/NAP values (indicating a degraded tree cover), TOM and calcium carbonate content (Fig. 4.8a) indicate a fast response of the environment to the climate change at the Allerød-Younger Dryas transition. Overall, the positive correlations between the De Ham core sedimentary proxies and Greenland ice core oxygen isotope records imply a direct link between the Lower Meuse paleoenvironment and North Atlantic climatic oscillations during the Lateglacial.

4.5.2. Floods in the Lower Meuse catchment during the Allerød-Younger Dryas

4.5.2.1. Interpretation of the end-member mixing model

The De Ham core contains sediments that were deposited during the Allerød, Younger Dryas and early to middle Holocene. Previous studies have pointed out important aeolian activity in this area during the Younger Dryas, as a result of a degraded vegetation cover (Kasse et al., 1995; Huisink, 1997; Kasse,

2002; Kolstrup, 2007) and strong and stable westerlies (Renssen et al., 1996; Brauer et al., 2008). Therefore, in addition to flood sediments, aeolian sediments could also have been deposited at the core site. Therefore, a reliable interpretation of the sediment source is vital to reconstruct the Lateglacial flood record of the Lower Meuse.

The grain size information of the De Ham core sediments and the unimodal-pattern of the GSDs of the De Hamert aeolian sediments (Fig. 4.9b) can be used to differentiate aeolian from fluvial sedimentary components in the De Ham core. The distinct grain size distributions of the two fine end members (EM1 and EM2) from the two coarse end members (EM3 and EM4) indicate different deposition processes represented by the two groups. EM1 and EM2 mainly occur in SU2-3, in which the sediment components are dominated by clay and coarse silt (Fig. 4.2c). The total sum of EM1 and EM2 in these two units adds up to more than 85% (Fig. 4.4d). Therefore, we interpret both EM1 and EM2 as suspended load sub-populations. The grain size range of these two end members fall in the range of the suspended load components found at the Well-Aijen and Ooijen sites (Fig. 4.9c, d). Although units SU-2 and SU-3 contain Lateglacial sediments while the latter two sites contain Holocene sediments, the resembling GSDs of the suspended load in the De Ham core and the Well-Aijen floodplain core (Fig. 4.8a, c) imply that the sedimentary processes (sediment source, transport and deposition) have resulted in very similar suspended load components. However, the different shapes of the GSDs of the fine EMs (suspended load) between Well-Aijen and Ooijen (Fig. 4.9c, d) indicate the sedimentary setting (floodplain versus levee) determines suspended load sorting, despite the proximity of the two sites and concurrent sedimentation therein. Similarly, the coarse-grained EM3 and EM4 resemble the coarser EMs from the Well-Aijen and Ooijen sites and also the De Hamert dune sands (Fig. 4.9b-d) and thus can be associated with fluvial bed load deposits or aeolian influx.

The sediments in SU-1 were deposited shortly after channel abandonment, and the dominant EM3 in this unit represents the fluvial bed load component (Fig. 4.4d). Aeolian activity in the Allerød was probably limited because the land surface was largely covered by pine-birch forest and shrubs (Fig. 4.5). The high soil stability reduced aeolian sediment availability. Therefore, the relatively high sedimentation rate of 1.39 mm/yr (Fig. 4.7b) in SU-2 should be the result of flooding. In SU-3, EM1 and EM2 are the major grain size subpopulations, and only spikes of EM3 and EM4 occur (Fig. 4.4d). The fine-grained sediments in this unit cannot be related to aeolian-dominated sedimentation. The disappearance of *Cristatella mucedo* (Bryozoa statoblast), *Myriophyllum spicatum*, *Hottonia palustris* in MAZ-2 of SU-3 might be due to an increased turbidity of the lake water, e.g. a higher suspended sediment load, related to higher peak discharges and increased flooding. Reduced soil water storage capacity, development of permafrost and more snow accumulation in the colder winters during the Younger Dryas favoured a higher peak discharge and severe flooding during spring (Kasse et al., 1995), and this could explain the spikes in the EM4 record in SU-3 (with mode at 300 μm) (Fig. 4.4d). We conclude that the sediments in SU-3 were derived mainly from floods. In SU-4, the sediments are much

coarser, with high proportions of EM3 and EM4 (Fig. 4.4d). At 210-170 cm, EM4 shows a background value (the minimum level) of 15% and the EM3 proportion is ~40% (Fig. 4.4d). In the context of a gradually infilled abandoned channel, more open vegetation conditions (Fig. 4.5), reduced soil water capacity and enhanced westerlies and higher peak discharge (Kasse et al., 1995; Renssen et al., 1996; Brauer et al., 2008), we suggest that the coarse sediment at 210-170 cm includes both flood and aeolian sandy sediments. In addition, the contribution from aeolian activity probably became dominant starting from the base of SU-4 (at ~207 cm). The dominance of EM4 above 134 cm cannot be related to aeolian input, because during the Holocene vegetation recovered and aeolian activity was largely reduced in the Lower Meuse during the Holocene. Sediment reworking or a more local fluvial process should be responsible for deposition of these sandy sediments.

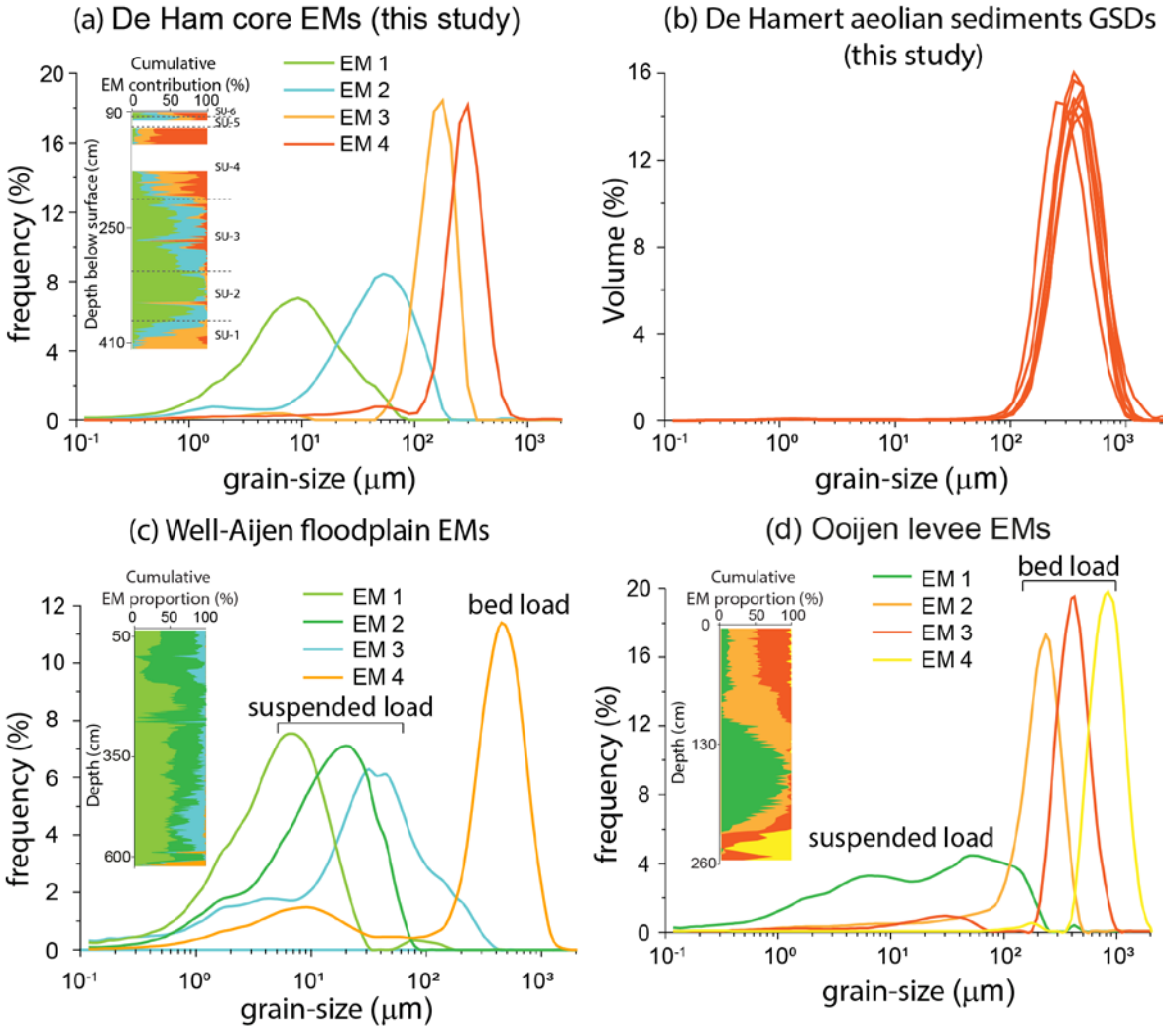

Figure 4.9. The modelled end members from the De Ham site (this study) and from the Well-Aijen and Ooijen sites (after Peng et al., 2019 and Peng et al., 2020, respectively). End member modelling is not performed on the De Hamert aeolian sediment GSDs because of the small sample number and the uniform grain-size distributions.

4.5.2.2. Lateglacial flood reconstruction for the Lower Meuse

Previous Holocene paleoflooding reconstructions for the Lower Meuse based on Well-Aijen floodplain and Ooijen levee sediments (Fig. 4.1C) relied on highlighting the coarse components among fine and coarse end members (Peng et al., 2019; Peng et al., 2020). Sediments from the De Ham core are composed of very similar fine and coarse components (Fig. 4.2b, c). In the fluvial sediment-dominated interval (420-207 cm), EM1 and EM2 can be interpreted as suspended load components and EM3 and EM4 as bed load components. This interpretation conforms to the mixing model proposed by Erkens et al. (2013) for the lower Rhine catchment, and to Peng et al. (2019) and Peng et al. (2020) for the Meuse catchment. Based on the principles of the latter two studies, we construct two indexes that independently highlight the coarse components within the suspended load fraction (EM1 and EM2) and the bed load fraction (EM3 and EM4). The key function of defining these two indexes is that they, independently from each other, amplify the flooding signal contained within the suspended load and bed load sediment fractions. The two indexes are expressed as:

$$\text{FEI-1} = \frac{pEM2}{(pEM1+pEM2)} \qquad \text{(Eq. 4.2)}$$

$$\text{FEI-2} = \frac{pEM4}{(pEM3+pEM4)} \qquad \text{(Eq. 4.3)}$$

Where pEMx indicates the proportion of EMx. We apply the two indexes to the end member modelling results. A locally estimated scatterplot smoothing (LOESS) method is applied to the results of the two indexes to prevent undue emphasis being placed on single data points (Fig. 4.7c, d). From SU-1 to SU-2, FEI-1 decreases steadily while FEI-2 is consistently low. The decreasing FEI-1 conforms to the fining-upward trend (Fig. 4.2b). Both indexes increase quickly from SU-2 to SU-3. Within SU-3 only FEI-2 starts to reduce. In the upper three units, both the indexes maintain a relatively high value (~0.6) with fluctuations (Fig. 4.7c, d).

Figure 4.8 presents the time series of the two indexes, the sedimentation rate, the AP/NAP values, the TOM and the calcium carbonate content based on the De Ham age model presented in Figure 4.7. The variations of the two indexes are also compared with the NGRIP ice core $\delta^{18}O$ (Fig. 4.8b). Both indexes show higher flood conditions during the IACP than that in the Late Allerød, whereas the Greenland ice core $\delta^{18}O$ shows an anti-phase variation (Fig. 4.8b). At the Allerød-Younger Dryas transition, the Lower Meuse experienced quickly intensified flooding and a high sedimentation rate (Fig. 4.8b, c), and these hydrological changes co-varied with the rapidly declined $\delta^{18}O$ in Greenland ice core. During the IACP a temporary period of wet conditions at the Lower Meuse Valley was also reported by Bohncke et al. (1993) and Hoek (1997). A simultaneous decline in winter temperature allowed for more intense freeze-thaw incidences which reduced soil infiltration capacity and, therefore, increased run-off and peak discharges during the spring time. This explanation also applies to the intensified floods at the start of Younger Dryas. The presence of initial ice-wedge casts and other periglacial features at the start of Younger Dryas point to the permafrost conditions and a mean annual temperature between -2 and -5°C,

and this could further induce more frequent and higher floods. In the first stage of the Younger Dryas, both indexes show consistently high flooding conditions (Fig. 4.8b), whereas a discrepancy of the two indexes is observed in the second stage of the Younger Dryas (Fig. 4.8b), during which the consistently high floods indicated by FEI-1 index are not observed in the FEI-2 index. This disagreement can be explained by the influx of coarse aeolian sediments during the second phase of the Younger Dryas. The aeolian activity altered the dominant sediment source for the De Ham core and blurred the flooding signal stored in the fluvial bed load sediments. In addition, during this period, the Meuse continuously incised and migrated to the east (Fig. 4.1C) (Kasse et al., 1995). Therefore, the core site was less prone to be inundated by floods, which explains the higher FEI-1 but lower sedimentation rate in the second phase of Younger Dryas compared to the Allerød period.

The observations above have two main implications. Firstly, our results show that the Lower Meuse hydrological regime is very sensitive to and abruptly responded to the North Atlantic regional climate shifts during the last deglaciation. Secondly, it indicates that well-preserved Lateglacial flood-induced sediment records can be used to reconstruct past flooding stages by applying the end-member modelling approach. However, it should be stated that the obtained results following such an approach is highly dependent on the sedimentological setting of the studied sedimentary sequence. For example, in specific fluvial environments only background fine suspended load sediments (i.e., in distal floodplain environments with low energy floods) or coarse bed load components (i.e., at levee sites that receive high-energy deposition) are available for sampling, and the flooding indicators (such as sand layers, lithology changes, sedimentary texture and structure changes, interbedded palaeosols) can hardly be observed from the relatively homogenous deposits. Here, we show that the flooding stage signal is reflected by highlighting the coarse grained end members in the sediment fill of an abandoned channel, in accordance with the previous Holocene paleoflooding reconstructions (Peng et al., 2019; Peng et al., 2020), in which the flooding stages were reconstructed by analyzing the fine and coarse sediments from floodplain and levee environments, respectively.

4.6. Conclusion

The De Ham core from the Lower Meuse provides a well-preserved fluvial sediment record covering the Allerød up to the middle Holocene. The present study mainly focuses on the Allerød-Younger Dryas part of the record. The fine sediment characteristics, abundant aquatic plant and fauna taxa indicate a lake environment. Laboratory analyses provided AMS ^{14}C dating, grain size, oxygen and carbon isotopes of opercula biogenic carbonate, organic matter content, calcium carbonate content, pollen- and macrofossil-based vegetation and environmental reconstruction for the core.

In the Allerød, the sediments have a high organic matter content, sediments are fine-grained (clay) and accumulation rates are relatively high. The local landscape was characterized by high arboreal coverage. The macrofossil abundance reached their highest levels. The correlations between the calcium carbonate content and $\delta^{18}O$ and $\delta^{13}C$ variations indicate a high evaporative effect on carbonate

chemistry of the lake environments during the Allerød period. Meanwhile, the intra-Allerød Cold Period is also recorded by the $\delta^{18}O$ of opercula biogenic carbonate in the De Ham core. Sediments deposited in the Younger Dryas have lower organic matter and calcium carbonate content, and sediments gradually coarsen because of an increased influx of coarse silts and (partly aeolian) sands. Sedimentation rate is the highest in the first stage of the Younger Dryas. Compared to the preceding period, AP taxa are less prominent and pollen sum and number of macrofossil species are reduced. Subsequently, the appearance of Ericales and more upland herbs in the second stage of the Younger Dryas imply a further opening of the vegetation cover. The aeolian influx increased, likely as a result of strong westerlies and more open vegetation conditions.

Two flood energy indexes, FEI-1 and FEI-2, are constructed based on the grain size end members. FEI-1 uses the suspended load end-members, whereas FEI-2 is based on the bed load end-members. Both indexes show relatively high flood conditions during the IACP, followed by a low flood stage in the Late Allerød and quickly intensified flood conditions at the onset of the Younger Dryas. This study firstly revealed the high sensitivity of the local hydrological processes and sedimentary environments in the Lower Meuse catchment to the regional climate system. However, the flooding signal can be disturbed by other depositional processes such as aeolian input or local reworking. Therefore, we suggest the sediment source analysis should be justified prior to flooding reconstruction.

5. Changing flood activity of the Lower Meuse fluvial system in response to climate change and human impact - a synthesis

Fei Peng, Willem Toonen, Cornelis Kasse, Maarten Prins, Ronald van Balen

Abstract

This study presents the Lower Meuse 13,000-year long paleoflood record, compiled from several case studies. The part of the record that spans the late Allerød-Younger Dryas periods is based on the sedimentary infill of an abandoned channel, whereas two independent Holocene flood records are derived from sediments deposited in a floodplain setting and in a levee setting. Rapid flood regime changes are recorded during the Allerød-Younger Dryas climate transition. For the Holocene, multi-centennial flooding phases are reconstructed. At both locations, the Holocene flood records show phases of increased flooding at 8700-8400 cal BP and 8100-7500 cal BP, shortly interrupted by a period of decreased flood activity coeval with the 8.2 ka BP climate event. A next period of increased flood activity occurred between 6100-5000 cal BP and 3000-2600 cal BP. Afterwards, floodings were more active at 2200-1900 cal BP (Roman Period), 1500-1200 cal BP (Dark Ages), 900-600 cal BP (Middle Ages) and 500-200 cal BP (Little Ice Age). In general, the late Holocene flooding record is characterized by rapid changes in flooding regime, with more episodic variability and the occurrence of high-magnitude events, compared to the long-term phasing and relatively lower magnitude flood events that occurred during the early and middle Holocene. From a comparison with climate records in the North Atlantic region it is concluded that variations of the Lower Meuse Holocene flooding regime coincide with records of North Atlantic ice-raft debris events, grand solar minima and the GISP2 glaciochemical series that reflect the strengthening of westerlies. In general, these correlations indicate a regional atmospheric circulation control over the Lower Meuse flooding regime. The general correspondence of enhanced flood activity with intervals of increased storm track activity, as recorded in coastal sequences, lake records and river catchments across Western Europe, corroborates a climate-driven variability in Lower Meuse floods throughout the Holocene. In the last millennia, flooding activity was considerably intensified by the anthropogenic impact on the Meuse catchment. The observed susceptibility of the Lower Meuse flooding regime changes to climate forcing and land use changes suggests an increased threat of high-magnitude flood events in future climate.

5.1. Introduction

The climate system can be characterized as highly variable and complex, as a consequence of being the ensemble expression of numerous internal and external mechanisms, each with oscillations over different timescales (from <1 year to >$1*10^5$ years), acting on varying spatial scales, and often modulating/affecting each other. Several dominant climate forcings and modes of natural variability

have been put forward (see overview in Wanner et al., 2008) to explain climate variability and their expressions on the earth surface dynamics. On a continental scale, numerous fluvial systems and lakes in Europe have been investigated in the last decades, to study the hydroclimatic variability and associated changes in flooding regimes (overview in Wilhelm et al., 2019), mainly to prepare flood-prone regions for the effects of future climate change. From these catchment-specific case studies some large-scale patterns have emerged with straightforward connections to dominant climatic forcings. Yet, there also seems to be considerable differences between records that are located in the same region, with sometimes unclear or even mixed responses to climate oscillations (Harrison et al., 2019; Schulte et al., 2019).

Variations in solar intensity and the North Atlantic Oscillation (NAO) have been suggested to be of particular importance for changes in river base flow and peak discharges. Solar forcing of the North Atlantic climate system was demonstrated by model studies (i.e., Haigh, 1996; Gray et al., 2010) and on the basis of climate proxies; e.g. from tree ring $\Delta^{14}C$ and ice core ^{10}B fluxes (i.e., Stuiver and Braziunas, 1993, 1998; Vonmoos et al., 2006; Steinhilber et al., 2009). Synchronous changes have been observed between reconstructed variations in solar intensity and terrestrial sedimentary records (i.e., Muñoz et al., 2015; Czymzik et al., 2016a; Engels et al., 2016) and historical records that reflect hydroclimatic change (Glaser et al., 2010; Peña et al., 2014). The NAO index describes the large-scale meridional atmospheric pressure difference between the Azores high pressure field and the Iceland low pressure field (Fig. 5.1) (Wanner et al., 2001). Patterns of precipitation over Western Europe are strongly connected to the configuration and intensity of North Atlantic westerly storm tracks. Short term variability such as inter-annual variation in winter precipitation over Western Europe is largely controlled by the NAO (Hurrell et al., 2001). Stronger westerly winds are typical for a positive NAO mode during the winter times and cause warm and wet winters in western Europe which favour floods, while cold and dry winters are characteristic for the negative mode of the NAO and a weakened zonal flow. Therefore, strong correlations between the NAO and increased flood activity have been recorded for many Western European river catchments (i.e., Hall et al., 2014; Foulds and Macklin, 2016; Toonen et al., 2016).

In this study, we present a compiled Lower Meuse paleoflood record spanning the Lateglacial and Holocene, based on the results of previous case studies (Peng et al., 2019; Peng et al., 2020; Peng et al., submitted). The compiled record is compared with proxy records of grand solar minima, North Atlantic ice rafting debris, and GISP2 glaciochemical series that reflect the strengthening of westerlies, to identify the main drivers for Lower Meuse flood regime changes. In addition, the Lower Meuse palaeoflood record is compared with paleohydrological studies from the wider region to detect temporal and spatial coherence of hydroclimatic variability over Western Europe. Observed differential responses in hydroclimatic records to the same overall forcings are used to assess the potential effects of human and physiographic controls on paleoflood registration (e.g. specific geomorphological setting),

and methodological procedures (e.g. sedimentary proxy selection and data processing). Such information fundamentally improves our understanding of paleoflood records, and promotes their successful deployment in current and future flood risk assessments.

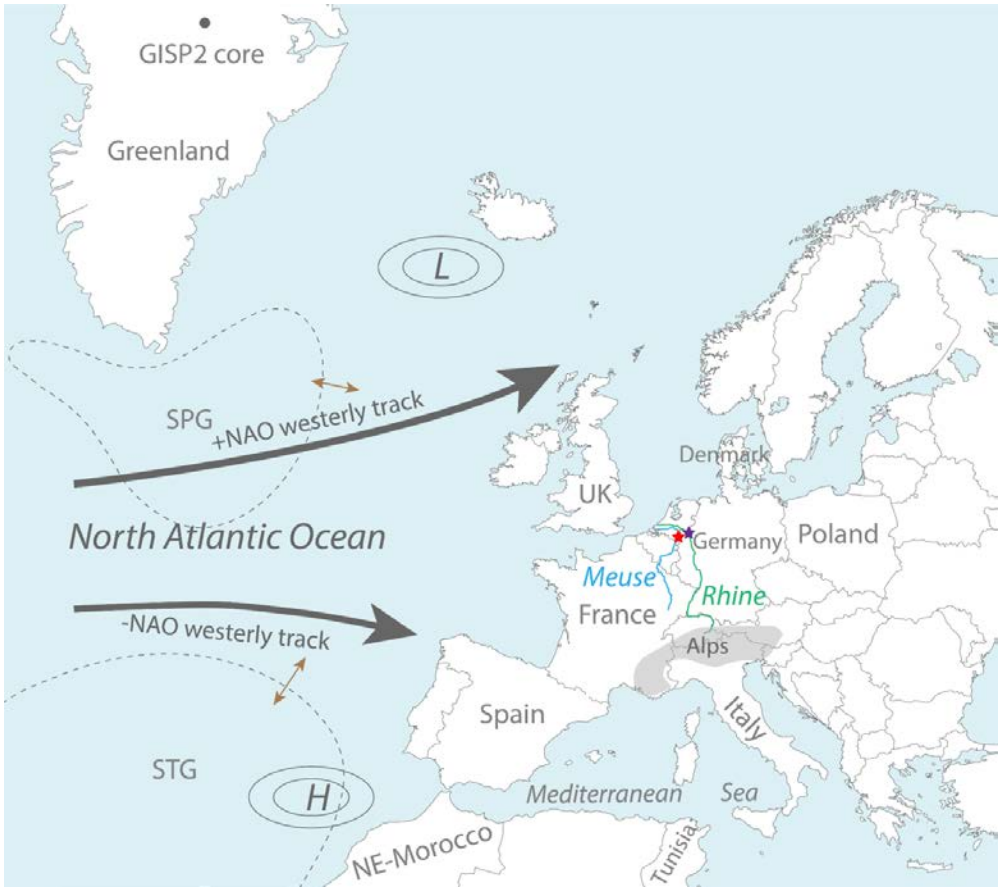

Figure 5.1. Location of the Lower Meuse paleoflood study area (red star), Lower Rhine paleoflood study area (purple star) (Toonen, 2013), paleoclimatic records used for comparison in this study and the main drivers for North Atlantic atmospheric and oceanic circulation. The approximate location of the oceanic subpolar gyre (SPG) and subtropical gyre (STG) is indicated with a dashed line. The brown arrows refer to the variations in the extent of the SPG and STG. L = Icelandic Low; H = Azores High.

5.2. The 13,000-yr Lower Meuse flood record

5.2.1. Study sites and methods

Flood deposits from a levee at Ooijen and the infills of abandoned channels located in the floodplain at the Well-Aijen and the De Ham sites in the Lower Meuse catchment (Fig. 5.2) were investigated to reconstruct the multi-centennial phasing in flood activity for the Lateglacial and Holocene period (Peng et al., 2019; Peng et al., 2020; Peng et al., submitted). The study sites are located on the Venlo Block, a fault-bounded block that has been relatively stable, compared with the adjacent uplifting Peel Block (Houtgast and Van Balen, 2000; Van Balen et al., 2005). Digital elevation maps and studies of river terrace formation (Kasse et al., 1995; Woolderink et al., 2018) suggest that lateral migration of the active channel has been limited at the study sites. Hence, overbank sedimentation at the studied sites

has been inferred as representative of catchment-wide signals rather than relating to local vertical and lateral dynamic channel conditions (Toonen et al., 2020).

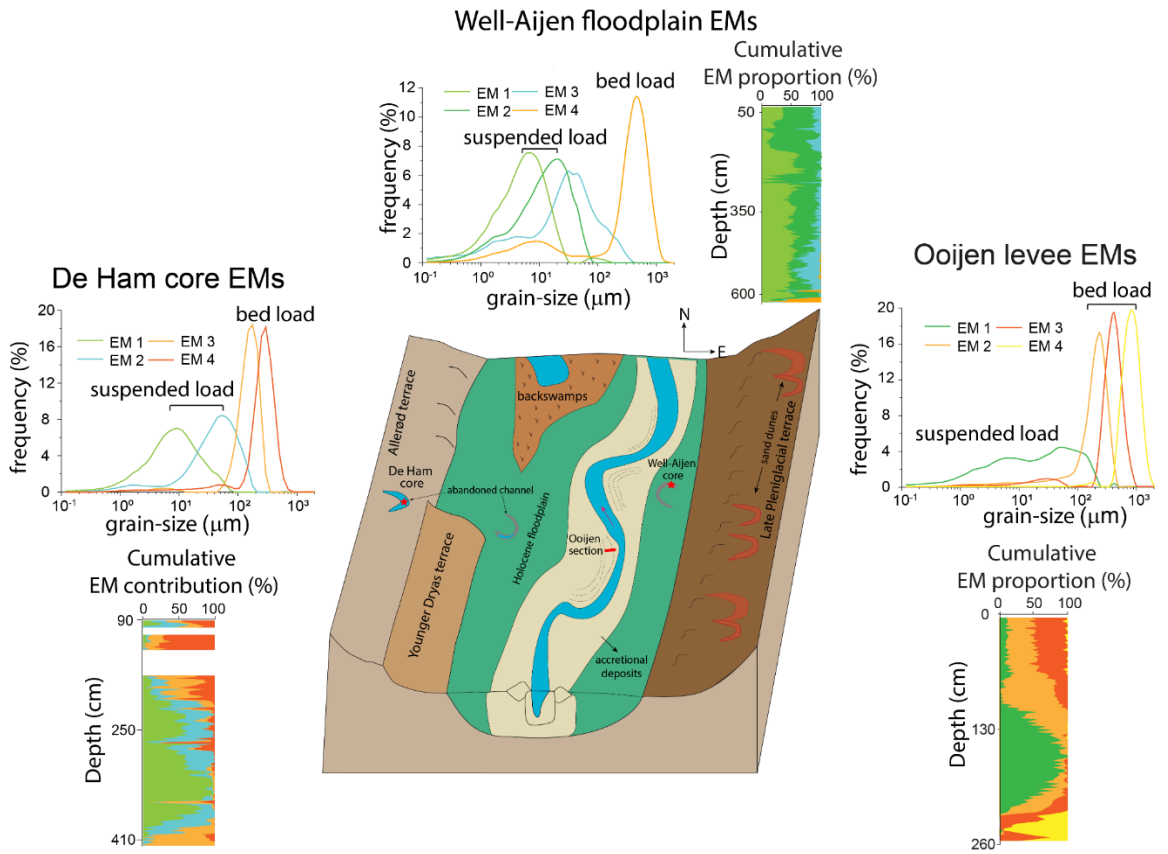

Figure 5.2. Conceptual representation of the Lower Meuse valley morphology, the location of paleoflood studies, and the end-member modelling results of the three investigated sites. The Well-Aijen core was collected from an infilled abandoned channel, located in the Holocene floodplain, and the Ooijen study section was situated on a Holocene levee. The De Ham core was retrieved from an abandoned channel on the higher Allerød river terrace. Inset frames show the grain-size dataset of each study sites, based on volumetric contribution of four end members.

The grain size of overbank deposits was used as the main characteristic to reconstruct the Lower Meuse paleoflood history. At each study site, grain size was analysed at a 2-cm resolution, reflecting approximately 30 years on average at the Well-Aijen and the De Ham sites, and 80 years on average at the Ooijen levee site. The investigated sites are all located close to the Meuse channel, and the analyzed sediments from these sites are believed to have delivered mainly by water during floods. The AnalySize package (Paterson and Heslop, 2015) was applied to perform an end-member modelling analysis (Prins and Weltje, 1999; Weltje and Prins, 2003) to decompose the grain-size distribution dataset into a series of end members. These end members were interpreted in terms of sediment source, and transport- and deposition mechanisms, which cannot be identified using univariate grain-size parameters alone (Prins, 1999; Van Hateren et al., 2018). In the Lower Meuse paleoflooding studies, the end members were classified as suspended load and bed load. The former represents suspended and wash load populations, for which it is assumed that limited differentiation occurs between different flood magnitudes, as these fine particles are also in suspension during normal flow (Toonen et al., 2015a). The volume and

coarseness of the bed load fraction in overbank deposition is used to indicate the relative magnitude of flood events. The end-member modelling results served to establish a flood energy index (FEI) (Peng et al., 2019). The 5-point averaging of raw data is applied to all the presented FEI records in this paper to reduce noise in the flooding signal. The results reflect phases of flood activity rather than single event magnitude quantifications.

5.2.2. Late Allerød-Younger Dryas flood record

Qualitative paleohydrological reconstructions for the Younger Dryas time period were first established in the Mark valley in the southern Netherlands (Bohncke et al., 1987). Later studies compiled similar records for the Lower Meuse valley (Bohncke et al., 1993; Kasse et al., 1995), and mainly focussed on general lithological changes, e.g. sandy Younger Dryas fluvial sediments contrasting with silty Allerød sediments, to infer large-scale changes in fluvial style and flood regime. Our studies provide the first quantitative results on flood activity, and show that the generally decreased Lower Meuse flooding intensity in the late Allerød. In the intra-Allerød cold period (IACP) (Stuiver and Grootes, 2000), a small increase in flooding was also recorded by the FEI index (Fig. 5.3) and other sedimentary proxies (organic matter content, and biogenetic $\delta^{18}O$ and $\delta^{13}C$ isotopes) (Peng et al., submitted). Subsequently this was followed by rapidly increased flooding conditions at the onset of the Younger Dryas. A phase of high flood activity was maintained for the entire duration of the Younger Dryas period (Fig. 5.3).

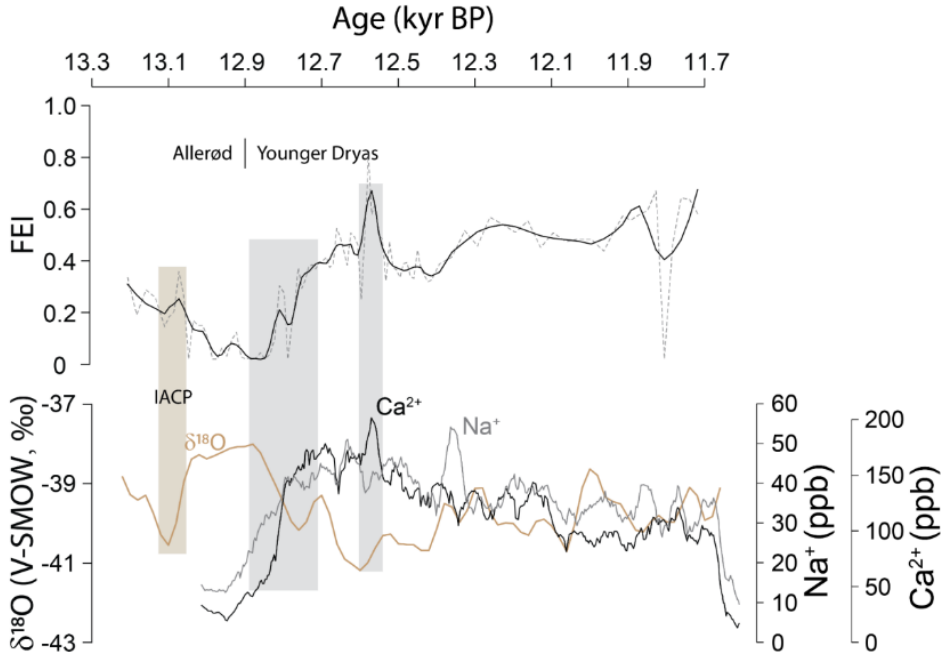

Figure 5.3. The 5-point averaged Lower Meuse FEI flood index (raw data in dashed line), showing variation in flood activity from the late Allerød to the Younger Dryas period (Peng et al., submitted), and the $\delta^{18}O$ record and glaciochemical series (Na^+ and Ca^{2+}) from the GISP2 ice core (Mayewski et al., 1997). The intra-Allerød cold period (IACP) is highlighted in brown shading. The grey shading indicates phases of correspondence between the FEI index and the ice core climate proxies.

The Allerød-Younger Dryas transition is regarded as an impactful warm-cold climate oscillation that occurred worldwide, and the concomitant change in atmospheric circulation (Isarin et al., 1997; Brauer et al., 2008) must have impacted the precipitation regime over the Lower Meuse catchment, which altered the average and peak discharges significantly. The deteriorated climate resulted in reduced vegetation cover and degraded soil stability, which affected surface runoff and sediment supply from upland regions. In response to changes in discharge and sediment load the Meuse transformed from a meandering system to a braided system (Kasse et al., 1995). The variations in Lower Meuse flood activity at the Allerød-Younger Dryas transition should, therefore, be considered as the combined result of (external) regional hydroclimate change and (internal) local fluvial channel- and floodplain form changes.

5.2.3. Holocene flood record

Two 9000-yr long Holocene flood activity records were reconstructed from the sedimentary infill of an abandoned channel (Peng et al., 2019) and from levee sediments (Peng et al., 2020), respectively. The levee sediments were exposed during an archeological survey (Ellenkamp et al., 2018). The FEI index deployed at the floodplain site calculated the ratio of coarse-grained fraction (31-105 μm) over the rest (0.12-105 μm). In addition, the FEI-index was designed in such a way that it corrects for the presence of Fe-Mn concretions and resistant organic material in the coarsest sediment fraction, which affected the quality of end-member modelling results (Peng et al., 2019). For the levee-based index, the volume ratio of two coarsest end members (EM3-EM4) were highlighted over all the bed load end members (EM2-EM4) (Peng et al., 2020). Despite the slight difference in setting and methodology, the two independent records generally show consistent results (Fig. 5.4e).

Both records show higher magnitude flooding phases of shorter duration during the late Holocene, in contrast with lower magnitude flooding phases of longer duration in the early and middle Holocene (Fig. 5.4e). High flooding phases are recorded at 8700-8400 cal BP and 8100-7500 cal BP, which were interrupted at 8.2 ka BP. This was followed by the high flooding phase at 6100-5000 cal BP. Generally reduced flood activity was registered between 7500-6100 cal BP. At ~7 ka cal BP, the floodplain-based record shows a high flooding phase condition but this is not reflected in the levee-based record (Fig. 5.4e). It is possible that later human disturbance or soil formation on the levee erased the flooding signal (Ellenkamp et al., 2018). From 5000 to 3800 cal BP, the Lower Meuse experienced a prolonged period of reduced flooding (Fig. 5.4e). The floodplain-based record shows a gradual increase in flood occurrence starting from ~3800 cal BP and peaking around 3000 cal BP (Fig. 5.4e), followed by a sharp decline until 2200 cal BP. The levee record suggest, however, an opposite phasing in flooding between 3800-2200 BP compared to floodplain records.

During the late Holocene, from 3000 cal BP until the present, the phasing in flood activity becomes more variable with higher amplitudes but overall shorter duration of each phase (Fig. 5.4e), especially

at 2200-1900 cal BP (Roman Period), 1500-1200 cal BP (Dark Ages), 900-600 cal BP (Middle Ages) and 500-200 cal BP (Little Ice Age) (Fig. 5.4e).

5.3. Lower Meuse flood regime changes in response to climate perturbations and human interference

To identify the main forcings for phasing in the Lower Meuse paleoflood activity the data series were compared with paleo-climate archives that are regularly deployed as reference for (changes in) regional temperature and precipitation; e.g. solar forcing variations established from tree ring $\Delta^{14}C$ and ice core ^{10}B analyses, the North Atlantic IRD events from the North Atlantic Ocean, and oxygen isotopes and glaciochemical series from the GISP2 ice core.

5.3.1. Rapid flood intensification following the late Allerød-Younger Dryas climate transition

The rapid increase in floods activity at the late Allerød-Younger Dryas transition closely follows the sharp increase of the nss (non-sea-salt) Ca^{2+} and ss (sea-salt) Na^{+} and the decline of $\delta^{18}O$ in GISP2 ice core (Fig. 5.3). The GISP2 glaciochemical series (e.g., sodium, calcium, etc.) reflects the history of atmospheric circulation over the northern hemisphere (Mayewski et al., 1997). Elevated nss Ca^{2+} was interpreted as strengthened westerlies (Mayewski et al., 1997; Lenton et al., 2012; Benito et al., 2015a), and the decrease in ss Na^{+} reflects the increase in Icelandic Low pressure, thus resembling a positive NAO state (Mayewski and Maasch, 2006). The synchronous intensification of the Lateglacial flooding in the Lower Meuse record with the strengthened westerlies implies a strong control by the latter over Western European discharge variability during the Lateglacial.

The periglacial environment and substantial decline in temperature during the Younger Dryas (Bohncke et al., 1993; Kasse et al., 1995) indicates that a positive-like NAO condition, which would bring warm and moist winters (by strong zonal westerlies) is not the case. Although some argue for an Allerød-like wet climate during the early Younger Dryas (Hepp et al., 2019), this is unlikely to account for a significant increase in flood activity. Instead, it seems plausible that the lower temperatures reduced soil water storage capacity because of frozen soils and reduced vegetation-infiltration, which in combination with increased snow accumulation during the winter could have led to the generation of higher peak discharges during spring.

5.3.2. Holocene Lower Meuse floods, climate change and human interference

Many proxy data and climate modelling results indicate a strong link between variations in solar activity and changes in precipitation over the North Atlantic region (i.e., Lockwood et al., 2010; Ineson et al., 2011; Martin-Puertas et al., 2012; Czymzik et al., 2013; Van Geel et al., 2014; Czymzik et al., 2016b). Several studies have found that a small change in solar forcing can be amplified via the atmosphere system (Magny, 1993; Shindell et al., 2001), and thus trigger a sensitive response of the climate system on multi-decadal to centennial timescales (Björck et al., 2001; Ammann et al., 2007; Martin-Puertas et

al., 2012). Phases of enhanced flood activity in the Lower Meuse at 8100-7500 cal BP, 6100-5000 cal BP and during the late Holocene generally coincide with the reconstructions of multi-decadal to centennial (grand) solar minima (Usoskin et al., 2007) (Fig. 5.4a, e). In addition, the intervals at 7000-6200 cal BP and 5000-3000 cal BP are characterized by low flood activity phases and absence of grand solar minima (Fig. 5.4a). Specifically, at ~2750 cal BP, the high flooding phase matches with the solar minimum which has been proposed as the main cause of a wetter and cooler climate pattern in NW Europe (Van Geel et al., 1996; Van Geel et al., 1998; Mauquoy et al., 2008; Van Geel et al., 2014; Mellström et al., 2015). The more recent Oort (~910 cal BP), Spörer (~480 cal BP), Wolf (~650 cal BP) and Maunder (~270 cal BP) solar minima also correspond with the latest two flooding phases in the Middle Ages and the Little Ice Age (Fig. 5.4e); especially the Oort and Spörer solar minima occurred just preceding the reconstructed flooding phases. The alignment thus suggests that (the modulating effect of) solar forcing was an important driver of Lower Meuse flooding.

Further indications for the influence of variations in solar activity come from the observation that Lower Meuse flood activity phases coincide well with the IRD events (Bond et al., 2001) and the increased GISP2 ice core Ca^{2+} and Na^{+} values (Mayewski et al., 1997) throughout the Holocene (Fig. 5.4b, c, e). The IRD record reflects major periods of the North Atlantic Ocean surface cooling. In addition, it is suggested to represent a shift of the main atmospheric streams toward lower latitudes, generate slow-moving cyclonic perturbations over those regions (Lamb, 2002). The concurrence of the IRD events and increased Ca^{2+} and Na^{+} values in ice core records (Fig. 5.4b, c) implies that during the cold periods the North Atlantic Ocean surface and the atmosphere above Greenland were a coupled system that underwent recurring shifts on millennial time scales. Hence the related displacement of cyclonic tracks probably played a dominant role in the Lower Meuse paleoflood records.

Solar activity and the North Atlantic climate are demonstrated to be correlated through NAO related atmospheric circulation on a decadal to centennial time-scale (e.g., Boberg and Lundstedt, 2002; Kodera, 2002; Kodera and Kuroda, 2005). A general correlation between a negative mode of the NAO and grand solar minimum (Usoskin et al., 2007) can be observed since 3.5 ka BP (Fig. 5.4a, d). During the cooling of the North Atlantic surface, the shift of the atmospheric streams to the lower latitudes (Mayewski and Maasch, 2006) would further explain the link between (modulated) solar forcing and the Lower Meuse records. Yet, a recent high-resolution rainfall index from Northern Morocco (Ait Brahim et al., 2019) pointed out that the negative NAO modes associated with IRD events only occurred during the early and late Holocene (IRD events 0-1, 5b-8). During the middle Holocene IRD events (2-4) a general positive NAO mode prevailed. Similarly, there are ongoing debates concerning the prevalence of a persistent positive NAO mode during the Middle Ages (Trouet et al., 2009; Ortega et al., 2015) and the impact of solar forcing on climate proxy records (Moore et al., 2006).

These apparent deviations demonstrate that the effect of solar forcing is not one-directional and that additional factors or internal responses (e.g., Arctic Oscillation and Atlantic Multidecadal Oscillation)

of the North Atlantic climate system played an important role in storm track configurations over Western Europe and the Meuse catchment. In this respect, the ~8200 ka BP event is a notable anomaly. This abrupt cold event is believed to be caused by the release of ice-dammed meltwater from proglacial Lake Agassiz and the associated collapse of the Atlantic Meridional Overturning Circulation (Alley and Ágústsdóttir, 2005). Previous studies argued the precipitation variation in Europe during the 8.2 ka event (i.e., Magny et al., 2003; Prasad et al., 2006; Prasad et al., 2009). The low flooding condition at 8.2 ka is clearly reflected in Lower Meuse records which indicates its susceptibility to abrupt and rapid climate change, in this case cooling, and this observation also supports an overall dry cold hydrological condition in NW Europe.

Starting from 2500 cal BP, the phases in Lower Meuse flood activity is characterized by larger amplitudes, shorter durations of each phase, and marked by rapid changes, which contrasts with the more prolonged flood activity phases during the early-mid Holocene. During this time-period in the late Holocene, the Lower Meuse catchment experienced large-scale land-use changes, especially during the Roman Period and the Middle Ages (De Moor et al., 2008; Bos and Zuidhoff, 2015; Ellenkamp et al., 2018). In the Geul river, a tributary of the Lower Meuse, the high sediment input and subsequent high flood activity during the Roman Period and Middle Ages caused a significant increase in floodplain sedimentation (De Moor et al., 2008). Increased land use and large-scale deforestation of loess upland areas of the Meuse catchment led to reduced river bank stability, infiltration capacity and evapotranspiration, and caused increased runoff and erosion (Ward et al., 2009; Notebaert and Verstraeten, 2010; Notebaert et al., 2011). Such changes are generally suggested to make lowland river systems more vulnerable to flooding (Hoffmann et al., 2009; Ward et al., 2009; Macklin et al., 2013). That is, a small increase in river discharge could induce a flood with larger magnitude. From the observed changes in our paleoflood records and the contemporaneous human-related shifts in the Meuse catchment it can, therefore, be concluded that the anthropogenic landscape change caused the fluvial system to become more sensitive to climatic variations of the last two millennia.

5.4. Discussion

5.4.1. Methodology in paleoflood reconstructions

5.4.1.1. FEI index

In the Lower Meuse paleoflood studies (Peng et al., 2019; Peng et al., 2020; Peng et al., submitted), the flooding phases are mainly determined by FEI, which is based on the end member modelling results. The values of the FEI index depend on the proportions of end member against the core/section depth. The end-members composition and amount are not only determined by the sediment grain size composition, but are also influenced by the end-member modelling methods. We adopted the same end-member modelling method, the AnalySize package (Paterson and Heslop, 2015) in the Lower Meuse paleoflood reconstructions. Van Hateren et al. (2018) demonstrated that the application of AnalySize is

able to yield more accurate end member results than other methods (i.e., BEMMA, DRS-unmixer and EMMAgeo). Although the FEI index method reconstructed the Lower Meuse flooding phases, this method can also potentially resolve individual flooding or a cluster of short flood events if a high-resolution age-model is available.

Using the FEI index method differs from conventional flooding reconstruction approaches (i.e., median, P90, and sand fraction), and we propose this is a promising and meaningful method in flood reconstruction. First, the construction of FEI uses all the end members (consisting of both suspended load and bed load), and thus the complete fluvial transport mechanism is taken into account. This consideration is in contrast to the sole use of coarse grains and coarse end members. Second, the FEI method resolves the dilemma when there is only very limited or no sandy component in the sediments (which have been used in previous past floods studies, i.e., (Beierle et al., 2002; Benedetti, 2003; Czymzik et al., 2013). Third, this method allowed to eliminate the effect of Fe-Mn nodules and organic flocculation in grain-size analysis results. By applying this method, the effect of contaminated portions in grain-size datasets can be minimized. In that sense, this method is also applicable elsewhere when encountering similar challenges (Peng et al., 2019). Last, at the Ooijen levee setting (Peng et al., 2020), the application of FEI diminishes the effects of fluvial dynamics (i.e., gradually elevated levee height and down-cutting of the river channel) on each end member component by the offset of division in FEI construction, and these effects, however, cannot be avoided by using single parameters (median/P50, P90 and sand fraction).

5.4.1.2. Dating

Age control is crucial in interpreting the hydrological variation in history. The age models in reconstructing Lower Meuse flood records are based on AMS ^{14}C dating, archeology, palynological subdivisions, and age-tuning by correlating the granulometry-based parameters (FEI index) with accumulation rate. The AMS ^{14}C dating produced robust results and agreed well with the biochronology derived from the pollen diagram (which could also reflect the climate change in certain geological period by analyzing the paleovegetation pattern) and archeological information (see Peng et al., 2019; Peng et al., 2020; Peng et al., submitted). Archeological information was obtained from a large excavation, during which the discovered artefacts were used to subdivide the sedimentary sequence into archeological time-periods (Bos and Zuidhoff, 2015; Ellenkamp et al., 2018). When datable organic material for AMS ^{14}C dating is absent and OSL is not applicable, age-tuning can be used. This method assumes a coarser sedimentary sequence deposited faster than finer sequence. A similar principle was successfully applied in fluvio-lacustrine sequences by Minderhoud et al. (2016), who linked the organic matter content with sediment accumulation rates. Overall, these dating methods produced reliable age models in Lower Meuse paleoflood reconstructions. This is reflected by the general match of the high flooding phases with regional and local hydrological and climatic records and specially, the capture of 8.2 ka event in both Holocene flood records (Fig. 5.4e).

5.4.2. A regional comparison of hydroclimate proxy records

Generally, paleohydrological changes can be studied either via the direct analyses of sedimentary archives (i.e., lacustrine sediments like varve layers, fluvial sediments, speleothems), focussing on the frequency/magnitude of flood deposition or their sedimentary characteristics, or by tracking changes in fluvial settings in so-called cumulative probability density function studies. In this section we correlate the Lower Meuse flood record with existing hydrological studies on storminess history, lake-level changes, and flood records obtained from fluvial and lake sediments. These records were reconstructed from a wider region in Europe, thus a comprehensive correlation should be able to shed light on the understanding of regional climate and human impacts on hydrological dynamics.

5.4.2.1. North Atlantic storminess record

Sorrel et al. (2012) synthesized the paleostorm records produced from the English Channel and the northern Europe coastal regions (from northwestern France to southern Sweden), to establish a stacked storminess chronology for the past 6000 years (Fig. 5.4f). To extend the storminess chronology to 9000 cal BP, we supplemented this by a Holocene North Atlantic storminess study from the coast area of western Denmark (Goslin et al., 2018) (Fig. 5.4f). Together, the two storminess records generally show the periods of enhanced storminess to be synchronous with the Lower Meuse flooding phases throughout the Holocene (Fig. 5.4e, f). For example, at 8500 cal BP, 7800 cal BP, 5600 cal BP, 2800 cal BP, 1400 cal BP and the Little Ice Age. Exceptions occur at the 5000-3800 cal BP, Roman Period and warm Middle Ages (Fig. 5.4f). At 5000-3800 cal BP, a series of fluvial floodings were registered in European river systems (Fig. 5.4f), while the Lower Meuse experienced a low flooding condition, and only the floodplain-based record shows a gradually increased flooding condition from ~3800 cal BP onwards (Fig. 5.4e). Considering that the levee setting is more prone to be impacted by later alterations, such as human activity or erosion by breaches during floods, the floodplain-based reconstruction is more reliable, and thus it is likely that the flooding conditions indeed increased from 3800 cal BP. The exact reason of the subdued flooding period at 5000-3800 cal BP is unclear. However, it is interesting to note that the grand solar minima did not occur in this interval (Fig. 5.4a).

The composite storminess record lines-up with the IRD events (Fig. 5.4c, f). Goslin et al. (2018) concluded that the strengthened and northward-located westerlies and storm-tracks in the North Atlantic resulted in the enhanced subpolar gyre (SPG) which promoted the IRD events. In addition, the strengthened winter westerlies activity was likely to be induced by the weakened solar forcing (Lockwood et al., 2010; Ineson et al., 2011; Thiéblemont et al., 2015). These studies indicate a main control of the solar activity on the westerlies regime over the North Atlantic sector. Another paleostorm record (Fig. 5.4f) from the NW Mediterranean Sea pointed out that the high storm activity in the NW Mediterranean Sea is in agreement with the changes in coastal hydrodynamics observed over the Eastern North Atlantic and corresponds to Holocene cooling in the North Atlantic (IRD records, Fig. 5.4c) which have led to a stronger meridional temperature gradient and a southward migration of the

westerlies (Sabatier et al., 2012). On the other hand, the NAO index record (Olsen et al., 2012) shows multi-decadal to multi-centennial negative modes at ~4200 cal BP, ~3300 cal BP, ~2800 cal BP, ~2100 cal BP and during the Little Ice Age at ~300 cal BP (Fig. 5.4d). During three (~4200 cal BP, ~2800 cal BP and ~300 cal BP) of these negative NAO periods, the enhanced storm activities were registered in the eastern coast of the North Atlantic and in the NW Mediterranean (Fig. 5.4f). Another interesting point is that the high storm records from both areas correlate well with the IRD record (Fig. 5.4c, f) and this has been asserted in these studies (Sabatier et al., 2012; Sorrel et al., 2012; Goslin et al., 2018). This non-unidirectional westerlies regime has been explained by the reorganization of ocean and atmosphere circulation during the long-term cooling of North Atlantic surface (Renssen et al., 2009; Thornalley et al., 2009; Colin et al., 2010; Sorrel et al., 2012). That is, the southward-shifted westerlies during cold periods led to the westward contraction of the SPG (negative like NAO condition), and this process was accompanied by the norward-moved subtropical gyre (STG) which was associated with the storm tracks to northern Europe. This is important for the Lower Meuse paleohydrology because the phases were also coeval with the IRD events (Fig. 5.4c, e), both during the negative and positive NAO modes (i.e., at ~2800 cal BP, ~2100 cal BP and ~1300 cal BP, Fig. 5.4d, e). In this context, the reorganizations of both high and low latitude atmospheric circulations (i.e., SPG and STG variations), and the southward shift of North Atlantic winter storm track under future climate warming (as a result from sea-ice extent decreases and mid- to high-latitude temperature gradient decreases, Orme et al., 2017) can further complicate the simple correlation of the Lower Meuse flooding phase with a single-mode NAO pattern. Further, this more unpredictable situation leads to a high potential flooding regime in context of the climate change, especially more frequent extreme climatic events (IPCC, 2019).

5.4.2.2. Flood and lake-level records derived from lake sediments

The mid-European lake-level record is a synthesis of a series of Holocene lake-level variations (Magny, 2004). By making this compilation, a variety of local, non-climatic factors, including natural infilling, local damming, vegetation cover changes and people impacts, which can influence the lake-level changes, are avoided (Dearing and Foster, 1986; Harrison and Digerfeldt, 1993). A teleconnection comparison of the mid-European lake-level variations with the IRD and Polar Circulation Index (established from GISP2 glaciochemical series, the values increased in colder climate, (Mayewski et al., 1997)) also indicates that changes in the solar activity play a major role in influencing the lake-level changes over the North Atlantic area. However, a comparison of the Lower Meuse flooding phases with the lake records shows a general anti-phase relation (Fig. 5.4e, f), except at 6000-5000 cal BP, 2700 cal BP and in the Middle Ages and Little Ice Age. If the lake-level variations and the Lower Meuse fluvial activity are both controlled by solar forcing, the discrepancies between the two records can be attributed to the differences in response/sensitivity to climate change between the lake and fluvial systems, or the uncertainty in age-control. On the other hand, Macklin et al. (2006) concluded that river basins can respond, through variations in the frequency and magnitude of major floods, more rapidly to climate

change than lake systems. If this can be confirmed by more high-resolution datings, then the fact that the Lower Meuse flooding phases slightly precede the lake-level records (especially since the 3000 cal BP, Fig. 5.4e, f) can be explained. A nearby example is the Lake Uddelermeer (centre Netherlands). Recent lake-level reconstruction attributed the high lake-level since 2800 cal BP to increased precipitation (Engels et al., 2016), and this change in atmospheric circulation could have started as early as 3500 cal BP (Van den Bos et al., 2018). The floodplain-based Lower Meuse flood record suggests that the onset of the active fluvial regime started at ~3800 cal BP (Fig. 5.4e), preceding the date derived from the Lake Uddelermeer sediments. This may indicate that fluvial system responds faster than the lake systems.

The history of flood activity derived from the southern Alps lake sediments (Fig. 5.4f) is believed to be a most robust record reflecting negative NAO modes (Wirth et al., 2013). The lake-sediments-inferred flood record for the southern Alps agrees well with the Lower Meuse flooding phases centred at ~8600 cal BP, ~5500 cal BP and ~2800 cal BP (Fig. 5.4e, f), during which the hydrological dynamics were mainly dominated by climate changes both in the southern Alps and the Lower Meuse catchment (Wirth et al., 2013; Bos and Zuidhoff, 2015). However, most of the recorded floods in the southern Alps occurred in summer and autumn, because ice cover and precipitation in the form of snow in winter at high-altitude sites inhibit the generation of flood layers. In that sense, the flooding season in this area differs from that of the Lower Meuse which mainly experiences floodings in winter and spring. In addition, the southern Alps flood frequency was also higher in cooler periods, coinciding with lows in solar activity (Fig. 5.4a, f). Wirth et al. (2013) proposed that the shrinking/expansion of the Hadley cell with decreasing/increasing air temperature caused wet/dry conditions in Central Europe during phases of low/high solar activity. This indicates that, a long-term low solar forcing, on the one hand, translate its signal into the strengthened surface mid-latitude westerlies activity during the winter season (Goslin et al., 2018) which resemble a negative-NAO mode and this further brings wetter climate to southern Europe. Meanwhile, the westward and contracted SPG was accompanied by a reinforced penetration of STG northwards, resulting in the high storm activity at the eastern coast area of the North Atlantic (Copard et al., 2012; Sorrel et al., 2012). On the other hand, the shrinking of the Hadley Cell due to the decreasing air temperatures and ocean-atmosphere coupling in summer times leads to a more humid climate and also more floods in the Alpine realm (Lu et al., 2007; Gray et al., 2010; Martin-Puertas et al., 2012; Wirth et al., 2013).

5.4.2.3. Lower Rhine flood record

Toonen (2013) studied Lower Rhine flood events over the past 8100 years by analyzing the sedimentary infill of abandoned channels. Based on the event-scale paleoflood records, multi-decadal to centennial-scale flood-rich phases were identified (Toonen et al., 2017) (Fig. 5.4f). The study areas in the Lower Rhine and the Lower Meuse are close to each other and both are located in the western part of the European continent (Fig. 5.1) and, therefore, can be considered to be under the same climate control.

Both rivers flooding regimes are dominated by precipitation from storm tracks. This allows a fairly direct comparison of results in terms of methodology and hydroclimatic setting. The catchment of the Rhine is, however, larger than that of the Meuse (185,000 km^2 versus 33,000 km^2), reaches further south into central Europe, and covers a more diverse hinterland. Moreover, the Lower Rhine peak discharges are also influenced by snow-melt and glaciers from upland regions, with makes it a mixed rain-snow flood regime compared to the rain-dominated flood regime of the Meuse. Therefore, the Lower Meuse should be regarded as a more direct and sensitive recorder of changes in flood frequency in response to the variations in precipitation that are driven by patterns in atmospheric circulation over Western Europe. Generally, the Lower Meuse and Lower Rhine have comparable paleoflood records, especially when considering the floodplain-based Lower Meuse record. For example, the concurrent flooding phases centred at 7900 cal BP, 5500 cal BP, 1400 cal BP and 300 cal BP (Fig. 5.4e, f). But the onset and length of the Lower Rhine flooding records do not always coincide with the Lower Meuse flooding phase records (Fig. 5.4e, f).

5.4.2.4. Fluvial flood records

By applying cumulative probability density function (CPDF) plots to radiometric dates obtained from various study sites (^{14}C and OSL) that have been classified on the basis of sedimentary environment and evidence for changing depositional regime,

Macklin et al. (2010), Benito et al. (2015a) and Benito et al. (2015b) identified multi-centennial length periods of Holocene flooding and river instability in temperate European regions (UK, Germany and Poland) and the Mediterranean region (Fig. 5.4f), using cumulative probability density function (CPDF) analyses applied to radiometric dates of changes in fluvial environment and depositional regime. At a multi-centennial to millennial scale, the Lower Meuse flooding record agrees with the temperate region composite flooding history during the Holocene. Phases of increased flood activity in the UK generally match those of the Lower Meuse in the last 8000 years (Fig), except at 7500-6000 cal BP and ~4800 cal BP. Similar to the Lower Meuse, phases of increased flood occurrence in the UK (Macklin et al., 2010) and other temperate river basins (Benito et al., 2015a) occurred at times when the ice-rafted debris index was increasing or high (Fig. 5.4c, f). These previous studies also support the connection between the cooling of the North Atlantic region and pervasive flooding conditions over Western Europe, as demonstrated in Section 5.3.2 by correlating the Lower Meuse flood records with the IRD events (Fig. 5.4c, e). In the Mediterranean river catchments, the major flooding phases show an anti-phase with the flooding record in the Lower Meuse during the middle Holocene (Fig. 5.4e, f). More frequent flooding events in the late Holocene partly overlap with that from the Lower Meuse. Considering that the NAO-controlled westerlies account for the precipitation regime on the European continent, the anti-phase phenomenon should reflect the NAO mode changes, which is in agreement with the results of Magny (2004) who observed similar patterns in Holocene lake-level variations over Europe.

CPDF studies do often relate fluvial change to the occurrence of extreme events. But some caution should be taken when interpreting temporal fluvial dynamics changes. The compiled are gathered from a variety of temporal and spatial scales. Therefore, dated changes in fluvial deposition/dynamics are potentially not exclusively related to (extreme) floods or flooding phases, but could also be attributed to local non-flooding causes, like bioturbation, human disturbance and local landform change (i.e. caused by instability of hillslopes and river banks). Furthermore, the dates in the last millennia may have been overrepresented due to preservation issues; the older part of the record may have been eroded, for example by extreme events. In addition, some of the ^{14}C dates, that were based on bulk sediment, could return different results nowadays with the updated AMS technique. As to the spatial distribution of the dates, the rivers in different geomorphological settings and rivers with various scales can react differently to the same climatic forcing at the same period. On the other hand, the dates collected from uplands, lowlands and various climatic sub-regions have been added together.

In the late Holocene (after 3000 cal BP), the impact of humans on the landscape (deforestation, land use) and rivers (regulations, discharge, sediment load) increased in the temperate regions (Foulds and Macklin, 2006; De Moor et al., 2008; Macklin et al., 2010; Broothaerts et al., 2013; Benito et al., 2015b; Bos and Zuidhoff, 2015). In this context, the overall comparable phasing in Lower Meuse flood activity, and that of British and other temperate region river basins, implies that these supra-regional changes were predominantly climate-driven. But the increased frequency of floods and higher magnitudes suggest that anthropogenic impact could have amplified the natural variability. This may, therefore, also be part of the explanation of the difference between the reconstructed low storm activity during the Roman Period and the Middle Ages and pervasive high-flooding phases in European river systems (Fig. 5.4f) has also been observed in the Northern French Alps area (Giguet-Covex et al., 2012) and the Mediterranean region (Faust et al., 2004).

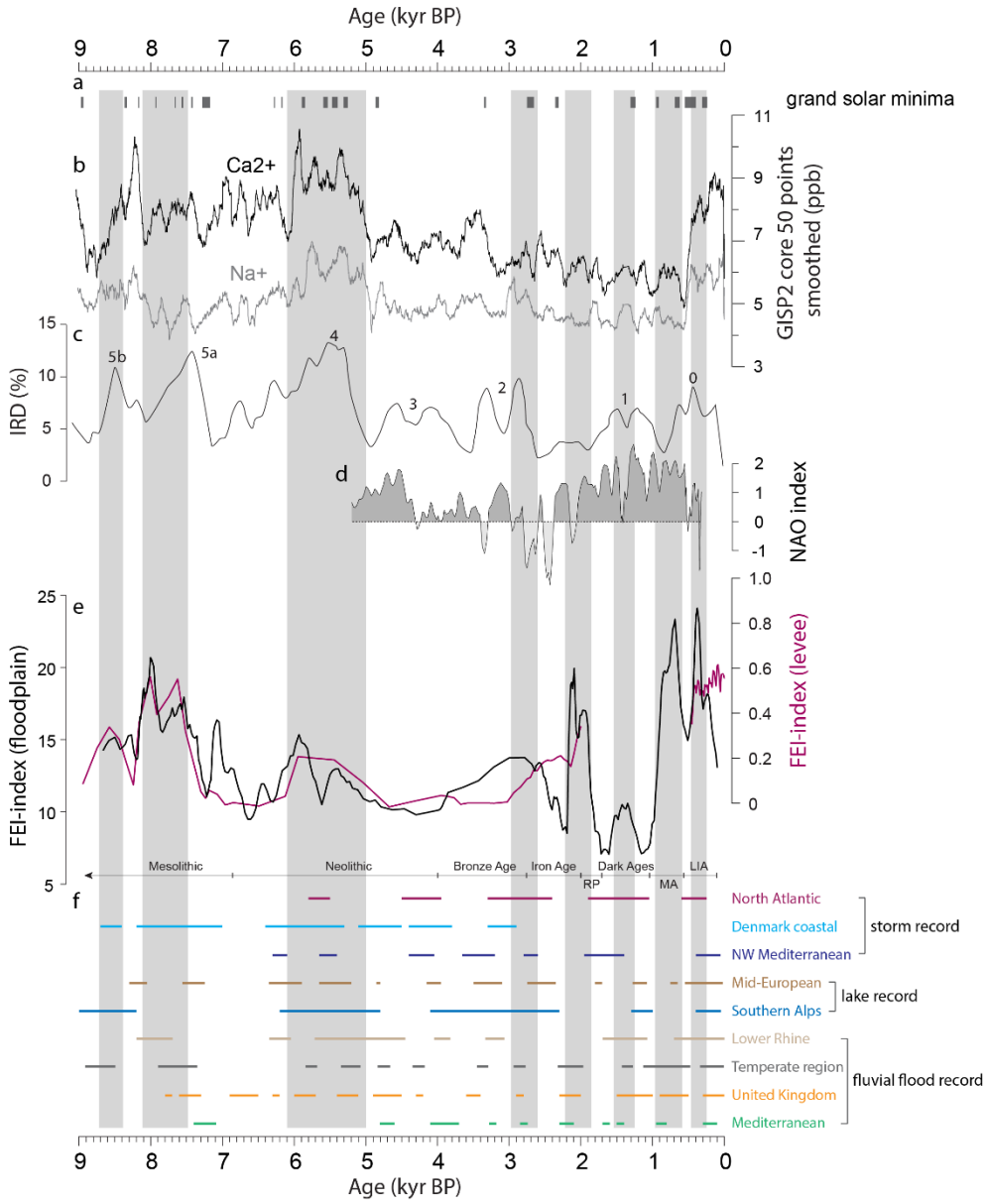

Figure 5.4. Comparison of the Lower Meuse Holocene flood records (frame e: Peng et al., (2019) and Peng et al., (2020)) with (a-d) North Atlantic climatic proxies, and (f) European hydroclimate proxies from fluvial systems, lakes and coastal environments. The data in frames a-d were compiled from Usoskin et al., (2007); Mayewski et al., (1997); Bond et al., (2001); Olsen et al., (2012). The storm records are from Sorrel et al., (2012); Goslin et al., (2004) and Sabatier et al., (2012). The lake records are from Magny, (2004) and Wirth et al., (2013), respectively. The fluvial flood records are from Toonen et al., (2017); Benito et al., (2015a); Macklin et al., (2010) and Benito et al., (2015b). The two flood energy indexes in (e) are processed from the raw data (dash line) using 5-point averaging. The vertical bands of grey shading indicate Lower Meuse high flooding phases.

5.5. Conclusion

The 13,000-yr Lower Meuse flood record provides a long-term history of hydrological dynamics which serves the understanding of the interaction between climate change, human impact and fluvial behaviour. This flood record compilation is based on two Holocene flood reconstructions, conducted in a floodplain setting and a levee setting, and a late Allerød-Younger Dryas reconstruction from the

sedimentary infill of an abandoned channel. The Lower Meuse exhibited a rapid response to the turning point of climate deterioration from the late Allerød to the Younger Dryas. A phase of reduced flooding in the late Allerød was followed by a quick increase at the start of Younger Dryas. This change synchronizes with climate cooling and strengthening of westerlies. The main reason to account for this is the snowmelt water, combined with reduced soil water infiltration and storage capacity, to trigger higher peak discharges during spring. Overall, the two Holocene flood records agree well and show increased flooding phases at 8700-8400 cal BP and 8100-7500 cal BP, 6100-5000 cal BP, 3000-2600 cal BP, 2200-1900 cal BP (Roman Period), 1500-1200 cal BP (Dark Ages), 900-600 cal BP (Middle Ages) and 500-200 cal BP (Little Ice Age). The late Holocene flooding record is characterized by rapid changes in flood regime, with more episodic variability and the occurrence of high-magnitude events, compared to the long-term phasing and relatively lower magnitude flood events that occurred during the early and middle Holocene.

Through a comprehensive comparison of the Lower Meuse flood record with regional climate proxies (grand solar minima, Ca^{2+} and Na^{+} values in GISP2, North Atlantic IRD records and NAO index) and a series of European paleohydrological reconstructions (storminess, lake-level, and flood records obtained from fluvial and lake sediments), some main conclusions can be summarized:

1. The solar forcing played a dominant role through the coupling of the atmospheric circulation and the cooling of the North Atlantic Ocean surface.

2. The coupling of the atmospheric circulation with the long-term North Atlantic surface temperature dominates the European climate, and this can be expressed by the NAO which controls the westerlies track changes. However, the associated high and low latitudes climatic system (i.e., SPG, STG and Hadley cell) could also exert a profound impact both in the Northern and Southern Europe hydroclimate variabilities.

3. The Lower Meuse hydrological variability is very sensitive to the climate variations, and this is meaningful for future flood risk assessments. As a rain-fed river located in the western part of the European continent, the Lower Meuse should be regarded as a more direct and sensitive recorder of changes in flood frequency in response to the variations in precipitation that are driven by patterns in atmospheric circulation over western Europe.

4. The high magnitude and more frequent floods in the Lower Meuse during the late Holocene are attributed to the anthropogenic-induced land use changes which led to a more climate-susceptible fluvial system. That is, the intense human activity in the late Holocene increased the vulnerability of the fluvial system. The consequence is that a small increase in precipitation could induce a flood with larger magnitude. Therefore, we conclude that the late Holocene flooding regime was climatic-induced but significantly intensified by anthropogenic impacts.

We propose that, combined with end member modelling, the FEI index method is a promising and meaningful method in flood reconstruction and can be used in a broad range of sedimentary settings.

Acknowledgements

I would like to take this opportunity to thank the people who supported and inspired my PhD work. First of all, I thank my promotor Prof. van Balen, who helped me to come to VU Amsterdam and this initiated my research career. Many thanks to my supervisor team members: R. van Balen, M. Prins and C. Kasse, you provided professional guidance to help make this thesis. I really enjoy the time when discussing and debating with you.

I would like to thank K. Cohen, N. van der Putten, J. van der Lubbe, F. Peeters and J. Vandenberghe for your suggestions in making the first project. Many of your reviews and help contributed to a good start. I also deliver my acknowledgements to R. Ellenkamp, R. van Elsas, M. Krasnoperov, M. Hagen and U van Buuren who provided massive laboratory support. Also to my colleagues and friends who accompanied me in the last 4 years, I will remember our time together.

Finally, I would like to thank the China Scholarship Council for providing the funding support.

Bibliography

Adams, P.N., Slingerland, R.L., Smith, N.D., 2004. Variations in natural levee morphology in anastomosed channel flood plain complexes. Geomorphology 61, 127-142. https://doi.org/10.1016/j.geomorph.2003.10.005

Ait Brahim, Y., Wassenburg, J.A., Sha, L., Cruz, F.W., Deininger, M., Sifeddine, A., Bouchaou, L., Spötl, C., Edwards, R.L., Cheng, H., 2019. North Atlantic Ice-Rafting, Ocean and Atmospheric Circulation During the Holocene: Insights From Western Mediterranean Speleothems. Geophysical Research Letters 46, 7614-7623. doi:10.1029/2019GL082405

Allen, J.R.L., 1965. A review of the origin and characteristics of recent alluvial sediments. Sedimentology 5, 89-191. https://doi.org/10.1111/j.1365-3091.1965.tb01561.x

Alley, R.B., Ágústsdóttir, A.M., 2005. The 8k event: cause and consequences of a major Holocene abrupt climate change. Quaternary Science Reviews 24, 1123-1149. https://doi.org/10.1016/j.quascirev.2004.12.004

Ammann, C.M., Joos, F., Schimel, D.S., Otto-Bliesner, B.L., Tomas, R.A., 2007. Solar influence on climate during the past millennium: Results from transient simulations with the NCAR Climate System Model. Proceedings of the National Academy of Sciences 104, 3713. 10.1073/pnas.0605064103

An, Z., Kutzbach, J.E., Prell, W.L., Porter, S.C., 2001. Evolution of Asian monsoons and phased uplift of the Himalaya–Tibetan plateau since Late Miocene times. Nature 411, 62. https://doi.org/10.1038/35075035

Ao, H., Deng, C., Dekkers, M.J., Liu, Q., 2010. Magnetic mineral dissolution in Pleistocene fluvio-lacustrine sediments, Nihewan Basin (North China). Earth and Planetary Science Letters 292, 191-200. https://doi.org/10.1016/j.epsl.2010.01.035

Armit, I., Swindles, G.T., Becker, K., Plunkett, G., Blaauw, M., 2014. Rapid climate change did not cause population collapse at the end of the European Bronze Age. Proceedings of the National Academy of Sciences 111, 17045-17049. https://doi.org/10.1073/pnas.1408028111

Arnaud, F., 2005. Discriminating Bio-Induced and Detrital Sedimentary Processes from Particle Size Distribution of Carbonates and Non-Carbonates in Hard Water Lake Sediments. Journal of Paleolimnology 34, 519-526. https://doi.org/10.1007/s10933-005-6787-1

Baker, V.R., 2008. Paleoflood hydrology: Origin, progress, prospects. Geomorphology 101, 1-13. https://doi.org/10.1016/j.geomorph.2008.05.016

Baker, V.R., Kochel, R.C., Patton, P.C., Pickup, G., 1983a. Palaeohydrologic Analysis of Holocene Flood Slack-Water Sediments, Modern and Ancient Fluvial Systems, pp. 229-239. https://doi.org/10.1002/9781444303773.ch18

Baker, V.R., Pickup, G., Polach, H.A., 1983b. Desert palaeofloods in central Australia. Nature 301, 502-504. 10.1038/301502a0

Beierle, B.D., Lamoureux, S.F., Cockburn, J.M., Spooner, I., 2002. A new method for visualizing sediment particle size distributions. Journal of Paleolimnology 27, 279-283.

Benedetti, M.M., 2003. Controls on overbank deposition in the Upper Mississippi River. Geomorphology 56, 271-290. https://doi.org/10.1016/S0169-555X(03)00156-9

Benito, G., Macklin, M.G., Panin, A., Rossato, S., Fontana, A., Jones, A.F., Machado, M.J., Matlakhova, E., Mozzi, P., Zielhofer, C., 2015a. Recurring flood distribution patterns related to short-term Holocene climatic variability. Scientific Reports 5. 10.1038/srep16398

Benito, G., Macklin, M.G., Zielhofer, C., Jones, A.F., Machado, M.J., 2015b. Holocene flooding and climate change in the Mediterranean. CATENA 130, 13-33. https://doi.org/10.1016/j.catena.2014.11.014

Benito, G., Sopeña, A., Sánchez-Moya, Y., Machado, M.a.J., Pérez-González, A., 2003. Palaeoflood record of the Tagus River (Central Spain) during the Late Pleistocene and Holocene. Quaternary Science Reviews 22, 1737-1756. https://doi.org/10.1016/S0277-3791(03)00133-1

Benito, G., Thorndycraft, V.R., 2005. Palaeoflood hydrology and its role in applied hydrological sciences. Journal of Hydrology 313, 3-15. https://doi.org/10.1016/j.jhydrol.2005.02.002

Benito, G., Thorndycraft, V.R., Rico, M., Sánchez-Moya, Y., Sopeña, A., 2008. Palaeoflood and floodplain records from Spain: Evidence for long-term climate variability and environmental changes. Geomorphology 101, 68-77. https://doi.org/10.1016/j.geomorph.2008.05.020

Berendsen, H.J.A., Stouthamer, E., 2000. Late Weichselian and Holocene palaeogeography of the Rhine–Meuse delta, The Netherlands. Palaeogeography, Palaeoclimatology, Palaeoecology 161, 311-335. https://doi.org/10.1016/S0031-0182(00)00073-0

Björck, S., Muscheler, R., Kromer, B., Andresen, C.S., Heinemeier, J., Johnsen, S.J., Conley, D., Koç, N., Spurk, M., Veski, S., 2001. High-resolution analyses of an early Holocene climate event may imply decreased solar forcing as an important climate trigger. Geology 29, 1107-1110. 10.1130/0091-7613(2001)029<1107:Hraoae>2.0.Co;2

Blaauw, M., Christen, J.A., 2011. Flexible paleoclimate age-depth models using an autoregressive gamma process. Bayesian Anal. 6, 457-474. https://doi.org/10.1214/11-BA618

Boberg, F., Lundstedt, H., 2002. Solar Wind Variations Related to Fluctuations of the North Atlantic Oscillation. Geophysical Research Letters 29, 13-11-13-14. doi:10.1029/2002GL014903

Bohncke, S., Vandenberghe, J., Huijzer, A., 1993. Periglacial environments during the Weichselian Late Glacial in the Maas valley, the Netherlands. Netherlands Journal of Geosciences-Geologie en Mijnbouw 72, 193-210.

Bohncke, S., Vandenberghe, J.E.F., Coope, R., Reiling, R., 1987. Geomorphology and palaeoecology of the Mark valley (southern Netherlands): palaeoecology, palaeohydrology and climate during the Weichselian Late Glacial. Boreas 16, 69-85. doi:10.1111/j.1502-3885.1987.tb00756.x

Bond, G., Kromer, B., Beer, J., Muscheler, R., Evans, M.N., Showers, W., Hoffmann, S., Lotti-Bond, R., Hajdas, I., Bonani, G., 2001. Persistent solar influence on North Atlantic climate during the Holocene. Science 294, 2130-2136. 10.1126/science.1065680

Bos, J.A.A., Bouma, N., Devriendt, I., van Dijk, J., Drenth, E., Exaltus, R., van Kappel, K., Kars, H., van der Laan, J., Melkert, M.J.A., Muller, A., Obdam, T., de Rijk, P.T.A., Zuidhoff, F.S., 2014. Tienduizend jaar landschaps- en bewoningsgeschiedenis in het Maasdal tussen Well en Aijen, in: edited by: Bouma, N., Muller, A., ADC ArcheoProjecten, the Netherlands,

Bos, J.A.A., van Geel, B., van der Plicht, J., Bohncke, S.J.P., 2007. Preboreal climate oscillations in Europe: Wiggle-match dating and synthesis of Dutch high-resolution multi-proxy records. Quaternary Science Reviews 26, 1927-1950. https://doi.org/10.1016/j.quascirev.2006.09.012

Bos, J.A.A., Zuidhoff, F.S., 2015. De restgeul van Well-Aijen. Een reconstructie van de vegetatieontwikkeling van het Noord-Limburgse Meusedal gedurende het Holoceen (Mesolithicum-Vroeg Romeinse tijd), in: edited by: ADC ArcheoProjecten, the Netherlands,

Boyle, J., 2004. A comparison of two methods for estimating the organic matter content of sediments. Journal of Paleolimnology 31, 125-127. https://doi.org/10.1023/B:JOPL.0000013354.67645.df

Brauer, A., Endres, C., Günter, C., Litt, T., Stebich, M., Negendank, J.F.W., 1999. High resolution sediment and vegetation responses to Younger Dryas climate change in varved lake sediments from Meerfelder Maar, Germany. Quaternary Science Reviews 18, 321-329. https://doi.org/10.1016/S0277-3791(98)00084-5

Brauer, A., Haug, G.H., Dulski, P., Sigman, D.M., Negendank, J.F.W., 2008. An abrupt wind shift in western Europe at the onset of the Younger Dryas cold period. Nature Geoscience 1, 520-523. 10.1038/ngeo263

Brierley, G.J., Ferguson, R.J., Woolfe, K.J., 1997. What is a fluvial levee? Sedimentary Geology 114, 1-9. https://doi.org/10.1016/S0037-0738(97)00114-0

Brook, G.A., Srivastava, P., Marais, E., 2006. Characteristics and OSL minimum ages of relict fluvial deposits near Sossus Vlei, Tsauchab River, Namibia, and a regional climate record for the last 30 ka. Journal of Quaternary Science 21, 347-362. https://doi.org/10.1002/jqs.977

Broothaerts, N., Verstraeten, G., Notebaert, B., Assendelft, R., Kasse, C., Bohncke, S., Vandenberghe, J., 2013. Sensitivity of floodplain geoecology to human impact: A Holocene perspective for the headwaters of the Dijle catchment, central Belgium. The Holocene 23, 1403-1414. 10.1177/0959683613489583

Buisman, J., 1995. Duizend jaar weer, wind en water in de Lage Landen / Dl. 1 : tot 1300. Van Wijnen, Franeker.

Bunnik, F., 2005a. Pollenanalyses van profielen uit het Maasdal bij Lomm, in: edited by: Utrecht (TNO-rapport NITG, 04-232-B),

Bunnik, F., 2005b. Pollenanalyses van afzettingen uit de Grensmaas (van Borgharen tot Koeweide), in: edited by: Utrecht (TNO-rapport NITG, 04-231-B),

Büntgen, U., Tegel, W., Nicolussi, K., McCormick, M., Frank, D., Trouet, V., Kaplan, J.O., Herzig, F., Heussner, K.-U., Wanner, H., Luterbacher, J., Esper, J., 2011. 2500 Years of European Climate Variability and Human Susceptibility. Science 331, 578-582. https://doi.org/10.1126/science.1197175

Chiverrell, R.C., Foster, G.C., Thomas, G.S.P., Marshall, P., Hamilton, D., 2009. Robust chronologies for landform development. Earth Surface Processes and Landforms 34, 319-328. https://doi.org/10.1002/esp.1720

Clark, P.U., Shakun, J.D., Baker, P.A., Bartlein, P.J., Brewer, S., Brook, E., Carlson, A.E., Cheng, H., Kaufman, D.S., Liu, Z., Marchitto, T.M., Mix, A.C., Morrill, C., Otto-Bliesner, B.L., Pahnke, K., Russell, J.M., Whitlock, C., Adkins, J.F., Blois, J.L., Clark, J., Colman, S.M., Curry, W.B., Flower, B.P., He, F., Johnson, T.C., Lynch-Stieglitz, J., Markgraf, V., McManus, J., Mitrovica, J.X., Moreno, P.I., Williams, J.W., 2012. Global climate evolution during the last deglaciation. Proceedings of the National Academy of Sciences 109, E1134. 10.1073/pnas.1116619109

Colin, C., Frank, N., Copard, K., Douville, E., 2010. Neodymium isotopic composition of deep-sea corals from the NE Atlantic: implications for past hydrological changes during the Holocene. Quaternary Science Reviews 29, 2509-2517. https://doi.org/10.1016/j.quascirev.2010.05.012

Copard, K., Colin, C., Henderson, G.M., Scholten, J., Douville, E., Sicre, M.A., Frank, N., 2012. Late Holocene intermediate water variability in the northeastern Atlantic as recorded by deep-sea corals. Earth and Planetary Science Letters 313-314, 34-44. https://doi.org/10.1016/j.epsl.2011.09.047

Cunningham, A.C., Wallinga, J., 2012. Realizing the potential of fluvial archives using robust OSL chronologies. Quaternary Geochronology 12, 98-106. https://doi.org/10.1016/j.quageo.2012.05.007

Czymzik, M., Adolphi, F., Muscheler, R., Mekhaldi, F., Martin-Puertas, C., Aldahan, A., Possnert, G., Brauer, A., 2016a. A varved lake sediment record of the 10Be solar activity proxy for the Lateglacial-Holocene transition. Quaternary Science Reviews 153, 31-39. https://doi.org/10.1016/j.quascirev.2016.10.007

Czymzik, M., Brauer, A., Dulski, P., Plessen, B., Naumann, R., von Grafenstein, U., Scheffler, R., 2013. Orbital and solar forcing of shifts in Mid- to Late Holocene flood intensity from varved sediments of pre-alpine Lake Ammersee (southern Germany). Quaternary Science Reviews 61, 96-110. https://doi.org/10.1016/j.quascirev.2012.11.010

Czymzik, M., Muscheler, R., Brauer, A., 2016b. Solar modulation of flood frequency in central Europe during spring and summer on interannual to multi-centennial timescales. Clim. Past 12, 799-805. 10.5194/cp-12-799-2016

De Moor, J.J.W., Kasse, C., van Balen, R., Vandenberghe, J., Wallinga, J., 2008. Human and climate impact on catchment development during the Holocene-Geul River, the Netherlands. Geomorphology 98, 316-339. https://doi.org/10.1016/j.geomorph.2006.12.033

Dearing, J.A., Foster, I.D., 1986. Lake sediments and palaeohydrological studies. Handbook of Holocene Palaeoecology and Palaeohydrology. Wiley, Chichester, 67-90.

Duller, G.A.T., 2004. Luminescence dating of quaternary sediments: recent advances. Journal of Quaternary Science 19, 183-192. https://doi.org/10.1002/jqs.809

Ellenkamp, G.R., Kubistal, P., Ruijters, M.H.P.M., Bloo, S.B.C., Ball, E.A.G., 2018. Vuursteen in lagen. Vindplaats 10 in projectgebied Ooijen-Wanssum, gemeente Horst aan de Maas. Archeologisch vooronderzoek: een waarderend veldonderzoek, in: edited by: the Netherlands,

Ely, L.L., 1997. Response of extreme floods in the southwestern United States to climatic variations in the late Holocene. Geomorphology 19, 175-201. https://doi.org/10.1016/S0169-555X(97)00014-7

Engels, S., Bakker, M.A.J., Bohncke, S.J.P., Cerli, C., Hoek, W.Z., Jansen, B., Peters, T., Renssen, H., Sachse, D., van Aken, J.M., van den Bos, V., van Geel, B., van Oostrom, R., Winkels,

T., Wolma, M., 2016. Centennial-scale lake-level lowstand at Lake Uddelermeer (The Netherlands) indicates changes in moisture source region prior to the 2.8-kyr event. The Holocene 26, 1075-1091. https://doi.org/10.1177/0959683616632890

Erkens, G., Toonen, W.H.J., Cohen, K.M., Prins, M.A., 2013. Unravelling mixed sediment signals in the floodplains of the Rhine catchment using end member modelling of grain size distributions, in: 10th International Conference on Fluvial Sedimentology, edited by: University of Leeds, 109-110.

Faegri, K., Kaland, P.E., Iversen, J., 1989. Textbook of pollen analysis. John Wiley & Sons, Ltd, p. 328.

Farrell, K.M., 1987. Sedimentology and Facies Architecture of Overbank Deposits of the Mississippi River, False River Region, Louisiana, in: Ethridge, F.G., Flores, R.M., Harvey, M.D. (Eds.), Recent Developments in Fluvial Sedimentology. SEPM Society for Sedimentary Geology.

Faust, D., Zielhofer, C., Baena Escudero, R., Diaz del Olmo, F., 2004. High-resolution fluvial record of late Holocene geomorphic change in northern Tunisia: climatic or human impact? Quaternary Science Reviews 23, 1757-1775. https://doi.org/10.1016/j.quascirev.2004.02.007

Ferguson, R.J., Brierley, G.J., 2002. Levee morphology and sedimentology along the lower Tuross River, south‐eastern Australia. Sedimentology 46, 627-648. https://doi.org/10.1046/j.1365-3091.1999.00235.x

Filgueira-Rivera, M., Smith, N.D., Slingerland, R.L., 2007. Controls on natural levée development in the Columbia River, British Columbia, Canada. Sedimentology 54, 905-919. 10.1111/j.1365-3091.2007.00865.x

Fisk, H.N., 1944. Geological investigation of the alluvial valley of the lower Mississippi River. Vicksburg.

Fisk, H.N., 1947. Fine-grained alluvial deposits and their effects on Mississippi River activity. Waterways Experiment Station, Vicksburg (Miss.).

Foulds, S.A., Macklin, M.G., 2006. Holocene land-use change and its impact on river basin dynamics in Great Britain and Ireland. Progress in Physical Geography: Earth and Environment 30, 589-604. 10.1177/0309133306071143

Foulds, S.A., Macklin, M.G., 2016. A hydrogeomorphic assessment of twenty-first century floods in the UK. Earth Surface Processes and Landforms 41, 256-270. doi:10.1002/esp.3853

Fretter, V., Graham, A., 1976. The Prosobranch Molluscs of Britain and Denmark, Part 2. Angus Graham Associates.

Fuchs, M., Owen, L.A., 2008. Luminescence dating of glacial and associated sediments: review, recommendations and future directions. Boreas 37, 636-659. https://doi.org/10.1111/j.1502-3885.2008.00052.x

Gaillard, M.J., Birks, H.H., 2007. PLANT MACROFOSSIL METHODS AND STUDIES | Paleolimnological Applications, in: Elias, S.A. (Ed.), Encyclopedia of Quaternary Science. Elsevier, Oxford, pp. 2337-2356. https://doi.org/10.1016/B0-44-452747-8/00226-X

Gerritsen, F., 2003. Local Identities: Landscape and Community in the Late Prehistoric Meuse-Demer-Scheldt Region (Amsterdam Archaeological Studies, 9). Amsterdam University Press.

Giguet-Covex, C., Arnaud, F., Enters, D., Poulenard, J., Millet, L., Francus, P., David, F., Rey, P.-J., Wilhelm, B., Delannoy, J.-J., 2012. Frequency and intensity of high-altitude floods over the last 3.5ka in northwestern French Alps (Lake Anterne). Quaternary Research 77, 12-22. https://doi.org/10.1016/j.yqres.2011.11.003

Gittenberger, E., Janssen, A.W., Kuijper, W., Kuiper, J., Meijer, T., Van der Velde, G., De Vries, J., 2004. De Nederlandse Zoetwatermollusken: Recente en fossiele weekdieren uit zoet en brak water. Nationaal Natuurhistorisch Museum Naturalis.

Glaser, R., Riemann, D., Schönbein, J., Barriendos, M., Brázdil, R., Bertolin, C., Camuffo, D., Deutsch, M., Dobrovolný, P., van Engelen, A., Enzi, S., Halíčková, M., Koenig, S.J., Kotyza, O., Limanówka, D., Macková, J., Sghedoni, M., Martin, B., Himmelsbach, I., 2010. The variability of European floods since AD 1500. Climatic Change 101, 235-256. 10.1007/s10584-010-9816-7

Glaser, R., Stangl, H., 2003. Historical floods in the Dutch Rhine Delta. Natural Hazards and Earth System Science 3, 605-613. https://doi.org/10.5194/nhess-3-605-2003

Goslin, J., Fruergaard, M., Sander, L., Gałka, M., Menviel, L., Monkenbusch, J., Thibault, N., Clemmensen, L.B., 2018. Holocene centennial to millennial shifts in North-Atlantic storminess and ocean dynamics. Scientific Reports 8, 12778. https://doi.org/10.1038/s41598-018-29949-8

Graham, A., 1988. Molluscs: Prosobranchs and Pyramidellid Gastropods: Keys and Notes for the Identification of the Species. Brill Archive.

Gray, L.J., Beer, J., Geller, M., Haigh, J.D., Lockwood, M., Matthes, K., Cubasch, U., Fleitmann, D., Harrison, G., Hood, L., Luterbacher, J., Meehl, G.A., Shindell, D., van Geel, B., White, W., 2010. Solar influence on climate. Reviews of Geophysics 48. 10.1029/2009RG000282

Grimm, E., 1992. TILIA and TILIA-GRAPH: Pollen spreadsheet and graphics programs, in: 8th International Palynological Congress. Aix-en-Provence, edited by:

Grimm, E., 2004. TGView Version 2.0. 2. Illinois State Museum, Springfield.

Haigh, J.D., 1996. The Impact of Solar Variability on Climate. Science 272, 981-984. 10.1126/science.272.5264.981

Hall, J., Arheimer, B., Borga, M., Brázdil, R., Claps, P., Kiss, A., Kjeldsen, T.R., Kriaučiūnienė, J., Kundzewicz, Z.W., Lang, M., Llasat, M.C., Macdonald, N., McIntyre, N., Mediero, L., Merz, B., Merz, R., Molnar, P., Montanari, A., Neuhold, C., Parajka, J., Perdigão, R.A.P., Plavcová, L., Rogger, M., Salinas, J.L., Sauquet, E., Schär, C., Szolgay, J., Viglione, A., Blöschl, G., 2014. Understanding flood regime changes in Europe: a state-of-the-art assessment. Hydrol. Earth Syst. Sci. 18, 2735-2772. 10.5194/hess-18-2735-2014

Harrison, S., Mighall, T., Stainforth, D.A., Allen, P., Macklin, M., Anderson, E., Knight, J., Mauquoy, D., Passmore, D., Rea, B., Spagnolo, M., Shannon, S., 2019. Uncertainty in geomorphological responses to climate change. Climatic Change 156, 69-86. 10.1007/s10584-019-02520-8

Harrison, S.P., Digerfeldt, G., 1993. European lakes as palaeohydrological and palaeoclimatic indicators. Quaternary Science Reviews 12, 233-248. https://doi.org/10.1016/0277-3791(93)90079-2

Heiri, O., Lotter, A.F., Lemcke, G., 2001. Loss on ignition as a method for estimating organic and carbonate content in sediments: reproducibility and comparability of results. Journal of Paleolimnology 25, 101-110. https://doi.org/10.1023/A:1008119611481

Hepp, J., Wüthrich, L., Bromm, T., Bliedtner, M., Schäfer, I.K., Glaser, B., Rozanski, K., Sirocko, F., Zech, R., Zech, M., 2019. How dry was the Younger Dryas? Evidence from a coupled δ2H–δ18O biomarker paleohygrometer applied to the Gemündener Maar sediments, Western Eifel, Germany. Clim. Past 15, 713-733. 10.5194/cp-15-713-2019

Herb, C., Zhang, W., Koutsodendris, A., Appel, E., Fang, X., Pross, J., 2013. Environmental implications of the magnetic record in Pleistocene lacustrine sediments of the Qaidam Basin, NE Tibetan Plateau. Quaternary international 313, 218-229. https://doi.org/10.1016/j.quaint.2013.06.015

Heunks, E., 2000. Project Zandmaas, deelgebied Ooijen, een Aanvullende Archeologische Inventarisatie (AAI), in: edited by: Amsterdam,

Hoek, W.Z., 1997. Late-glacial and early Holocene climatic events and chronology of vegetation development in the Netherlands. Vegetation History and Archaeobotany 6, 197-213. 10.1007/BF01370442

Hoek, W.Z., Bohncke, S.J.P., 2002. Climatic and environmental events over the Last Termination, as recorded in The Netherlands: a review. Netherlands Journal of Geosciences - Geologie en Mijnbouw 81, 123-137. 10.1017/S001677460002062X

Hoek, W.Z., Lammertsma, E.I., Bohncke, S.J.P., Bos, J.A.A., Bunnik, F., Kasse, C., Schokker, J., Westerhoff, W., 2017. Lateglacial and early Holocene vegetation development and fluvial system changes in the northern Meuse valley, the Netherlands: a review of palynological data. Netherlands Journal of Geosciences 96, 93-114. https://doi.org/10.1017/njg.2017.4

Hoffmann, T., Erkens, G., Gerlach, R., Klostermann, J., Lang, A., 2009. Trends and controls of Holocene floodplain sedimentation in the Rhine catchment. CATENA 77, 96-106. https://doi.org/10.1016/j.catena.2008.09.002

Houtgast, R.F., Van Balen, R.T., 2000. Neotectonics of the Roer Valley Rift System, the Netherlands. Global and Planetary Change 27, 131-146. https://doi.org/10.1016/S0921-8181(01)00063-7

Howard, A.J., Gearey, B.R., Hill, T., Fletcher, W., Marshall, P., 2009. Fluvial sediments, correlations and palaeoenvironmental reconstruction: The development of robust radiocarbon chronologies. Journal of Archaeological Science 36, 2680-2688. https://doi.org/10.1016/j.jas.2009.08.006

Huang, C.C., Pang, J., Zha, X., Zhou, Y., Su, H., Zhang, Y., Wang, H., Gu, H., 2012. Holocene palaeoflood events recorded by slackwater deposits along the lower Jinghe River valley, middle Yellow River basin, China. Journal of Quaternary Science 27, 485-493. http://dx.doi.org/10.1002/jqs.2536

Huisink, M., 1997. Late-glacial sedimentological and morphological changes in a lowland river in response to climatic change: the Maas, southern Netherlands. Journal of Quaternary Science 12, 209-223. doi:10.1002/(SICI)1099-1417(199705/06)12:3<209::AID-JQS306>3.0.CO;2-P

Huisink, M., 1999. Lateglacial river sediment budgets in the Mass valley, The Netherlands. Earth Surface Processes and Landforms 24, 93-109. https://doi.org/10.1002/(SICI)1096-9837(199902)24:2%3C93::AID-ESP940%3E3.0.CO;2-R

Hurrell, J.W., Kushnir, Y., Visbeck, M., 2001. The North Atlantic Oscillation. Science 291, 603. 10.1126/science.1058761

Ineson, S., Scaife, A.A., Knight, J.R., Manners, J.C., Dunstone, N.J., Gray, L.J., Haigh, J.D., 2011. Solar forcing of winter climate variability in the Northern Hemisphere. Nature Geosci 4, 753-757. http://www.nature.com/ngeo/journal/v4/n11/abs/ngeo1282.html#supplementary-information

IPCC, 2019. IPCC Special Report on the Ocean and Cryosphere in a Changing Climate, in: edited by: Pörtner, H.-O., Roberts, D.C., Masson-Delmotte, V., Zhai, P., Tignor, M., Poloczanska, E., Mintenbeck, K., Alegría, A., Nicolai, M., Okem, A., Petzold, J., Rama, B., Weyer, N.M.,

Isarin, R.F.B., Bohncke, S.J.P., 1999. Mean July Temperatures during the Younger Dryas in Northwestern and Central Europe as Inferred from Climate Indicator Plant Species. Quaternary Research 51, 158-173. https://doi.org/10.1006/qres.1998.2023

Isarin, R.F.B., Rensink, E., Ellenkamp, G.R., Heunks, E., 2017. Of Meuse and Man: the geomorphogenetic and archaeological predictive maps of the Dutch Meuse valley. Netherlands Journal of Geosciences 96, 183-196. https://doi.org/10.1017/njg.2017.5

Isarin, R.F.B., Renssen, H., Koster, E.A., 1997. Surface wind climate during the Younger Dryas in Europe as inferred from aeolian records and model simulations. Palaeogeography, Palaeoclimatology, Palaeoecology 134, 127-148. https://doi.org/10.1016/S0031-0182(96)00155-1

Isarin, R.F.B., Renssen, H., Vandenberghe, J., 1998. The impact of the North Atlantic Ocean on the Younger Dryas climate in northwestern and central Europe. Journal of Quaternary Science 13, 447-453. doi:10.1002/(SICI)1099-1417(1998090)13:5<447::AID-JQS402>3.0.CO;2-B

Ishii, Y., Hori, K., Momohara, A., 2017. Middle to late Holocene flood activity estimated from loss on ignition of peat in the Ishikari lowland, northern Japan. Global and Planetary Change 153, 1-15. https://doi.org/10.1016/j.gloplacha.2017.04.004

Iversen, J., 1973. The development of Denmark's nature since the last glacial. C.A. Reitzels Forlag, København.

Johnston, G.H., David, S.R., Edmonds, D.A., 2019. Connecting fluvial levee deposition to flood-basin hydrology. Journal of Geophysical Research: Earth Surface 0. 10.1029/2019JF005014

Kalis, A.J., Merkt, J., Wunderlich, J., 2003. Environmental changes during the Holocene climatic optimum in central Europe - human impact and natural causes. Quaternary Science Reviews 22, 33-79. https://doi.org/10.1016/S0277-3791(02)00181-6

Kasse, C., 2002. Sandy aeolian deposits and environments and their relation to climate during the Last Glacial Maximum and Lateglacial in northwest and central Europe. Progress in Physical Geography: Earth and Environment 26, 507-532. 10.1191/0309133302pp350ra

Kasse, C., Vandenberghe, J., Bohncke, S.J.P., 1995. Climatic change and fluvial dynamics of the Maas during the Late Weichselian and Early Holocene, in: B., F., Vandenberghe, J., Kasse, C., Bohncke, S.J.P., B., G. (Eds.), European river activity and climatic change during the Lateglacial and early Holocene, pp. 123-150.

Knox, J.C., 2006. Floodplain sedimentation in the Upper Mississippi Valley: Natural versus human accelerated. Geomorphology 79, 286-310. https://doi.org/10.1016/j.geomorph.2006.06.031

Kochel, R.C., Baker, V.R., 1982. Paleoflood Hydrology. Science 215, 353. https://doi.org/10.1126/science.215.4531.353

Kodera, K., 2002. Solar cycle modulation of the North Atlantic Oscillation: Implication in the spatial structure of the NAO. Geophysical Research Letters 29, 59-51-59-54. doi:10.1029/2001GL014557

Kodera, K., Kuroda, Y., 2005. A possible mechanism of solar modulation of the spatial structure of the North Atlantic Oscillation. Journal of Geophysical Research: Atmospheres 110. doi:10.1029/2004JD005258

Kolstrup, E., 2007. Lateglacial older and younger coversand in northwest Europe: chronology and relation to climate and vegetation. Boreas 36, 65-75. doi:10.1111/j.1502-3885.2007.tb01181.x

Konert, M., Vandenberghe, J.E.F., 1997. Comparison of laser grain size analysis with pipette and sieve analysis: a solution for the underestimation of the clay fraction. Sedimentology 44, 523-535. https://doi.org/10.1046/j.1365-3091.1997.d01-38.x

Lamb, H.H., 2002. Climate, history and the modern world. Routledge.

Lee, S.H., Lee, Y.I., Yoon, H.I., Yoo, K.-C., 2008. East Asian monsoon variation and climate changes in Jeju Island, Korea, during the latest Pleistocene to early Holocene. Quaternary Research 70, 265-274. https://doi.org/10.1016/j.yqres.2008.04.014

Leng, M., Roberts, N., Reed, J., Sloane, H., 1999. Late Quaternary climatic and limnological variations based on carbon and oxygen isotope data from authigenic and ostracod carbonate in the Konya Basin, Turkey. Journal of Paleolimnology 22, 187-204.

Leng, M.J., Marshall, J.D., 2004. Palaeoclimate interpretation of stable isotope data from lake sediment archives. Quaternary Science Reviews 23, 811-831. https://doi.org/10.1016/j.quascirev.2003.06.012

Lenton, T.M., Livina, V.N., Dakos, V., Scheffer, M., 2012. Climate bifurcation during the last deglaciation? Clim. Past 8, 1127-1139. 10.5194/cp-8-1127-2012

Lim, J., Lee, J.-Y., Hong, S.-S., Kim, J.-Y., 2013. Late Holocene flooding records from the floodplain deposits of the Yugu River, South Korea. Geomorphology 180-181, 109-119. https://doi.org/10.1016/j.geomorph.2012.09.010

Litt, T., Brauer, A., Goslar, T., Merkt, J., Bałaga, K., Müller, H., Ralska-Jasiewiczowa, M., Stebich, M., Negendank, J.F., 2001. Correlation and synchronisation of Lateglacial continental sequences in northern central Europe based on annually laminated lacustrine sediments. Quaternary Science Reviews 20, 1233-1249. https://doi.org/10.1016/S0277-3791(00)00149-9

Lockwood, M., Bell, C., Woollings, T., Harrison, R.G., Gray, L.J., Haigh, J.D., 2010. Top-down solar modulation of climate: evidence for centennial-scale change. Environmental Research Letters 5, 034008. 10.1088/1748-9326/5/3/034008

Lu, J., Vecchi, G.A., Reichler, T., 2007. Expansion of the Hadley cell under global warming. Geophysical Research Letters 34.

Macklin, M.G., Benito, G., Gregory, K.J., Johnstone, E., Lewin, J., Michczyńska, D.J., Soja, R., Starkel, L., Thorndycraft, V.R., 2006. Past hydrological events reflected in the Holocene fluvial record of Europe. CATENA 66, 145-154. https://doi.org/10.1016/j.catena.2005.07.015

Macklin, M.G., Johnstone, E., Lewin, J., 2005. Pervasive and long-term forcing of Holocene river instability and flooding in Great Britain by centennial-scale climate change. The Holocene 15, 937-943. https://doi.org/10.1191/0959683605hl867ft

Macklin, M.G., Jones, A.F., Lewin, J., 2010. River response to rapid Holocene environmental change: evidence and explanation in British catchments. Quaternary Science Reviews 29, 1555-1576. https://doi.org/10.1016/j.quascirev.2009.06.010

Macklin, M.G., Lewin, J., Jones, A.F., 2013. River entrenchment and terrace formation in the UK Holocene. Quaternary Science Reviews 76, 194-206. https://doi.org/10.1016/j.quascirev.2013.05.026

Macklin, M.G., Lewin, J., Woodward, J.C., 2012. The fluvial record of climate change. Philos Trans A Math Phys Eng Sci 370, 2143-2172. https://doi.org/10.1098/rsta.2011.0608

Macklin, M.G., Toonen, W.H.J., Woodward, J.C., Williams, M.A.J., Flaux, C., Marriner, N., Nicoll, K., Verstraeten, G., Spencer, N., Welsby, D., 2015. A new model of river dynamics, hydroclimatic change and human settlement in the Nile Valley derived from meta-analysis of the

Holocene fluvial archive. Quaternary Science Reviews 130, 109-123. https://doi.org/10.1016/j.quascirev.2015.09.024

Magny, M., 1993. Solar Influences on Holocene Climatic Changes Illustrated by Correlations between Past Lake-Level Fluctuations and the Atmospheric 14C Record. Quaternary Research 40, 1-9. https://doi.org/10.1006/qres.1993.1050

Magny, M., 2004. Holocene climate variability as reflected by mid-European lake-level fluctuations and its probable impact on prehistoric human settlements. Quaternary International 113, 65-79. https://doi.org/10.1016/S1040-6182(03)00080-6

Magny, M., Bégeot, C., Guiot, J., Peyron, O., 2003. Contrasting patterns of hydrological changes in Europe in response to Holocene climate cooling phases. Quaternary Science Reviews 22, 1589-1596. https://doi.org/10.1016/S0277-3791(03)00131-8

Martin-Puertas, C., Matthes, K., Brauer, A., Muscheler, R., Hansen, F., Petrick, C., Aldahan, A., Possnert, G., van Geel, B., 2012. Regional atmospheric circulation shifts induced by a grand solar minimum. Nature Geoscience 5, 397-401. 10.1038/ngeo1460

Mauquoy, D., Yeloff, D., Van Geel, B., Charman, D.J., Blundell, A., 2008. Two decadally resolved records from north‐west European peat bogs show rapid climate changes associated with solar variability during the mid–late Holocene. Journal of Quaternary Science: Published for the Quaternary Research Association 23, 745-763.

Mayewski, P.A., Maasch, K.A., 2006. Recent warming inconsistent with natural association between temperature and atmospheric circulation over the last 2000 years. Clim. Past Discuss. 2006, 327-355. 10.5194/cpd-2-327-2006

Mayewski, P.A., Meeker, L.D., Twickler, M.S., Whitlow, S., Yang, Q., Lyons, W.B., Prentice, M., 1997. Major features and forcing of high-latitude northern hemisphere atmospheric circulation using a 110,000-year-long glaciochemical series. Journal of Geophysical Research: Oceans 102, 26345-26366. 10.1029/96JC03365

Mellström, A., Van der Putten, N., Muscheler, R., De Jong, R., Björck, S., 2015. A shift towards wetter and windier conditions in southern Sweden around the prominent solar minimum 2750 cal a BP. Journal of Quaternary Science 30, 235-244.

Meyers, P.A., Teranes, J.L., 2002. Sediment organic matter, Tracking environmental change using lake sediments. Springer, pp. 239-269.

Minderhoud, P.S.J., Cohen, K.M., Toonen, W.H.J., Erkens, G., Hoek, W.Z., 2016. Improving age-depth models of fluvio-lacustrine deposits using sedimentary proxies for accumulation rates. Quaternary Geochronology 33, 35-45. https://doi.org/10.1016/j.quageo.2016.01.001

Moore, J., Grinsted, A., Jevrejeva, S., 2006. Is there evidence for sunspot forcing of climate at multi-year and decadal periods? Geophysical Research Letters 33. doi:10.1029/2006GL026501

Moore, P.D., Webb, J.A., Collison, M.E., 1991. Pollen analysis. Blackwell scientific publications.

Muñoz, A., Bartolomé, M., Muñoz, A., Sancho, C., Moreno, A., Hellstrom, J.C., Osácar, M.C., Cacho, I., 2015. Solar influence and hydrological variability during the Holocene from a speleothem annual record (Molinos Cave, NE Spain). Terra Nova 27, 300-311. doi:10.1111/ter.12160

Munoz, S.E., Giosan, L., Therrell, M.D., Remo, J.W.F., Shen, Z., Sullivan, R.M., Wiman, C., O'Donnell, M., Donnelly, J.P., 2018. Climatic control of Mississippi River flood hazard amplified by river engineering. Nature 556, 95. https://doi.org/10.1038/nature26145

Munoz, S.E., Gruley, K.E., Massie, A., Fike, D.A., Schroeder, S., Williams, J.W., 2015. Cahokia's emergence and decline coincided with shifts of flood frequency on the Mississippi River. Proceedings of the National Academy of Sciences 112, 6319. 10.1073/pnas.1501904112

Muschitiello, F., Pausata, F.S.R., Watson, J.E., Smittenberg, R.H., Salih, A.A.M., Brooks, S.J., Whitehouse, N.J., Karlatou-Charalampopoulou, A., Wohlfarth, B., 2015. Fennoscandian freshwater control on Greenland hydroclimate shifts at the onset of the Younger Dryas. Nature Communications 6, 8939. 10.1038/ncomms9939

Nesje, A., Dahl, S.O., Matthews, J.A., Berrisford, M.S., 2001. A ~4500 yr record of river floods obtained from a sediment core in Lake Atnsjøen, eastern Norway. Journal of Paleolimnology 25, 329-342. 10.1023/A:1011197507174

Notebaert, B., Verstraeten, G., 2010. Sensitivity of West and Central European river systems to environmental changes during the Holocene: A review. Earth-Science Reviews 103, 163-182. https://doi.org/10.1016/j.earscirev.2010.09.009

Notebaert, B., Verstraeten, G., Ward, P., Renssen, H., Van Rompaey, A., 2011. Modeling the sensitivity of sediment and water runoff dynamics to Holocene climate and land use changes at the catchment scale. Geomorphology 126, 18-31. https://doi.org/10.1016/j.geomorph.2010.08.016

Olsen, J., Anderson, N.J., Knudsen, M.F., 2012. Variability of the North Atlantic Oscillation over the past 5,200 years. Nature Geosci 5, 808-812. 10.1038/ngeo1589

Orme, L.C., Charman, D.J., Reinhardt, L., Johnsen, S.J., Mitchell, F.J.G., Stenfanini, B.S., Barkwith, A., Ellis, M.A., Grosvenor, M., 2017. Past changes in the North Atlantic storm track driven by insolation and sea-ice forcing. Geology 45, 335-338. 10.1130/G38521.1

Ortega, P., Lehner, F., Swingedouw, D., Masson-Delmotte, V., Raible, C.C., Casado, M., Yiou, P., 2015. A model-tested North Atlantic Oscillation reconstruction for the past millennium. Nature 523, 71-74. 10.1038/nature14518

Paterson, G.A., Heslop, D., 2015. New methods for unmixing sediment grain size data. Geochemistry, Geophysics, Geosystems 16, 4494-4506. https://doi.org/10.1002/2015GC006070

Peña, J., Schulte, L., Badoux, A., Barriendos, M., Barrera-Escoda, A., 2014. Influence of solar forcing, climate variability and atmospheric circulation patterns on summer floods in Switzerland. Hydrology & Earth System Sciences Discussions 11.

Peng, F., Kasse, C., Prins, M.A., Ellenkamp, R., Krasnoperov, M.Y., van Balen, R.T., 2020. Paleoflooding reconstruction from Holocene levee deposits in the Lower Meuse valley, the Netherlands. Geomorphology 352, 107002. https://doi.org/10.1016/j.geomorph.2019.107002

Peng, F., Prins, M.A., Kasse, C., Cohen, K.M., Van der Putten, N., van der Lubbe, J., Toonen, W.H.J., van Balen, R.T., 2019. An improved method for paleoflood reconstruction and flooding phase identification, applied to the Meuse River in the Netherlands. Global and Planetary Change 177, 213-224. https://doi.org/10.1016/j.gloplacha.2019.04.006

Peng, F., van Balen, R., Beets, C., Kasse, C., Prins Maarten, A., Van der Putten, N., Troelstra, S., Woolderink, H.A.G., Van der Woude, J., submitted. Rapid flood intensification and environmental response of the Lower Meuse during the Allerød-Younger Dryas climate oscillation. Submitted to Geomorpholoy.

Phillips, J.D., 2010. Relative Importance of Intrinsic, Extrinsic, and Anthropic Factors in the Geomorphic Zonation of the Trinity River, Texas. Journal of the American Water Resources Association 46, 807-823. https://doi.org/10.1111/j.1093-474X.2010.00457.x

Pierik, H.J., Stouthamer, E., Cohen, K.M., 2017. Natural levee evolution in the Rhine-Meuse delta, the Netherlands, during the first millennium CE. Geomorphology 295, 215-234. https://doi.org/10.1016/j.geomorph.2017.07.003

Prasad, S., Brauer, A., Rein, B., Negendank, J.F.W., 2006. Rapid climate change during the early Holocene in western Europe and Greenland. The Holocene 16, 153-158. 10.1191/0959683606hl916ft

Prasad, S., Witt, A., Kienel, U., Dulski, P., Bauer, E., Yancheva, G., 2009. The 8.2 ka event: Evidence for seasonal differences and the rate of climate change in western Europe. Global and Planetary Change 67, 218-226. https://doi.org/10.1016/j.gloplacha.2009.03.011

Prins, M.A., 1999. Pelagic, hemipelagic and turbidite deposition in the Arabian Sea during the late Quaternary: unravelling the signals of eolian and fluvial sediment supply as functions of tectonics, sea-level and climatic change by means of end-member modelling of siliciclastic grain-size distributions, in: edited by: Universiteit Utrecht, the Netherlands,

Prins, M.A., Postma, G., Weltje, G.J., 2000. Controls on terrigenous sediment supply to the Arabian Sea during the late Quaternary: the Makran continental slope. Marine Geology 169, 351-371. https://doi.org/10.1016/S0025-3227(00)00087-6

Prins, M.A., Vriend, M., Nugteren, G., Vandenberghe, J., Lu, H., Zheng, H., Jan Weltje, G., 2007. Late Quaternary aeolian dust input variability on the Chinese Loess Plateau: inferences from unmixing of loess grain-size records. Quaternary Science Reviews 26, 230-242. https://doi.org/10.1016/j.quascirev.2006.07.002

Prins, M.A., Weltje, G.J., 1999. End-member modeling of siliciclastic grain-size distributions: The late Quaternary record of aeolian and fluvial sediment supply to the Arabian Sea and its

paleoclimatic significance, in: Harbaugh, J. (Ed.), Numerical experiments in stratigraphy: Recent advances in stratigraphic and sedimentologic computer simulations. Society for Sedimentary Geology, pp. 91-111.

Rasmussen, S.O., Andersen, K.K., Svensson, A.M., Steffensen, J.P., Vinther, B.M., Clausen, H.B., Siggaard-Andersen, M.-L., Johnsen, S.J., Larsen, L.B., Dahl-Jensen, D., Bigler, M., Röthlisberger, R., Fischer, H., Goto-Azuma, K., Hansson, M.E., Ruth, U., 2006. A new Greenland ice core chronology for the last glacial termination. Journal of Geophysical Research: Atmospheres 111. 10.1029/2005jd006079

Rasmussen, S.O., Bigler, M., Blockley, S.P., Blunier, T., Buchardt, S.L., Clausen, H.B., Cvijanovic, I., Dahl-Jensen, D., Johnsen, S.J., Fischer, H., Gkinis, V., Guillevic, M., Hoek, W.Z., Lowe, J.J., Pedro, J.B., Popp, T., Seierstad, I.K., Steffensen, J.P., Svensson, A.M., Vallelonga, P., Vinther, B.M., Walker, M.J.C., Wheatley, J.J., Winstrup, M., 2014. A stratigraphic framework for abrupt climatic changes during the Last Glacial period based on three synchronized Greenland ice-core records: refining and extending the INTIMATE event stratigraphy. Quaternary Science Reviews 106, 14-28. https://doi.org/10.1016/j.quascirev.2014.09.007

Reimer, P.J., Bard, E., Bayliss, A., Beck, J.W., Blackwell, P.G., Ramsey, C.B., Buck, C.E., Cheng, H., Edwards, R.L., Friedrich, M., Grootes, P.M., Guilderson, T.P., Haflidason, H., Hajdas, I., Hatté, C., Heaton, T.J., Hoffmann, D.L., Hogg, A.G., Hughen, K.A., Kaiser, K.F., Kromer, B., Manning, S.W., Niu, M., Reimer, R.W., Richards, D.A., Scott, E.M., Southon, J.R., Staff, R.A., Turney, C.S.M., van der Plicht, J., 2013. IntCal13 and Marine13 Radiocarbon Age Calibration Curves 0–50,000 Years cal BP. Radiocarbon 55, 1869-1887. https://doi.org/10.2458/azu_js_rc.55.16947

Renssen, H., Lautenschlager, M., Schuurmans, C.J.E., 1996. The atmospheric winter circulation during the Younger Dryas stadial in the Atlantic/European sector. Climate Dynamics 12, 813-824. 10.1007/s003820050145

Renssen, H., Seppä, H., Heiri, O., Roche, D.M., Goosse, H., Fichefet, T., 2009. The spatial and temporal complexity of the Holocene thermal maximum. Nature Geoscience 2, 411-414. 10.1038/ngeo513

Roberts, N., Jones, M.D., Benkaddour, A., Eastwood, W.J., Filippi, M.L., Frogley, M.R., Lamb, H.F., Leng, M.J., Reed, J.M., Stein, M., Stevens, L., Valero-Garcés, B., Zanchetta, G., 2008. Stable isotope records of Late Quaternary climate and hydrology from Mediterranean lakes: the ISOMED synthesis. Quaternary Science Reviews 27, 2426-2441. https://doi.org/10.1016/j.quascirev.2008.09.005

Ruijters, M.H.P.M., van Dijk, X.C.C., Ellenkamp, G.R., Tichelman, G., 2017. Afgedekte ruggen opgezocht. Onderzoeksgebied Ooijen-Wanssum in de gemeenten Venray en Horst aan de Maas; archeologisch vooronderzoek: een proefsleuvenonderzoek, in: edited by: the Netherlands,

Sabatier, P., Dezileau, L., Colin, C., Briqueu, L., Bouchette, F., Martinez, P., Siani, G., Raynal, O., Von Grafenstein, U., 2012. 7000 years of paleostorm activity in the NW Mediterranean Sea in response to Holocene climate events. Quaternary Research 77, 1-11. https://doi.org/10.1016/j.yqres.2011.09.002

Santisteban, J.I., Mediavilla, R., López-Pamo, E., Dabrio, C.J., Zapata, M.B.R., García, M.J.G., Castaño, S., Martínez-Alfaro, P.E., 2004. Loss on ignition: a qualitative or quantitative method for organic matter and carbonate mineral content in sediments? Journal of Paleolimnology 32, 287-299. https://doi.org/10.1023/B:JOPL.0000042999.30131.5b

Schenk, F., Väliranta, M., Muschitiello, F., Tarasov, L., Heikkilä, M., Björck, S., Brandefelt, J., Johansson, A.V., Näslund, J.-O., Wohlfarth, B., 2018. Warm summers during the Younger Dryas cold reversal. Nature Communications 9, 1634. 10.1038/s41467-018-04071-5

Schulte, L., Wetter, O., Wilhelm, B., Peña, J.C., Amann, B., Wirth, S.B., Carvalho, F., Gómez-Bolea, A., 2019. Integration of multi-archive datasets for the development of a four-dimensional paleoflood model of alpine catchments. Global and Planetary Change 180, 66-88. https://doi.org/10.1016/j.gloplacha.2019.05.011

Schwertmann, U., Fanning, D.S., 1976. Iron-manganese Concretions in Hydrosequences of Soils in Loess in Bavaria1. Soil Science Society of America Journal 40, 731-738. https://doi:10.2136/sssaj1976.03615995004000050034x

Shang, Y., Beets, C.J., Tang, H., Prins, M.A., Lahaye, Y., van Elsas, R., Sukselainen, L., Kaakinen, A., 2016. Variations in the provenance of the late Neogene Red Clay deposits in northern China. Earth and Planetary Science Letters 439, 88-100. https://doi.org/10.1016/j.epsl.2016.01.031

Shindell, D.T., Schmidt, G.A., Mann, M.E., Rind, D., Waple, A., 2001. Solar Forcing of Regional Climate Change During the Maunder Minimum. Science 294, 2149. 10.1126/science.1064363

Smith, N.D., Cross, T.A., Dufficy, J.P., Clough, S.R., 1989. Anatomy of an avulsion. Sedimentology 36, 1-23. https://doi.org/10.1111/j.1365-3091.1989.tb00817.x

Sorrel, P., Debret, M., Billeaud, I., Jaccard, S.L., McManus, J.F., Tessier, B., 2012. Persistent non-solar forcing of Holocene storm dynamics in coastal sedimentary archives. Nature Geoscience 5, 892-896. 10.1038/ngeo1619

Stam, M.H., 2002. Effects of Land-Use and Precipitation Changes on Floodplain Sedimentation in the Nineteenth and Twentieth Centuries (Geul River, The Netherlands), in: Martini, I.P., Baker, V.R., Garzón, G. (Eds.), Flood and Megaflood Processes and Deposits. Blackwell Publishing Ltd., pp. 251-267. https://doi.org/10.1002/9781444304299.ch14

Starkel, L., Michczyńska, D.J., Gębica, P., Kiss, T., Panin, A., Perşoiu, I., 2015. Climatic fluctuations reflected in the evolution of fluvial systems of Central-Eastern Europe (60–8 ka cal BP). Quaternary International 388, 97-118. https://doi.org/10.1016/j.quaint.2015.04.017

Steinhilber, F., Beer, J., Fröhlich, C., 2009. Total solar irradiance during the Holocene. Geophysical Research Letters 36. 10.1029/2009GL040142

Streeter, D., Hart-Davies, C., Hardcastle, A., Harper, L., Cole, F., 2016. Collins Wild Flower Guide. HarperCollins Publishers Limited.

Stuiver, M., 1970. Oxygen and carbon isotope ratios of fresh-water carbonates as climatic indicators. Journal of Geophysical Research (1896-1977) 75, 5247-5257. doi:10.1029/JC075i027p05247

Stuiver, M., Braziunas, T.F., 1993. Sun, ocean, climate and atmospheric 14CO2: an evaluation of causal and spectral relationships. the holocene 3, 289-305.

Stuiver, M., Braziunas, T.F., 1998. Anthropogenic and solar components of hemispheric 14C. Geophysical Research Letters 25, 329-332.

Stuiver, M., Grootes, P.M., 2000. GISP2 Oxygen Isotope Ratios. Quaternary Research 53, 277-284. 10.1006/qres.2000.2127

Tebbens, L.A., Veldkamp, A., Westerhoff, W., Kroonenberg, S.B., 1999. Fluvial incision and channel downcutting as a response to Late-glacial and Early Holocene climate change: the lower reach of the River Meuse (Maas), The Netherlands. Journal of Quaternary Science 14, 59-75. https://doi.org/10.1002/(SICI)1099-1417(199902)14:1%3C59::AID-JQS408%3E3.0.CO;2-Z

Teranes, J.L., McKenzie, J.A., 2001. Lacustrine oxygen isotope record of 20th-century climate change in central EuropeL evaluation of climatic controls on oxygen isotopes in precipitation. Journal of Paleolimnology 26, 131-146. 10.1023/A:1011175701502

Teunissen, D., 1983. The development of the landscape of the nature reserve De Hamert and its environs in the Northern part of the province of Limburg, The Netherlands. Geologie en Mijnbouw 62, 8.

Thiéblemont, R., Matthes, K., Omrani, N.-E., Kodera, K., Hansen, F., 2015. Solar forcing synchronizes decadal North Atlantic climate variability. Nature Communications 6, 8268. 10.1038/ncomms9268

Thompson, R., Battarbee, R.W., O'Sullivan, P.E., Oldfield, F., 1975. Magnetic susceptibility of lake sediments. Limnology and Oceanography 20, 687-698. https://doi.org/10.4319/lo.1975.20.5.0687

Thornalley, D.J.R., Elderfield, H., McCave, I.N., 2009. Holocene oscillations in temperature and salinity of the surface subpolar North Atlantic. Nature 457, 711-714. 10.1038/nature07717

Tipping, R., Davies, A., McCulloch, R., Tisdall, E., 2008. Response to late Bronze Age climate change of farming communities in north east Scotland. Journal of Archaeological Science 35, 2379-2386. https://doi.org/10.1016/j.jas.2008.03.008

Toonen, W.H.J., 2013. A Holocene flood record of the Lower Rhine (Ph.D. thesis), in: edited by: Utrecht University, 204.

Toonen, W.H.J., 2015. Flood frequency analysis and discussion of non-stationarity of the Lower Rhine flooding regime (AD 1350–2011): Using discharge data, water level measurements, and historical records. Journal of Hydrology 528, 490-502. https://doi.org/10.1016/j.jhydrol.2015.06.014

Toonen, W.H.J., Foulds, S.A., Macklin, M.G., Lewin, J., 2017. Events, episodes, and phases: Signal from noise in flood-sediment archives. Geology 45, 331-334. https://doi.org/10.1130/G38540.1

Toonen, W.H.J., Kleinhans, M.G., Cohen, K.M., 2012. Sedimentary architecture of abandoned channel fills. Earth Surface Processes and Landforms 37, 459-472. https://doi.org/10.1002/esp.3189

Toonen, W.H.J., Middelkoop, H., Konijnendijk, T.Y.M., Macklin, M.G., Cohen, K.M., 2016. The influence of hydroclimatic variability on flood frequency in the Lower Rhine. Earth Surface Processes and Landforms 41, 1266-1275. doi:10.1002/esp.3953

Toonen, W.H.J., Munoz, S.E., Cohen, K.M., Macklin, M.G., 2020. High-Resolution Sedimentary Paleoflood Records in Alluvial River Environments: A Review of Recent Methodological Advances and Application to Flood Hazard Assessment, in: Herget, J., Fontana, A. (Eds.), Palaeohydrology: Traces, Tracks and Trails of Extreme Events. Springer International Publishing, Cham, pp. 213-228. 10.1007/978-3-030-23315-0_11

Toonen, W.H.J., Winkels, T.G., Cohen, K.M., Prins, M.A., Middelkoop, H., 2015a. Lower Rhine historical flood magnitudes of the last 450 years reproduced from grain-size measurements of flood deposits using End Member Modelling. CATENA 130, 69-81. https://doi.org/10.1016/j.catena.2014.12.004

Toonen, W.H.J., Winkels, T.G., Cohen, K.M., Prins, M.A., Middelkoop, H., 2015b. Lower Rhine historical flood magnitudes of the last 450years reproduced from grain-size measurements of flood deposits using End Member Modelling. CATENA 130, 69-81. https://doi.org/10.1016/j.catena.2014.12.004

Törnqvist, T.E., Bridge, J.S., 2002. Spatial variation of overbank aggradation rate and its influence on avulsion frequency. Sedimentology 49, 891-905. 10.1046/j.1365-3091.2002.00478.x

Trouet, V., Esper, J., Graham, N.E., Baker, A., Scourse, J.D., Frank, D.C., 2009. Persistent Positive North Atlantic Oscillation Mode Dominated the Medieval Climate Anomaly. Science 324, 78. 10.1126/science.1166349

Usoskin, I.G., Solanki, S., Kovaltsov, G., 2007. Grand minima and maxima of solar activity: new observational constraints. Astronomy & Astrophysics 471, 301-309.

Van Balen, R.T., Houtgast, R.F., Cloetingh, S.A.P.L., 2005. Neotectonics of The Netherlands: a review. Quaternary Science Reviews 24, 439-454. https://doi.org/10.1016/j.quascirev.2004.01.011

Van den Bos, V., Engels, S., Bohncke, S.J.P., Cerli, C., Jansen, B., Kalbitz, K., Peterse, F., Renssen, H., Sachse, D., 2018. Late Holocene changes in vegetation and atmospheric circulation at Lake Uddelermeer (The Netherlands) reconstructed using lipid biomarkers and compound‐specific δ D analysis. Journal of Quaternary Science 33, 100-111. https://doi.org/10.1002/jqs.3006

Van Geel, B., Buurman, J., Waterbolk, H.T., 1996. Archaeological and palaeoecological indications of an abrupt climate change in The Netherlands, and evidence for climatological teleconnections around 2650 BP. Journal of Quaternary Science 11, 451-460. https://doi.org/10.1002/(SICI)1099-1417(199611/12)11:6%3C451::AID-JQS275%3E3.0.CO;2-9

Van Geel, B., Coope, G.R., Van Der Hammen, T., 1989. Palaeoecology and stratigraphy of the lateglacial type section at Usselo (the Netherlands). Review of Palaeobotany and Palynology 60, 25-129. https://doi.org/10.1016/0034-6667(89)90072-9

Van Geel, B., Heijnis, H., Charman, D.J., Thompson, G., Engels, S., 2014. Bog burst in the eastern Netherlands triggered by the 2.8 kyr BP climate event. The Holocene 24, 1465-1477. 10.1177/0959683614544066

Van Geel, B., Van Der Plicht, J., Kilian, M.R., Klaver, E.R., Kouwenberg, J.H.M., Renssen, H., Reynaud-Farrera, I., Waterbolk, H.T., 1998. The Sharp Rise of Δ14C ca. 800 cal BC: Possible Causes, Related Climatic Teleconnections and the Impact on Human Environments. Radiocarbon 40, 535-550. https://doi.org/10.1017/S0033822200018403

Van Hateren, J.A., Prins, M.A., van Balen, R.T., 2018. On the genetically meaningful decomposition of grain-size distributions: A comparison of different end-member modelling algorithms. Sedimentary Geology 375, 49-71. https://doi.org/10.1016/j.sedgeo.2017.12.003

Van Huissteden, J., Kasse, C., 2001. Detection of rapid climate change in Last Glacial fluvial successions in The Netherlands. Global and Planetary Change 28, 319-339. https://doi.org/10.1016/S0921-8181(00)00082-5

Van Leeuwen, M., 2014. Response of the Maas River to climatic changes of the Late Pleniglacial to Holocene, in: edited by: Vrije Universiteit Amsterdam, 73.

Vandenberghe, J., Kasse, C., Bohncke, S., Kozarski, S., 1994. Climate-related river activity at the Weichselian-Holocene transition: a comparative study of the Warta and Maas rivers. Terra Nova 6, 476-485. doi:10.1111/j.1365-3121.1994.tb00891.x

Vandenberghe, J., Lu, H., Sun, D., van Huissteden, J., Konert, M., 2004. The late Miocene and Pliocene climate in East Asia as recorded by grain size and magnetic susceptibility of the Red Clay deposits (Chinese Loess Plateau). Palaeogeography, Palaeoclimatology, Palaeoecology 204, 239-255. https://doi.org/10.1016/S0031-0182(03)00729-6

Vonmoos, M., Beer, J., Muscheler, R., 2006. Large variations in Holocene solar activity: Constraints from 10Be in the Greenland Ice Core Project ice core. Journal of Geophysical Research: Space Physics 111. doi:10.1029/2005JA011500

Wanner, H., Beer, J., Bütikofer, J., Crowley, T.J., Cubasch, U., Flückiger, J., Goosse, H., Grosjean, M., Joos, F., Kaplan, J.O., Küttel, M., Müller, S.A., Prentice, I.C., Solomina, O., Stocker, T.F., Tarasov, P., Wagner, M., Widmann, M., 2008. Mid- to Late Holocene climate change: an overview. Quaternary Science Reviews 27, 1791-1828. https://doi.org/10.1016/j.quascirev.2008.06.013

Wanner, H., Brönnimann, S., Casty, C., Gyalistras, D., Luterbacher, J., Schmutz, C., Stephenson, D.B., Xoplaki, E., 2001. North Atlantic Oscillation–concepts and studies. Surveys in geophysics 22, 321-381.

Ward, P.J., Renssen, H., Aerts, J.C.J.H., van Balen, R.T., Vandenberghe, J., 2008. Strong increases in flood frequency and discharge of the River Meuse over the late Holocene: impacts of long-term anthropogenic land use change and climate variability. Hydrol. Earth Syst. Sci. 12, 159-175. https://doi.org/10.5194/hess-12-159-2008

Ward, P.J., van Balen, R.T., Verstraeten, G., Renssen, H., Vandenberghe, J., 2009. The impact of land use and climate change on late Holocene and future suspended sediment yield of the Meuse catchment. Geomorphology 103, 389-400. https://doi.org/10.1016/j.geomorph.2008.07.006

Weltje, G.J., 1997. End-member modeling of compositional data: Numerical-statistical algorithms for solving the explicit mixing problem. Mathematical Geology 29, 503-549. 10.1007/BF02775085

Weltje, G.J., Prins, M.A., 2003. Muddled or mixed? Inferring palaeoclimate from size distributions of deep-sea clastics. Sedimentary Geology 162, 39-62. https://doi.org/10.1016/S0037-0738(03)00235-5

Wilhelm, B., Ballesteros Cánovas, J.A., Macdonald, N., Toonen, W.H.J., Baker, V., Barriendos, M., Benito, G., Brauer, A., Corella, J.P., Denniston, R., Glaser, R., Ionita, M., Kahle, M., Liu, T., Luetscher, M., Macklin, M., Mudelsee, M., Munoz, S., Schulte, L., St. George, S., Stoffel, M., Wetter, O., 2019. Interpreting historical, botanical, and geological evidence to aid preparations for future floods. WIREs Water 6, e1318. doi:10.1002/wat2.1318

Wirth, S.B., Glur, L., Gilli, A., Anselmetti, F.S., 2013. Holocene flood frequency across the Central Alps – solar forcing and evidence for variations in North Atlantic atmospheric circulation. Quaternary Science Reviews 80, 112-128. https://doi.org/10.1016/j.quascirev.2013.09.002

Wolman, M.G., Leopold, L.B., 1957. River flood plains: Some observations on their formation, in: Professional Paper, edited by: Washington, D.C., 87-109.

Woolderink, H., Kasse, C., Cohen, K.M., Hoek, W.Z., Van Balen, R., 2018. Spatial and temporal variations in river terrace formation, preservation, and morphology in the Lower Meuse Valley, The Netherlands. Quaternary Research, 1-22. https://doi.org/10.1017/qua.2018.49

Yang, D., Yu, G., Xie, Y., Zhan, D., Li, Z., 2000. Sedimentary records of large Holocene floods from the middle reaches of the Yellow River, China. Geomorphology 33, 73-88. https://doi.org/10.1016/S0169-555X(99)00111-7

Zhao, H., Liu, Z., Song, L., Wang, C., Li, S.-H., 2018. OSL dating of flood sediments in the North China Plain. Quaternary Geochronology 49, 101-107. https://doi.org/10.1016/j.quageo.2018.07.010

Zuidhoff, F.S., Bos, J.A.A., 2011a. Landschap en vegetatie Lomm Hoogwatergeul fase II. In: D.A. Gerrets & R. de Leeuwe (red.), Rittelen aan de Maas. Lomm Hoogwatergeul fase II, een archeologische opgraving., in: edited by: ADC ArcheoProjecten, Amersfoort, the Netherlands, 27-61.

Zuidhoff, F.S., Bos, J.A.A., 2011b. Landschap en vegetatie. In: D.A. Gerets & G.L. Williams (red.), Water en Vuur. Archeologisch proefsleuvenonderzoek en opgraving te Lomm Hoogwatergeul Fase III., in: edited by: ADC ArcheoProjecten, Amersfoort, the Netherlands, 27-66.

Zuidhoff, F.S., Huizer, J., 2015. De noordelijke Maasvallei door de eeuwen heen. Vijftienduizend jaar landschapsdynamiek tussen Roermond en Mook. Inventariserend archeologisch onderzoek 'Verkenning Plus' project Maasvallei voor vijftien deelgebieden, in: edited by: ADC Archeoprojecten, Amersfoort,